



**UNIVERSITÀ DEGLI STUDI DI ROMA
TOR VERGATA**

**SCHOOL OF ENGINEERING
MEDICAL ENGINEERING**

A.A. 2021-2022

Master's Thesis

**The impact of residual strains
on the stress analysis
of atherosclerotic carotid vessels:
predictions based on the
homogenous stress hypothesis**

SUPERVISOR

Marino Michele
Gasser T. Christian

STUDENT

Mastrofini Alessandro
0299585

Table of Contents

Extended abstract	1
1 Introduction	4
1.1 Carotid atherosclerosis	4
1.1.1 Carotid artery	5
1.1.2 Pathophysiology	5
1.1.3 Clinical guidelines	9
1.2 Computational biomechanics: state of the art	11
2 Working hypothesis and thesis goal	18
2.1 Residual strain	18
2.2 Hypothesis: homogenous stress theory	19
2.3 Thesis goal	20
3 Methods	22
3.1 Continuum mechanics	22
3.1.1 Strain	23
3.1.2 Stress	24
3.1.3 Governing laws	26
3.1.4 Boundary Value Problem	26
3.2 Finite Element Method	27
3.2.1 Spatial description	27
3.2.2 Calculus of variations	28
3.2.3 Discretization	31
3.3 3D mesh generation	32

3.4	Tissue kinematics with growth and remodeling	33
3.4.1	Volumetric growth	34
3.5	Constitutive description	34
3.6	Growth formulation and algorithm	37
3.7	Synthesis of the complete workflow	41
4	Results	42
4.1	Benchmark case study	42
4.2	Patient-specific case study	47
4.2.1	Comparison between growth-load approaches	49
4.2.2	Stress analysis	53
4.2.3	Residual strains	59
4.3	Comparison between different patients	60
5	Discussion and conclusion	64
Acknowledgements		67
References		68
Appendix A - Simple cylinder geometry		76
Appendix B - Further patients		77
5.1	Patient (ID: 779)	77
5.2	Patient (ID: 753) - bulk material effect	78
5.3	Patient (ID: 710) - calcifications	79
Appendix C - Comsol Multiphysics		80
5.4	Staggered approach	80
5.5	Relaxed formulation	82
5.6	Variable stiffness spring	82
List of figures		84

Extended abstract

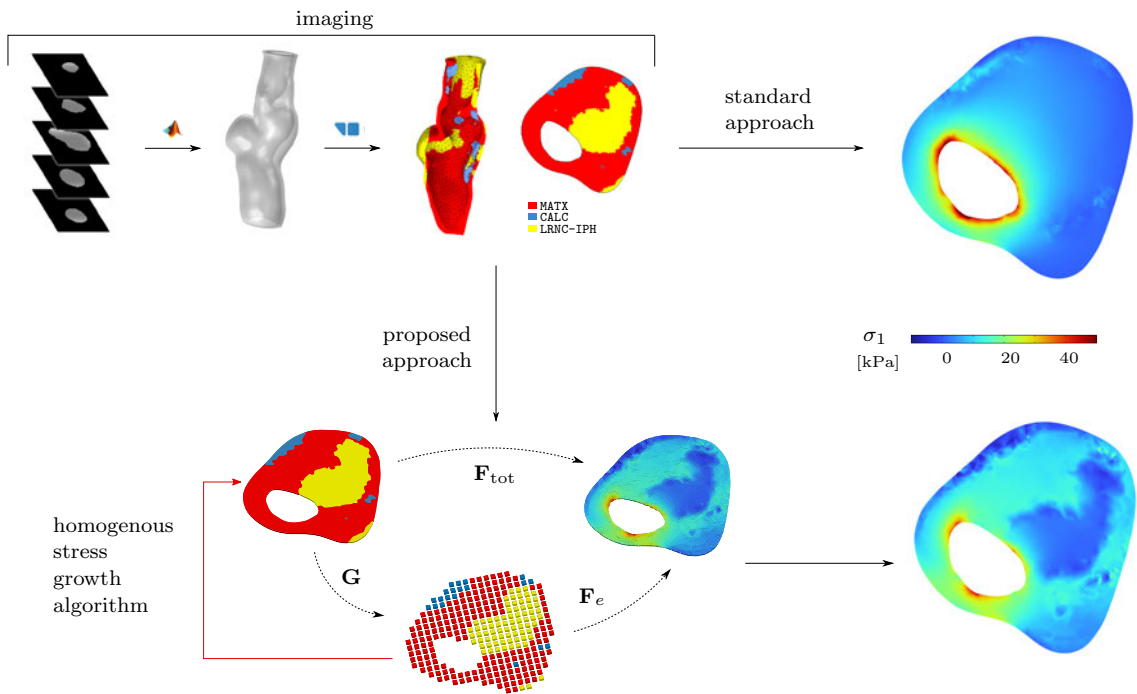
Cardiovascular disease refers to a group of disorders that affect the heart and blood vessels. These disorders are a leading cause of death and disability worldwide. Atherosclerosis and carotid artery disease are among the major causes of stroke, permanent damage and death. This is an important problem for both public health and economic impact. Severe clinical outcomes are related to massive plaque thickening and rupture, with the consequent risk of stroke and ischemic events leading the patient to death.

Atherosclerotic plaque development is a complex phenomenon that involves a number of different stimuli. Generally, it starts from an inflammatory lesion and endothelial cell dysfunction, then evolves under the influence of blood pressure, lipids, infections, wall shear stress, and generic expression of the chemo-mechanical environment [79]. As a consequence, the characteristics of the plaque and surrounding vascular tissues are highly patient-specific. Due to the variability in populations current clinical guidelines suggest the need for personalized investigation and individual rupture risk evaluation focusing on the patient-specific plaque morphology [90].

Computational biomechanical analyses may help in this purpose, allowing to evaluate stress and strain inside the atherosclerotic plaque and surrounding tissues in order to better assess the rupture risk and investigate pathology evolution [18, 20]. This require to analyze patient-specific geometry, material properties, plaque morphology and loading conditions [67, 15]. Nowadays, advanced numerical methods allow us to simulate the mechanical environment of the plaque by considering inhomogeneous materials with different plaque constituents, patient-specific geometry and very specific loading conditions [11].

However, computational studies often ignore residual stresses and strains in vascu-

lar tissues and this could lead to potentially inaccurate solutions [68, 60]. Neglecting residual strains in the load-free configuration could lead to an overestimation of the stress field and imprecise risk evaluation for plaque rupture. This is even more significant in patient-specific cases since the geometry and the presence of the plaque may significantly alter the mechanobiological environment of cells that drive growth and remodeling mechanism responsible for the occurrence of residual strains.



In this thesis, we propose a computational framework to take into account residual strains and stresses by following the homogenous stress hypothesis. The underlying rationale is that vascular tissue undergo continuous growth and remodeling with the attempt to reduce stress gradients and obtain a stress field as homogeneous as possible within vessel wall. This hypothesis agrees well with well-established evidence on the existence of an homeostatic tensional stress state in biological tissues [30].

The developed computational tool allows to perform stress analyses on patient-specific pathological carotid arteries with different levels of atherosclerosis. Based on clinically approved software for histopathological segmentation, medical volumetric images of carotid arteries with atherosclerotic plaques are converted into a discretized

three-dimensional numerical model. Tissues segmentation allows to discriminate between the different plaque constituents, such as lipid-rich necrotic core, calcification and intra-plaque hemorrhage. Starting from these segmented images, a non-linear finite element structural analysis is implemented by including a growth formulation based on the homogenous stress theory for vascular wall remodeling. The growth and remodeling formulation is based on the kinematic decomposition of the deformation gradient in a large strain framework. The growth-related deformation gradient is defined such to reduce high stress gradients within non-atherosclerotic portions of the vascular tissues.

The campaign of numerical simulations address four patient-specific case studies characterized by profound differences in vessel geometry, in the characteristics of plaque lesion, and in the relative portion between plaques and surrounding tissues. Obtained results highlight how including residual strains lead to considerably different results with respect to standard analyses without growth and remodeling. Due to the growth-induced stresses, the model provides quantitative relations between plaque biomechanical environment and rupture risk investigation based on the distribution of different pathological tissues. The proposed methodology open towards the development of novel *in silico* diagnostic tools allowing for a strongly individualized plaque rupture risk assessment.

Chapter 1

Introduction

Cardiovascular diseases are the largest cause of death worldwide, representing more than 30% of all global deaths. This represents a health issue but also an economic challenge for healthcare systems. With almost 50 million people currently living with cardiovascular diseases in Europe, it represents an economic cost of more than €210 billion per year [91]. Indirect costs such as morbidity, the follow-up process, productivity loss, or general informal care costs should be also considered. Indirect costs could be as higher as direct ones. Cardiovascular disease diffusion is also expected to increase in the following years.

Cardiovascular diseases deaths are mainly related to heart attack and ischemic stroke related to unstable atherosclerosis [100] and hence it is extremely important to investigate atherosclerosis from a clinical point of view.

1.1 Carotid atherosclerosis

Carotid atherosclerotic diseases appear when plaque builds up in carotid arteries. It is also called carotid stenosis and represents a significant reduction in the vessel's lumen and additionally causes the hardening of the vascular tissue. That pathological process is due to progressive depositions of material in the vessel wall. Atherosclerosis is a systemic event and both plaque development and evolution could be affected by involved arteries with their geometries as well as from plaque morphology and composition. In carotid arteries when the narrowing of the lumen became severe it could restrict blood flow to the brain and cause stroke. Ischemic stroke could also be

related to plaque rupture and subsequent clots or hemorrhage.

1.1.1 Carotid artery

Carotid arteries are vascular vessels situated in the neck that supply blood to the brain. There are two different branches, one per each side of the neck, named as the common carotid artery. The common carotid artery (CCA) travels from the chest to the head. The left one originated directly from the aortic arch instead the right one originate from the brachiocephalic trunk.

On the way, the common carotid forks into two branches: the internal (ICA) and the external (ECA) carotid arteries. Common carotid artery is characterized by a typical diameter of 6.3 mm while internal one is characterized by a diameter of 4.8 mm. Thickness range between 0.4 mm and 0.8 mm. Generally, size appears bigger in man than woman [13]. There can be a significant variation on one or both sides of the neck. Both the internal and external carotid arteries forks into several smaller branches which carry blood, oxygen and supplements to the neck, head and brain. The external branches generally supply the face, tongue, teeth, ears, and other structures in the face. The internal branches supply the ipsilateral cerebral hemisphere, the eye and accessory organs [83]. A schematic representation is shown in fig. 1.1.

1.1.2 Pathophysiology

The disease is represented by a narrowing of the arterial lumen caused by atherosclerosis. It represents the deposit of substance as lipids, calcium and other waste products from biological reactions into the arterial wall.

The Cardiovascular Health Study detects high incidence of arteriosclerosis with 5% of the general population over 65 years showing stenosis higher than 50% of the lumen section [69].

Risk factors could be classified as modifiable and not modifiable ones. Not modifiable predictors are age, sex, family history, and race. Several studies have shown as atherosclerosis generally increases with age [80, 103]. Males generally show a higher risk to develop dangerous atherosclerotic plaque, with respect to women [73]. Another independent risk factor is age, older people show a higher risk of plaque instability

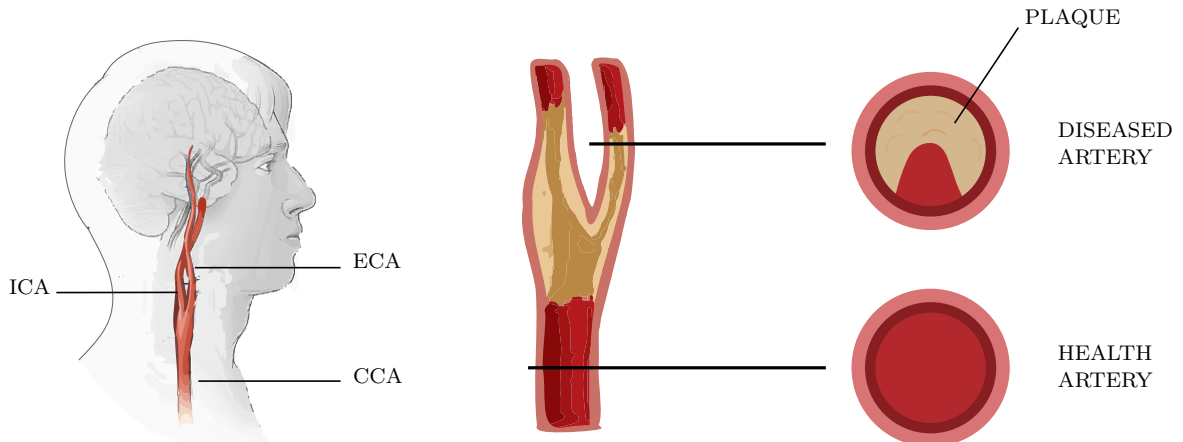


Figure 1.1: Schematic representation of the carotid arteries: common carotid artery (CCA), internal carotid artery (ICA) and external carotic artery (ECA). Schematic representation of the plaque at the carotid bifurcation.

[99]. Modifiable risk factors are represented by smoking, hypertension, and diabetes are established as a risk factors for carotid atherosclerosis. The intensity of blood pressure and cholesterol levels can affect stenosis progression [102]. Recent studies show also a general influence of socioeconomic status. Lower socioeconomic status is associated with a higher frequency of severe stenosis and also minor treatment [32, 57].

Plaque development

The plaque development in carotid arteries is similar to the development found in other arterial sites. Atherosclerosis is a systemic pathology and it appears to be related with vascular areas showing low wall shear stress and flow stagnation, typical condition for ramification points of the vascular tree.

The vascular wall responds to injury with a cascade of events leading to plaque formation. The development of the early lesion consecutively activate further reactions that lead to plaque growing into a fibrous plaque and more complex advanced lesions.

The first injury-response action is the inflammatory process leading to endothelial cells (EC) dysfunction. This is followed by the lipids accumulation driven by several reason. ECs alteration leads to a loss in permeability as well as the endothelial action as a selective barrier. This leads also to modified expression of the lipoprotein

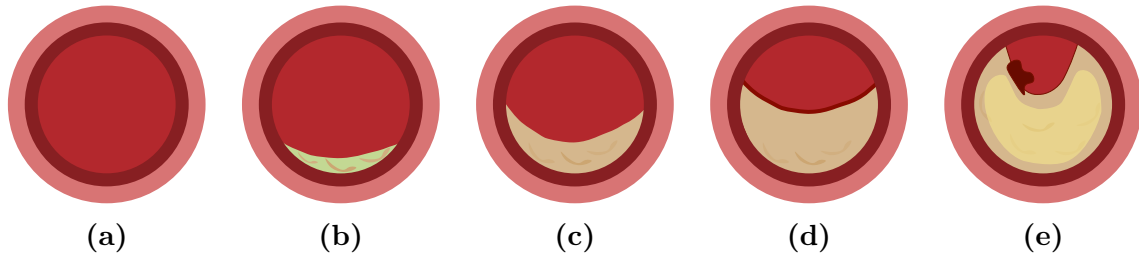


Figure 1.2: Evolution of carotid atherosclerosis: normal vessel (a); initial intimal thickening (b) low-density lipoprotein deposition and starting of oxidative reaction (c); atheroma (d); clinical condition with large necrotic core, thin fibrotic cap and thrombosis (e).

receptors that are responsible for internalizing lipoprotein from the vessel's lumen. Then, it results in an increased oxidative state that leads to cascade events driving to higher adhesion of monocyte. Incorporated lipids are also retrained by the smooth muscle cells and macrophages. Due to their receptors with altered regulative feedback, they continue ingurgitating lipids leading to the formation of bigger foam cells. In addition, smooth muscle cells in atherosclerotic show phenotypic modulation that reduces their contractile activity while increasing their lipid accumulation.

Due to cellular mechanotransduction aforementioned factors are also modulated by mechanical aspects such as blood flow, cell foundation movements, and wall shear stress. Mechanical force could modulate ECs dysfunction, lipid accumulation, and inflammatory cell recruitment in order to maintain local homeostatic states [93].

Intimal thickening

Nowadays, it is believed that atherosclerosis is initiated by the entry of low-density lipoprotein into the subintimal space. Following some specific metabolic condition low-density lipoprotein could be oxidized and this leads to a cascade of enzymatic reactions inducing local inflammation and activation of surface adhesion molecules. Also, smooth muscle cells are attracted to the area.

The monocytes are then converted into macrophages. They can engorge lipids and this leads to a high release of free cholesterol in the extracellular space. This attracts other macrophages into a vicious cycle that leads to the formation of a big necrotic core confined between the intima and the media layer of the vascular wall.

Another important element is the fibrous cap. It is composed of vascular smooth muscle cells inside a collagen fibers matrix, represents the plaque portion towards the vascular lumen. It maintains the integrity of the plaque. It starts to appear in the advanced type of atheromatous lesion and represents a more substantial deposit of lipids, hematoma and thrombotic.

It represent the first stage of advanced lesion of atherosclerosis in artery following the American Heart Association (AHA) classification scheme. The thickness of the cap is related to the risk of ischemic neurological symptoms and showed to be strongly related to symptomatic plaque [14].

The lipid-rich necrotic core (LRNC) generally constitutes the main portion of the plaque due to a protracted deposition of lipid. Larger cores seem to be associated with plaque rupture in both symptomatic and asymptomatic carotid disease and show an inverse relationship with cap thickness [70]. Furthermore, bigger necrotic core provides a good environment for macrophages and proteolytic enzymes that could degrade the collagen. A higher content of free cholesterol, typically shown in the larger necrotic core, is potentially correlated with a higher risk of volume expansion due to crystallization.

Damages in the plaque vasculature and neovessels lead to the formation of intraplaque hemorrhage (IPH). The fragility of these vessels is due to the absence of smooth muscle cell support and their density is positively related to the necrotic core formation. Furthermore, also the presence of intraplaque hemorrhage contributes to further lipid deposition [65].

Intraplaque hemorrhage shows an association with the increase in necrotic core size and also in lesion instability [49]. It could destabilize the plaque through the hemoglobin released from red blood cells which is a potent pro-inflammatory agent.

Plaque rupture

Lipid accumulation in the plaque core leads to an increased stress state on the fibrous cap that could potentially predispose to plaque rupture [18]. When the plaque core starts to be saturated with cholesterol crystallization is initiated and the core expands in volume. It could contribute to the fibrous cap stretch [2]. Furthermore, this

high concentration of lipids and consequently macrophages activation promotes the secretion of proteolytic enzymes capable of degrading the extracellular matrix leading to a weakening of the fibrous cap [6]. This degradation leads to a diminished collagen synthesis and then a reduced extensibility of the tissue that could lead to rupture at a lower stress range.

Plaque rupture is a catastrophic event leading to severe clinical manifestations such as stroke and ischemic events. Disruption of the plaque cap exposes the core to bloodstream. It results in thrombus developments in the lumen space and it may lead to embolism. That represents the major cause of ischemic events and stroke progression. Several evidences charge plaque rupture as the main cause of ischemic attacks rather than blood flow reduction [54].

1.1.3 Clinical guidelines

Currently, it is possible to use several noninvasive imaging techniques to analyze and study atherosclerotic plaque. The most common are Doppler ultrasound, MRI, computer tomographic angiography (CTA), and positron emission tomography (PET). Different techniques have different pros and cons, as well as costs and risks for the patient that must be correctly considered. From the point of view of the analysis of the atheroma, the MRI and the CTA are shown to be the best with higher spatial resolution and better possibility to distinguish between different tissues.

It is necessary to separate the medical approaches for symptomatic and nonsymptomatic carotid diseases. A carotid stenosis is classified as symptomatic when a transient ischemic attack or stroke is present. Cerebrovascular events are classified as transitory when are resolved in 24 hours or strokes if the deficit is longer. For asymptomatic disease, generally, the treatment includes treatment of hypertension in addition to lipid-lowering drugs. This should be correlated with physical exercise, weight loss, dietary precautions and smoking and alcoholic cessations. For symptomatic and higher degrees of stenosis, a surgical approach is selected. A typical surgical approach includes carotid endarterectomy and carotid artery stenting as invasive therapy.

Current guidelines suggest surgery interventions with a threshold between 50% and 70% of lumen stenosis in relation to patient's symptoms and other risk factors

correlations. When stenosis exceeds 50% it introduces significant changes in hemodynamics and generally leads to a drastic aggravation of the disease [64]. For symptomatic stenosis, the degree of stenosis strongly impacts on stroke risk [21, 8]. To assess the risk of plaque instability it is necessary to include more information such as plaque morphology, patient lifestyle and general clinical conditions. Characterization of plaque enhances the understanding of atherosclerotic development. Generally, plaques with a large lipid core, thin fibrous cap and intraplaque hemorrhage are associated with subsequent thromboembolic ischemic events for both asymptomatic and symptomatic patients [66]. Medical decisions should follow also plaque morphology and analyze stenosis progression, plaque surface area, and presence of ulceration or echolucency for individual cases.

Despite current guidelines rely on lumen narrowing, a lower degree of stenosis generally doesn't guarantee for lower failure risk or a smaller possibility to observe plaque progression. Evidences show 47% of plaques ruptured with less than 70% of luminal narrowing with a high prevalence in segments generally less narrowed than 80% of the total lumen area. Several studies also report a thin fibrous cap as indicator of high vulnerability [80]. Currently, new risk indexes and markers start to be developed taking into account plaque neurovascularization, inflammation and tissue stiffness [64]. Also, hemodynamics shows an important role in plaque development and progression. So, it is really important to start considering patient-specific risk factors. The development of more precise diagnostic tools is still lacking.

In the lately 20 years, an engineering perspective on risk analysis was developed using computational biomechanics. Using the patient-specific geometry, plaque morphology, different tissues distribution and several information from clinical history and medical images, it is possible to assess the three dimensions stresses and strains distribution around the plaque and plaque boundary in order to better estimate biomechanical indexes of risk for plaque failure.

The biomechanical computational analysis could also allow us to better understand plaque evolution and different types of tissue interaction with the chemo-mechanical environment of the diseased vascular tissue.

1.2 Computational biomechanics: state of the art

Starting from 30 to 20 years ago, computational mechanics strongly involve academia and industry in simulative studies. In the late years, also thanks to advancements in silicon technology and computational power, a number of new models have been proposed. Now, it is possible to simulate complex geometries with strongly non-linear tissue behaviors, possibly involving time-dependent processes such as growth and remodeling. Remarkably, these computation models start to be used in clinical procedures [22, 94].

Biological systems are very complex. A large number of cells is involved in their description with several processes evolving through non-linear behavior and operating at different scales. Furthermore, biological systems are dynamic entities whose behavior could be affected by their previous evolutionary steps and history, involving time-dependent processes. This leads to seeing biological organisms as four-dimensional entities where the organism lives and evolves in a spatial three-dimensional domain spanning over the time domain. Then a lot of time-related effects should be taken into account such as viscoelasticity, damage and softening, evolution and remodeling or permanent strains.

Representation of biological systems requires multi-scale modeling to account for several processes that involve different time and spatial scales. These models generally involve multi-physics descriptions and integration of different disciplines. These models are based on the same principle of biological hierarchical relations between system and their sub-systems with a mutual interaction at different scales. For instance, cells could influence tissue behavior and consequently the scale of the organs where a macroscopic regulation could, in turn, send feedback to adjust the micro scale interactions. Analogous multi-scale representations are required for time scales that could span from molecular interactions in seconds to a macro scale involving hours, days, or years.

Then, a typical approach is to proceed through a model reduction in order to obtain a simplified model capable to describe the features of interest as accurately

as possible [7]. Every model is characterized by the observation of reality followed by abstraction in order to obtain a virtual description representing the real systems. These virtual models should not only describe the observed reality but also be able to make predictions and explanations about the real systems.

Starting from cell-to-cell interaction to the full organism, it is currently impossible to use a unique model to describe every aspect and, in fact, a good model should focus only on the aspect of interest for the purpose of the model itself. Several models have been developed to describe bio-chemo-mechanical systems, their behavior, interaction and evolution. Here, we focus on the biomechanical aspect of the atherosclerotic vessels.

Initially, separate models were developed to describe mechanical and biological characteristics but now several aspects could be investigated as correlated entities. This leads to a description of the mechanical behavior of the vessel where the mechanical properties could be related to the biochemical environment and micro constituents.

In this thesis, we consider a continuum approach where the material descriptions are given at a macro-scale accounting for smaller (and eventually larger scales). This approach is widely used for vascular vessels [46]. The vessel wall is described as a continuum entity where the material properties could be related to several constituents, such as cells or extracellular matrix, through several models based on a smaller scale. Furthermore, various experimental procedures have been developed to numerically characterize and validate these models.

Continuum approaches use a mathematical representation of the governing laws through partial differential equations (PDE) involving a continuum description in space and time. Then, we need a numerical approach to apply these models to complicated in-vivo cases and a widely used numerical approach is the Finite Element Method. Finite Element analyses involve the study of atherosclerotic plaque in order to investigate three-dimensional stress distribution investigating several boundary and loading conditions to best assess the biomechanical response with different geometries, tissue distributions, and materials.

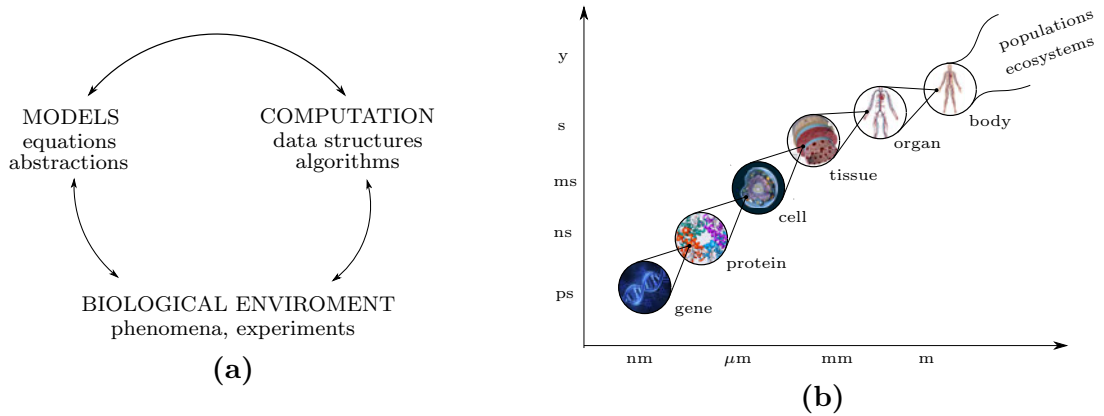


Figure 1.3: Representation of biological organisms involves multiple disciplines to describe the real systems and be able to extract useful results from the model (a); Biological hierarchy involve multiple scales (b)

In atherosclerosis, as well as in other pathologies, the mechanical environment plays an important role in disease development and progression and should be considered for the best selection of treatment, strategies and decisions. The vascular tissue, especially the smooth muscle cells and the endothelium, reacts to the mechanical environment and to their strain [43]. To better address the stress state inside the plaque we need to describe the mechanics of each involved material. The accuracy could strongly depend on the plaque components estimations and the composition could affect the final results [4, 15].

Modern cutting-edge approaches are based on single patient features and are known as patient-specific models. Whilst it is relatively easy to extract patient-specific geometrical features, there are no well-established procedures to extract mechanical parameters from in-vivo tissue. Geometric features such as the lumen or wall of the vessel could be extracted with imaging techniques used for medical diagnosis. There are several approaches that could be integrated into clinical procedures in order to extract geometries with a good resolution and so they could be used for numerical approaches. Widely used imaging methods are MRI and CT scanners [5].

The second important aspect of a patient-specific application is the fitting of a general mechanical model to the patient's tissues. This requires mechanical testing of

the tissue and it is clearly impossible to do in-vivo and so requires ex-vivo approaches. Lately, some techniques have been developed in order to characterize specific mechanical properties starting from imaging techniques [98]. However, the general approach is based on statistically determined mechanical properties starting from tests carried out on ex-vivo tissues.

The evolutional aspect of plaque growth plays a key role to assess plaque vulnerability. The main structural components of the vascular wall and plaque are smooth muscle cells, elastin, collagen, lipids and calcification. To characterize the single material properties it is possible to use standard uniaxial testing [96] or more advanced technique as micro and nano indentation, unconfined compression or dynamic compression testing [9, 15, 44, 89, 3].

Most numerical and experimental studies on both coronary and carotid atherosclerotic plaque assume that it is possible to describe the plaque components as continuum materials following the continuum mechanics theory. It is the only approach available to implement a clinical application to investigate stress and strain into the plaque [43]. Models are currently used to quantify the stress and strain state inside the plaque or to understand the Wall Shear Stress induced by the blood flow [35, 61]. They could also be used to best investigate the stress risk factors or to better understand the plaque progression [88, 55]. Recent advanced models show relatively accurate assumptions as non-linear hyperelastic incompressible material with three-dimensional patient-specific geometry. Several models consider isotropic constitutive models as Neo-Hookean, Yeoh or Mooney-Rivlin models [11, 56, 40]. Other assumptions consider anisotropic constitutive laws to better characterize some specific behavior as fiber orientation across different tissues [16, 53].

Furthermore, the fluid-dynamics aspects are also important, and the flow-induced shear stress influences plaque initiation and progression. The latest advanced models start using a coupled formulation to consider both the mechanical stress and strain distribution and the fluid dynamic Wall Shear Stress, and their combined effect, developing a fluid-structure interactions model accounting also for blood properties and pulsatile dynamics due to the cardiac cycle [29, 74].

Considering that most vulnerable plaques are characterized by the presence of a large necrotic core and a thin fibrous cap, it is possible to address the failure events also to higher peak stress in the fibrous cap [43]. Several studies suggest how circumferential tensile stress plays a crucial role in plaque rupture. Typically, a threshold of 300 kPa [18] is adopted as a rupture limit of the fibrous cap. In vivo strain measures are an interesting topic and a validation for in vitro findings. It is important to consider the blood pressure-induced strain from a computation point of view and also to address the residual strain [82, 76]. Generally, this is not considered in computational biomechanics because it is difficult to quantify from in vivo measurements.

Nowadays, it is clear that physiological tissues are constantly searching for a homeostatic state. Homeostasis is a dynamic process through which the organism continuously adapts toward an equilibrium state. This originates from the cell's sensing activities. They could respond to mechanical stimuli such as shear loads or mechanical strains, biological stimuli due to the extracellular matrix or cell interactions, as well as to morphological stimuli as surface topography or substrate stiffness [17]. Cells are dynamically connected with their external environment and transduce these surroundings into intracellular and intercellular signals that could modify their interaction in order to maintain integrity and tissue health. It is demonstrated that different types of cells could sense different stimuli. For the mechanical environment, there are cells that respond better to shear loads and others to tensile or compressive loads in order to reach homeostasis [30]. Several models have been developed to deal with atherosclerotic initiation and evolution. Different approaches have been used, both with continuum or discrete descriptions. Typically the discrete ones are agent-based modeling (ABM) or cellular automata (CA), often also combined with continuum approaches and finite element analysis. These models include biological factors related to the disease describing interaction at tissue levels accounting also for the structure at the macro-scale [33, 12, 20, 26]. All these models are based on the observation that the main actors in atherosclerotic disease are inflammation and accumulation of LDL, cholesterol, macrophages and foam cells.

Homeostasis could act at different time scales. In vascular reactivity for instance, whilst the vasodilation and vasoconstriction interactions are regulated in minutes further remodeling processes could require days, weeks or years of persistent stimuli. Homeostasis not only depends on a time scale but also on a spatial scale, there are several active regulation processes that act from the cellular scale to an inter-tissue interaction leading to a single organ regulation while still respecting the complete organism homeostatic state.

Furthermore, homeostatic states are incorporated into the growth and remodeling (G&R) processes of biological tissues through both gene expression, regulation and/or more general internal or external stimuli [71].

External loads are among the most effective causes of growth and remodeling for every tissue, especially for vessel regulation [27].

There are different approaches to describe growth and remodeling and they generally require finite elasticity descriptions since soft tissues generally undergo large deformations. Also, it is often required to account for multi-phase interactions and calibrate experiments for differences between in-vivo and ex-vivo behavior [63].

Starting from the standard non-linear continuum mechanics two approaches have been developed: kinematic growth and constrained mixture models [27]. Kinematic growth follows the definition of volumetric growth as a change in the local stress state of the body and it could be expressed through the deformation gradient. Several stress-based growth models start from the hypothesis of a mass rate expressed as a function of the stresses in order to maintain equilibrium and balance between growth and resorption [36], but different rationale exist [78]. The constrained mixture models are based on a representation of n different constituents. Following the mass turnover every constituent could depose or withdraw mass and the net mass turnover is determined by the summation of these several increments. Each element could separately be active at a separate time and the overall volume changes are determined by their superposition [10]. Despite the homogenized mixture models are based on biologically motivated growth law deriving from micro-mechanical models, they require high computational power with respect to the kinematic theory. Otherwise, the latter relies on

heuristic growth laws.

Due to growth and remodeling, tissues are characterized by initial strains that should be taken into account in simulations and they could strongly affect results [5]. They could act in order to homogenize stress distribution across the biological structure leading to more stable states [72].

Residual strains are clearly demonstrated by the presence of an opening angle, that is the angle obtained from the releasing of the residual stresses with an infinite series of transmural cuts [86]. Every cut induces a permanent deformation leading to a global finite displacement. From the assumption of a purely cylindrical vessel structure, it is possible to define the opening angle by comparing the closed cylinder and the opened one. Clearly, such assessment requires ex-vivo experiments.

Residual stresses and strains could affect the physiological response [97, 77] and some recent studies started to involve residual stresses and strains in Finite Element analyses. Specifically about atherosclerosis, several models analyze the influence of residual strain and stress in coronary atherosclerotic plaque [60, 68], aortic aneurysm [76], carotid bifurcation [28] and generic arterial wall tissue [101, 81]. Neglecting residual stresses and strains leads to an overestimation of peak stress and stress amplitude in the thin fibrous cap. Although it is very complex to account for residual stresses and strains from a computational point of view, denying them could lead to inaccurate results.

Chapter 2

Working hypothesis and thesis goal

Atherosclerotic diseases are multifactorial phenomena related to several chemo-mechanical interactions occurring in a relatively long time. Vascular tissue also shows a continuous remodeling that affects the development of the pathology.

One of the most important remodeling activities present in vascular tissue is related to the stress state associated with the average blood pressure conditions during an heartbeat. For biological tissues, there exists a preferred homostatic stress state maintained by the tissue itself [27]. It is not clear what variable regulates this state however several studies show how stress plays a very important role [85].

Then, depending on the intensity of the external mechanical stimuli, growth and remodeling of the tissues activate in order to maintain a homeostatic tensional state. In fact, the presence of residual stresses and strains within vascular tissues is known for several years and is strongly supported by experimental studies [92, 38].

2.1 Residual strain

The stress that exists in an unloaded configuration is called residual stress and, generally, in living tissues it is non-null, although it must be clearly self-balanced. Moreover, the stress and strain state is strongly related to the biological functions of the cells, tissues, or organs. It is a reciprocal interaction between stresses that modulate cell activity inducing growth and remodeling of the vascular tissue that in turn changes the three-dimensional stress and strain state.

The most common approach for residual strains measurements is related to the

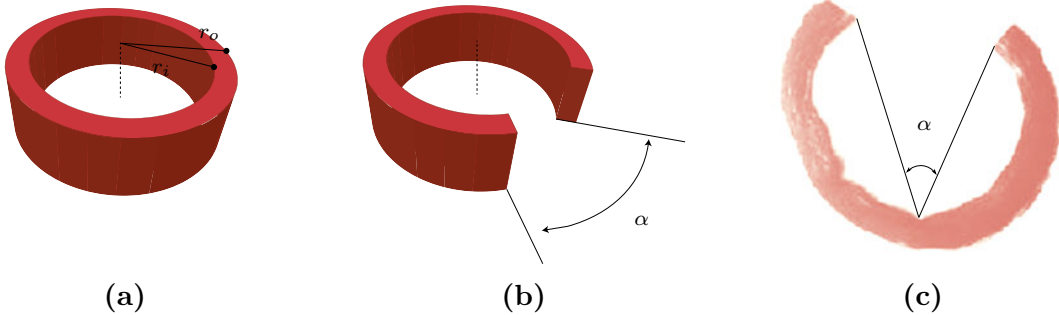


Figure 2.1: One of the way to represent the opening angle α . Whole ring geometry with internal and external radii(a); Cutted ring geometry (b); Opening of a common carotid artery ring showing the releasing of residual stresses (c) [84]

opening angle. It relies on the idea of using an arterial segment with one or more cuts to relieve the stress. So it is possible to compare the stress-free configuration (the one with cuts) with the closed ring, focusing on the load, strain, and stress necessary to close the configuration. However, there is a general consensus that this approach is not sufficient to characterize the complete three-dimensional stress state in the arterial wall although it could necessary to consider the residual stress state as a fully three-dimensional property of the tissues [47].

A well-established hypothesis is that the main purpose of the residual strain is to contribute to the homogenization of the stress inside the vascular tissue [37]. It is induced across the vascular wall thickness in order to compensate for the effect driven by the inside pressure of the blood. So, a number of interesting approaches are based on the hypothesis of uniform stress distribution across the wall thickness [19].

2.2 Hypothesis: homogenous stress theory

The arterial wall could be assumed to evolve to maintain a constant stress gradient across the wall thickness. This is called homogenous stress theory and is in contrast with the more typical assumption of zero initial stress hypothesis. It is related also to the uniform strain theory which hypothesizes that the vascular wall maintains constant the circumferential strain in the cross section during the remodeling process [87], both are based on the growth and remodeling process seen as strongly related to

the organism homeostasis.

Experimental evidence shows how the stress state in the vessel is maintained around a determined range. This range is constant across the individual life span and several biological species [104]. Furthermore, it could be altered by pathological state [75]

Generally, the vascular vessel tensional homeostasis leads to a negative stress gradient in the arterial wall with a negative strain on the outside of the vessel in the load-free configuration [19]. So, it is possible to see the growth and remodeling process as an active action acted to minimize the stress differences in the structure. In fact, a structure with a more homogeneous stress state is, in general, safer from an engineering viewpoint than a structure with a higher stress peak.

The aforementioned hypotheses are generally used to investigate the growth and remodeling processes of healthy vascular tissue, often in structures characterized by regular geometries and a single material. This is far different from real clinical cases that require accounting for complicated geometries and multiple material descriptions. Whilst vascular tissue generally shows biochemical homeostasis, for other pathological tissues present in the atherosclerotic region, such as the lipid-rich necrotic core or the calcifications, it is not possible to grow and remodel [58]. However, they play an active role in determining the stress state that acts on the vascular tissue processes affecting the development of high-stress areas as well as vessel portions partially cleared from loads. Hence, it is possible to hypothesize that structures that are not able to adapt towards a more homogenous stress state, show a higher risk of rupture due to the occurrence of high stresses.

2.3 Thesis goal

The goal of this thesis is to develop a computational tool for the stress analysis of patient-specific carotid structures with large atherosclerotic regions. The general aim is to improve the accuracy of *in silico* strategies for risk evaluation and plaque rupture estimation. This is aimed by enriching traditional simulation approaches via a growth and remodeling formulation that employs a multi-material description. Adopting

a growth strategy based on the homogenous stress hypothesis, residual strains and stresses for vascular vessels are computed in realistic clinical scenarios. Accordingly, their impact in determining the biomechanical state of the vessel are accounted for and evaluated on four different patient-specific case studies with different pathological conditions.

Chapter 3

Methods

In order to numerically solve the problem we need a computational framework able to characterize the stress and strain state in the diseased carotid vessel incorporating the description of the different materials of the atherosclerotic plaque as well as the growth and remodeling processes.

3.1 Continuum mechanics

All real objects are composed of molecules with their atomic structures and compositions leading to microscopic systems. However, from a mathematical point of view, this may not be an adequate approach. We consider the continuum mechanics approach to describe various physical phenomena with macroscopic models that represent a description of the internal structures and micro-systems. We considered the macroscopic system treated as a homogeneous medium focusing the investigation on the study of motion and deformation, the study of stress, and the relation with the fundamental laws of physics.

Then, we consider a continuous body in the reference configuration Ω_0 that could move in space toward the spatial configuration Ω . The map between reference position \mathbf{X} and the spatial position \mathbf{x} of the material particle is represented by the motion $\mathbf{x}(t) = \chi(\mathbf{X}, t)$. In finite deformations, no assumptions are made on the magnitude of displacement $\mathbf{u} = \mathbf{x} - \mathbf{X}$, that as no small displacements are required.

At the time t the motion in the neighborhood of a material point is represented

by the deformation gradient:

$$\mathbf{F}(\mathbf{X}, t) = \text{Grad } \chi(\mathbf{X}, t) = \frac{\partial \chi(\mathbf{X}, t)}{\partial \mathbf{X}}. \quad (3.1.1)$$

It is the primary measure of deformation and allows to relate the relative position of neighboring particles after and before the deformation in terms of their relative material position.

The local motion could be also decomposed into a rigid body motion and deformation using a polar decomposition of the deformation gradient as

$$\mathbf{F} = \mathbf{R}\mathbf{U} = \mathbf{v}\mathbf{R}. \quad (3.1.2)$$

\mathbf{U} and \mathbf{v} represent unique, positive definite, symmetric tensors called respectively as right (or material) stretch tensor and left (or spatial) stretch tensor. They measure local stretching along mutually orthogonal eigenvectors. \mathbf{R} is an orthogonal tensor called as rotation tensor representing the rigid body rotation.

3.1.1 Strain

At finite deformations, non-linear strain measures are used to correctly represent the differences between the reference and the spatial configuration.

The right Cauchy-Green strain is formulated with respect to the reference configuration and could be expressed as:

$$\mathbf{C} = \mathbf{U}^2 = \mathbf{F}^T \mathbf{F}. \quad (3.1.3)$$

An additional deformation tensor is the Green-Lagrange strain tensor, reading:

$$\mathbf{E} = \frac{1}{2} (\mathbf{F}^T \mathbf{F} - \mathbf{I}). \quad (3.1.4)$$

The latter is used to represent the change in the squared lengths $\lambda_a^2 - 1$, where λ_a is the linear stretch and represents how the line element is deformed from the original direction \mathbf{a}_0 to the spatial configuration $\mathbf{a} = \mathbf{F}\mathbf{a}_0$ (with $|\mathbf{a}_0| = 1$). This is:

$$\lambda_{\mathbf{a}} = \frac{dl}{dL} = \frac{|\mathbf{F}\mathbf{a}_0|}{|\mathbf{a}_0|} = \sqrt{\mathbf{a}_0^T \mathbf{F}^T \mathbf{F} \mathbf{a}_0} = |\mathbf{a}|. \quad (3.1.5)$$

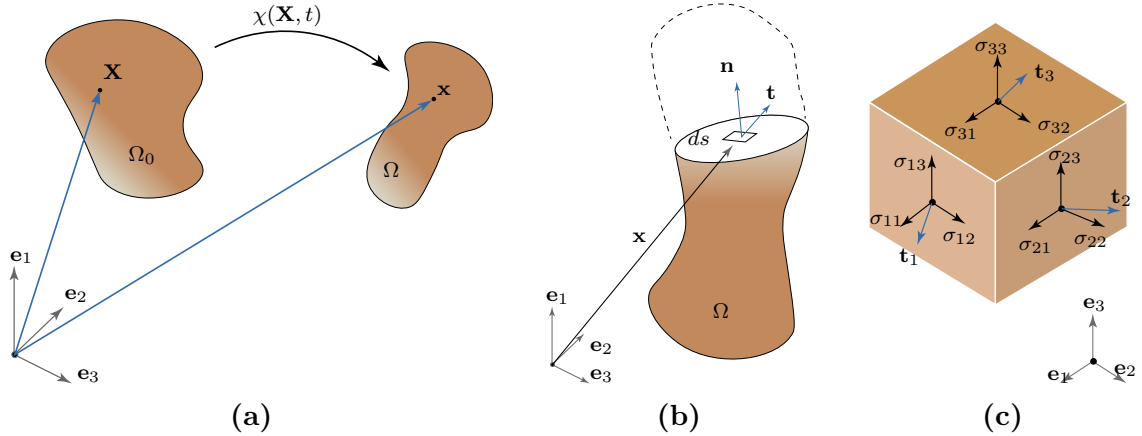


Figure 3.1: Motion χ of the body from the reference configuration Ω_0 to the current configuration Ω (a); Representation of the stress state, with a hypothetical cut through the body perpendicular to \mathbf{n} , and of the corresponding traction vector \mathbf{t} resulting from the Cauchy's stress theorem $\mathbf{t}(\mathbf{x}) = \boldsymbol{\sigma}(\mathbf{x})\mathbf{n}(\mathbf{x})$ (b); Normal stress components σ_{ii} and shear stress components σ_{ij} determine the traction vector \mathbf{t} and the load acting at the material particle (c).

A line element is extended for $\lambda_a > 1$, unstretched for $\lambda_a = 1$ or compressed for $\lambda_a < 1$.

The Cauchy-Green strain tensor can be also represented through eigenvalue representation, with the principle stretches λ_i and the principal stretch direction $\hat{\mathbf{N}}_i$, as:

$$\mathbf{C} = \lambda_i^2 \hat{\mathbf{N}}_i \otimes \hat{\mathbf{N}}_i. \quad (3.1.6)$$

3.1.2 Stress

To represent the load on the material particle a stress measure is required. The Cauchy stress $\boldsymbol{\sigma}$ is a second-order tensor used to represent the stress state containing both the normal stress and the shear stress components acting respectively perpendicular or in parallel to the local area ds as shown in fig. 3.1c.

However, at finite deformation, where the current configuration is different from the reference one, other stress tensors may be defined. While the Cauchy stress is represented in the current configuration, the first Piola-Kirchhoff relates the force in the spatial configuration to the area element in the reference configuration. Through

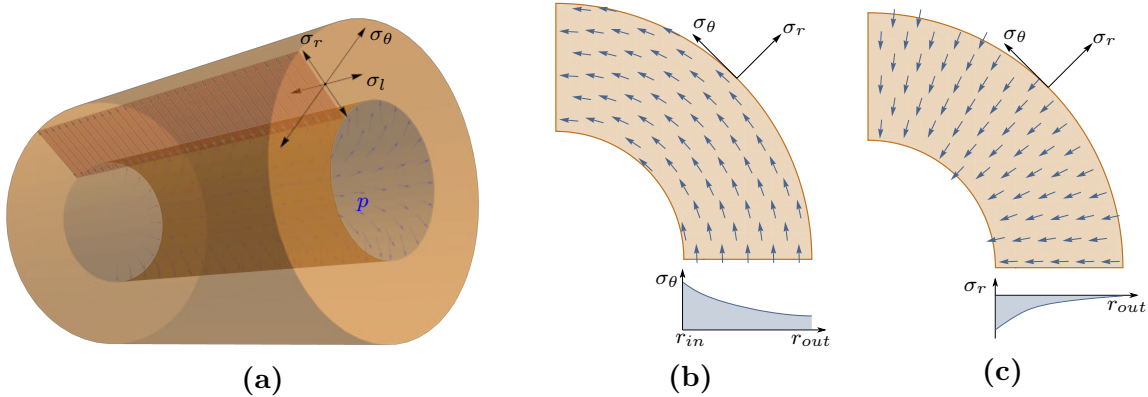


Figure 3.2: Pressurized cylinder vessel (a) with internal pressure p with circumferential (or tangential) stress σ_θ , axial stress σ_l and radial stress σ_r . Circumferential and radial stresses are highlighted in (b) and (c).

the backward Piola transform it could be related to the Cauchy stress as:

$$\mathbf{P} = J\sigma \mathbf{F}^{-T}, \quad (3.1.7)$$

where $J = \det(\mathbf{F})$ and \mathbf{F} is the deformation gradient.

The second Piola-Kirchhoff stress pull-back the force in the spatial configuration to the reference one and so it is entirely expressed in the reference configuration Ω_0 . It could be expressed as:

$$\mathbf{S} = \mathbf{F}^{-1}\mathbf{P}. \quad (3.1.8)$$

Furthermore, the Cauchy stress can be represented in a coordinate system within which the shear stress disappears. This stress state is called the principal stress state and the principal stress directions $\hat{\mathbf{n}}_i$ represent the eigenvectors of the stress state. Introducing the principal stresses σ_i , the Cauchy stress in a principal coordinate system reads:

$$\boldsymbol{\sigma} = \sigma_i \hat{\mathbf{n}}_i \otimes \hat{\mathbf{n}}_i. \quad (3.1.9)$$

Vascular vessels are cylinder-like structures that can be approximated as a typical engineering problem named as pressurized tube. Inflated vessels may be characterized by a mutual tri-orthogonal axial system representing cylindrical coordinates. For this simplified setup, the three principal directions are circumferential, axial and radial one with the related stresses shown in fig. 3.2. Due to the boundary conditions of

the problem the radial stress has to balance the internal pressure inside and the external one outside while the circumferential stresses are generated to resist the resulting bursting effect. Since the internal pressure is higher than the external one, radial stresses are generally higher inside and gradually decrease across the thickness. Circumferential stresses follow a similar trend depending on the internal pressure but also on wall thickness. For a thick-wall cylinder, they could be calculated using the Lamé equations with the resulting trend in fig. 3.2.

3.1.3 Governing laws

The motion of a material particle of density ρ is governed by the linear momentum balance equation:

$$\rho \frac{D\mathbf{v}}{Dt} = \text{div } \boldsymbol{\sigma} + \mathbf{b}_f, \quad (3.1.10)$$

where $\boldsymbol{\sigma}$ is the Cauchy stress tensor, \mathbf{v} is the particle velocity and \mathbf{b}_f is the body force per unit volume.

The balance of angular momentum is a priori satisfied by the symmetry of the Cauchy stress tensor: $\boldsymbol{\sigma} = \boldsymbol{\sigma}^T$.

3.1.4 Boundary Value Problem

In continuum mechanics, the primary unknown variable is the displacement field \mathbf{u} and this can be obtained from the solution of the Boundary Value Problem (BVP) derived from the balance of linear momentum and constitutive relations.

The body is characterized by the boundary $\partial\Omega$, split into $\partial\Omega_u$ and $\partial\Omega_t$. At $\partial\Omega_u$ Dirichlet or essential boundary conditions are prescribed in order to impose the displacement, while at $\partial\Omega_t$ Neumann or natural boundary conditions prescribe the traction through the boundary normal.

For a transient problem, the mathematical description should be closed by the initial conditions on the velocity and displacement field. hence, the BVP is described by the following set of equations:

$$\left\{ \begin{array}{ll} \operatorname{div} \boldsymbol{\sigma} + \mathbf{b}_f = \rho \frac{D^2 \mathbf{u}}{dt^2} & \text{in } \Omega, \\ \mathbf{u} = \bar{\mathbf{u}} & \text{at } \partial\Omega_u, \\ \mathbf{t} = \boldsymbol{\sigma} \mathbf{n} = \bar{\mathbf{t}} & \text{at } \partial\Omega_t, \\ \frac{D\mathbf{u}}{Dt} = \mathbf{v}_0; \mathbf{u} = \mathbf{u}_0 & \text{in } \Omega, \text{ at } t = t_0 \end{array} \right. \quad (3.1.11)$$

3.2 Finite Element Method

The Finite Element Method is a widely used method to numerically solve partial differential equations (PDE). It is a procedure based on the representation of the continuum with a finite number of points, called nodes, within the continuum body in order to discretize the full body (of arbitrary geometry) by means of a finite set of sub-regions of standard geometries called finite elements. Over every region, both the geometry and the variables of the governing equations are approximated in order to solve complex systems of equations over elaborate domains.

The governing equations are usually reformulated in the weak integral form and the finite element approximation leads to a finite set of non-linear algebraic equations in the primary variable. Then, these equations could be solved with an iterative technique such as the Newton-Rapson method.

3.2.1 Spatial description

The domain is approximated as a discretized domain segmented into n subdomains:

$$\Omega \simeq \Omega_h = \sum_{e=1}^n \Omega_e. \quad (3.2.1)$$

This discretization allows us to focus only on a single finite element Ω_e for the governing equations and material description.

The primary variables are approximated through the shape functions N_i . The latter interpolate the primary variables in space over the finite element Ω_e through their values at nodes as:

$$\mathbf{u}(\xi) = \sum_{i=1}^{n_i} N_i(\xi) \mathbf{u}_i, \quad (3.2.2)$$

where ξ represents the coordinates in the single element domain with n_i nodes.

By storing all the independent variables \mathbf{u}_i ($i = 1, \dots, n_{\text{ndim}}$) into a vector \mathbf{h} of dimension $n_{\text{dof}} = n_i n_{\text{dim}}$ the finite element interpolation can be reformulated as

$$\mathbf{u} = \mathbf{N}\mathbf{h}, \quad (3.2.3)$$

with the interpolation matrix \mathbf{N} collecting shape functions N_i .

By using an isoparametric finite element formulation, both the essential variables and the spatial coordinates \mathbf{x} use the same shape function, so:

$$\mathbf{x}(\xi) = \sum_{i=1}^{n_n} N_i(\xi) \mathbf{x}_i. \quad (3.2.4)$$

The shape functions could be defined in the natural coordinate of the finite element ξ and linked to the global coordinate \mathbf{x} through the Jacobian $\mathbf{J} = \partial \mathbf{x} / \partial \xi$. It allows us to define shape function and further numerical quadrature only for each specific typology of finite element, and then map it to the current geometries.

Due to the interpolation in eq. (3.2.3) also the symmetric spatial gradient of the essential variables could be expressed through an interpolation matrix as:

$$\text{grad}_s \mathbf{u} = \mathbf{B}\mathbf{h}, \quad (3.2.5)$$

where \mathbf{h} expresses the n_s independent components of the gradients as a single vector with the convention of $[(\bullet)_{11} (\bullet)_{22} (\bullet)_{33} (\bullet)_{23} (\bullet)_{12} (\bullet)_{12}]^T$. \mathbf{B} represents the gradient interpolation matrix and stores the gradient of the shape functions. This gradient requires the Jacobian matrix because the shape functions are expressed with respect to the natural coordinates ξ but they are derived with respect to the global coordinate \mathbf{x} . Each row of \mathbf{B} is expressed as:

$$\frac{\partial N_i(\xi)}{\partial \mathbf{x}} = \frac{\partial N_i(\xi)}{\partial \xi} : \frac{\partial \xi}{\partial \mathbf{x}} = \frac{\partial N_i(\xi)}{\partial \xi} : \mathbf{J}^{-1}. \quad (3.2.6)$$

3.2.2 Calculus of variations

Physical problems are often described by local governing equations with the description in the so-called strong form of the problem. However, FEM requires the weak or integral form in order to discretize and then solve the problem. A general method to

derive the weak form is the Calculus of Variations. Multiplying the governing equations with a test function, and then integrating over the body domain, leads to the weak form of the problem.

For a solid mechanics problem, the body occupies the initial configuration Ω and the problem is formulated with respect to the essential variable, the displacement \mathbf{u} . The state of motion is described by the displacement and its time derivatives, velocity $\dot{\mathbf{u}}$ and acceleration $\ddot{\mathbf{u}}$. They have to satisfy the equilibrium equation. Furthermore, a Dirichlet boundary Ω_u allows for prescribed displacement condition $\mathbf{u} = \bar{\mathbf{u}}$ and a Neumann boundary $\partial\Omega_t$ for traction condition oriented across the outward-normal $\mathbf{t} = \boldsymbol{\sigma}\mathbf{n} = \bar{\mathbf{t}}$. This leads to the BVP as expressed in eq. (3.1.11).

The equilibrium equation is then multiplied with an admissible variation $\delta\mathbf{u}$ and it is integrated over the body domain.

$$\int_{\Omega} \delta\mathbf{u} \cdot (\operatorname{div} \boldsymbol{\sigma} + \mathbf{b}_f - \rho\ddot{\mathbf{u}}) dv = 0. \quad (3.2.7)$$

The first term can be split following the integration by parts:

$$\int_{\Omega} \delta\mathbf{u} \cdot \operatorname{div} \boldsymbol{\sigma} dv = \int_{\Omega} \operatorname{div}(\boldsymbol{\sigma}\delta\mathbf{u}) dv - \int_{\Omega} (\boldsymbol{\sigma} : \operatorname{grad} \delta\mathbf{u}) dv. \quad (3.2.8)$$

Furthermore, the divergence theorem can be applied:

$$\int_{\Omega} \operatorname{div}(\boldsymbol{\sigma}\delta\mathbf{u}) dv = \int_{\partial\Omega} \delta\mathbf{u} \cdot \boldsymbol{\sigma}\mathbf{n} ds. \quad (3.2.9)$$

Then, the weak form can be expressed as:

$$\underbrace{\int_{\partial\Omega_t} \bar{\mathbf{t}} \cdot \delta\mathbf{u} ds}_{\delta\Pi_{\text{ext}}} + \underbrace{\int_{\Omega} \delta\mathbf{u} \cdot (\mathbf{b}_f - \rho\ddot{\mathbf{u}}) dv}_{\delta\Pi_{\text{int}}} - \underbrace{\int_{\Omega} \boldsymbol{\sigma} : \operatorname{grad}_s \delta\mathbf{u} dv}_{\delta\Pi_{\text{int}}} = 0, \quad (3.2.10)$$

where the two $\delta\Pi$ terms represent respectively the external and internal work upon the admissible variation.

It is also interesting to observe that eq. (3.2.10) correspond to the principle of virtual work when the admissible variation $\delta\mathbf{u}$ is regarded as corresponding to an admissible variation of the engineering strain $\delta\boldsymbol{\varepsilon} = \operatorname{grad}_s \delta\mathbf{u}$.

The weak form is irreducible and involves only the first-order derivative of the essential variable. So, the derivative order of the displacement field appears to be

reduced with respect to the strong form and shared with the derivative of the test function.

In non-linear mechanical problems, where large deformations are involved together with non-linear constitutive models, it is convenient to express the internal work term with respect to the reference configuration through the second Piola-Kirchhoff stress and the variation of the Green-Lagrange strain, as:

$$\delta\Pi_{\text{int}} = \int_{\Omega} \boldsymbol{\sigma} : \delta\boldsymbol{\varepsilon} dV = \int_{\Omega_0} \mathbf{S} : \delta\mathbf{E} dV, \quad (3.2.11)$$

where $\delta\mathbf{E}$ is the admissible variation of the Green-Lagrange strain.

The balance equation obtained from Eq. (3.2.11) is nonlinear and, to be solved, has to be linearized along the increment of the displacement, that is:

$$D_{\mathbf{u}}\delta\Pi_{\text{int}} = \delta\Pi_{\text{int}}(\mathbf{u} + \Delta\mathbf{u}) - \delta\Pi_{\text{int}}(\mathbf{u}) \quad (3.2.12)$$

With the direction derivative $D_{\mathbf{u}}$ along the increment of displacement $\Delta\mathbf{u}$:

$$D_{\mathbf{u}}\delta\Pi_{\text{int}} = D_{\mathbf{u}} \left(\int_{\Omega_0} \mathbf{S} : \delta\mathbf{E} dV \right) = \int_{\Omega_0} (\mathbf{S} : D_{\mathbf{u}}\delta\mathbf{E} + \delta\mathbf{E} : \mathbb{C} : D_{\mathbf{u}}\mathbf{E}) dV \quad (3.2.13)$$

where $\mathbb{C}(\mathbf{E}) = \frac{\partial \mathbf{S}}{\partial \mathbf{E}}$ is the non-linear material stiffness.

By pushing it forward to the spatial configuration:

$$D_{\mathbf{u}}\delta\Pi_{\text{int}} = \int_{\Omega} (\text{grad}_s \delta\mathbf{u} : \text{grad}_s \Delta\mathbf{u} \sigma + \text{grad}_s \delta\mathbf{u} : \mathbb{C} : \text{grad}_s \Delta\mathbf{u}) dv \quad (3.2.14)$$

There are two different contributions to the linearized internal work, that is a geometric contribution:

$$D_{\mathbf{u}}\delta\Pi_{\text{int geo}} = \int_{\Omega} (\text{grad}_s \delta\mathbf{u} : \text{grad}_s \Delta\mathbf{u} \sigma) dv, \quad (3.2.15)$$

and a material contribution:

$$D_{\mathbf{u}}\delta\Pi_{\text{int mat}} = \int_{\Omega} (\text{grad}_s \delta\mathbf{u} : \mathbb{C} : \text{grad}_s \Delta\mathbf{u}) dv. \quad (3.2.16)$$

Both terms depend on the choice of the constitutive model to be determined.

3.2.3 Discretization

Galerkin's approach uses the same interpolation for essential variable and their test function. In other words, the nodal displacements, stored in \mathbf{h} , and their admissible variations, stored in $\delta\mathbf{h}$, are interpolated with the same interpolation functions, collected in \mathbf{N} . Then the discretized weak form for the e -th finite element reads:

$$\delta h_i \left[\underbrace{\int_{\Omega_e} N_{ai} \rho N_{aj} dv}_{M_{ij}} \ddot{h}_j + K_{ij} h_j - \underbrace{\left(\int_{\Omega_e} b_{fa} N_{ai} dv + \int_{\partial\Omega_{et}} \bar{t}_a N_{ai} ds \right)}_{f_i} \right] = 0. \quad (3.2.17)$$

The K_{ij} term contains two different contributions. The material contribution leads to the material stiffness matrix of the finite element:

$$K_{\text{mat } ij} = \int_{\Omega_e} B_{ai} C_{ab} B_{bj} dv, \quad (3.2.18)$$

where C_{ab} denotes the material stiffness linked to the constitutive model.

The geometrical contribution denotes the geometric stiffness matrix:

$$K_{\text{geo } ij} = \int_{\Omega_e} \frac{\partial N_{ai}}{\partial x_c} \sigma_{ab} \frac{\partial N_{cj}}{\partial x_b} dv, \quad (3.2.19)$$

where σ_{ab} are the component of the Cauchy stress.

These integrals are commonly computed through numerical quadrature formulas.

Given n_n arbitrary admissible variation $\delta\mathbf{h}$, the discretized weak form yields to a system of algebraic equations:

$$\ddot{\mathbf{M}\mathbf{h}} + \mathbf{K}\mathbf{h} - \mathbf{f} = \mathbf{0} \quad (3.2.20)$$

This system of equations can be solved with numerical iterative methods. If the velocity and acceleration terms are different from zero also a time discretization is required.

A non-linear stationary FEM problem can be expressed as:

$$\mathbf{K}(\mathbf{h})\Delta\mathbf{h} - \mathbf{f} = \mathbf{r}(\mathbf{h}) \quad (3.2.21)$$

and iteratively solved through a numerical procedures that minimize the residuum $\mathbf{r}(\mathbf{h})$, ideally until $|\mathbf{r}| \rightarrow 0$. Adopting a Newton-Rapson iterative scheme, the current solution at step $i + 1$ is computed from the previous step i as:

$$\mathbf{h}_{i+1} = \mathbf{h}_i + \Delta\mathbf{h}|_{\mathbf{h}=\mathbf{h}_i}, \quad (3.2.22)$$

with the increment $\Delta\mathbf{h}$:

$$\Delta\mathbf{h} = - \left(\frac{\partial \mathbf{r}}{\partial \mathbf{h}} \right)^{-1} \mathbf{r} = - (\mathbf{K}(\mathbf{h}))^{-1} \mathbf{r}(\mathbf{h}). \quad (3.2.23)$$

Both the material and the geometrical stiffness matrixes are functions of the essential variable and need to be evaluated in each step of the iterative solver. Furthermore, also a load increment approach could be used. The external boundary load is incremented with a load factor and an equivalent system is solved for each load step, as two nested loops.

Further technical details for implementation with the Comsol finite element solver are described in the appendix.

3.3 3D mesh generation

Patient-specific images are obtained with Computed Tomography Angiography (CTA), a well-established tool to clinically investigate atherosclerotic diseases [1]. It uses the injection of radio-opaque substances into the blood system that acts as a contrast agent in order to help scan vessel diseases. Images are produced with a CT scanner and the contrast material help highlight the vessel's lumen. Tomographic images are then produced containing slices of the scanned body. It is possible also to obtain volumetric images where each voxel is colored based on a gray-scale proportional to the tissue X-ray attenuation, in turn connected to tissue properties.

In this thesis work, anonymized data of medical CTA from the Karolinska Institute are used. These volumetric images are processed with a segmentation software, VascuCAP (Elucid [31]). The latter is a clinically approved software to analyze tissue distribution in atherosclerotic plaque (see. fig. 3.3).

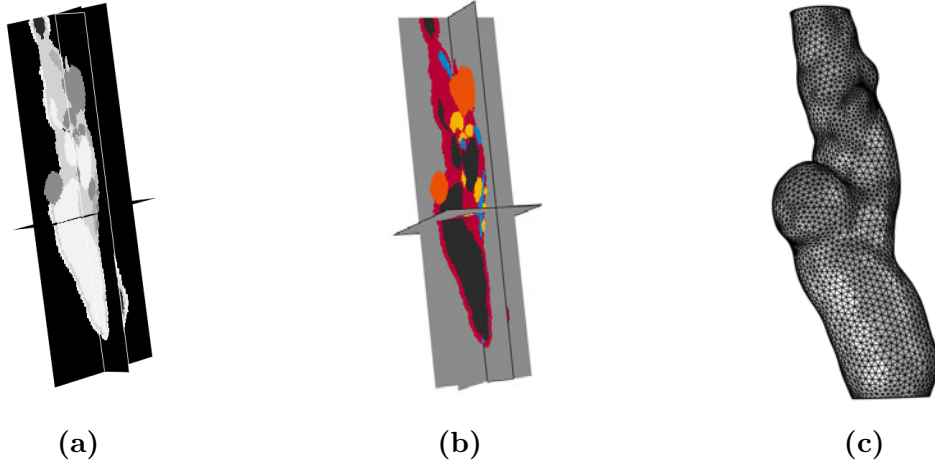


Figure 3.3: 3D volumetric reconstruction with coronal, para-sagittal and horizontal plane of CTA image (a) and tissue segmentation (b) for carotid bifurcation with atherosclerotic vessel. Example of meshed atherosclerotic carotid vessel (c).

Information about volumetric images and tissue distribution are stored into .NRRD files. These raw files are processed and converted from volumetric images into a mesh. The `iso2mesh` [48] package for Matlab [62] is used to convert volumetric binary images into a mesh. It uses voxel-based isosurfaces to generate a volumetric tetrahedral mesh. The two complete meshes are generated, representing the lumen and the vascular wall boundaries respectively. A simple boolean operation gives us the final isolated vascular wall. Eventually, smoothing, cleaning and other morphological algorithms may be included in the workflow to post-process the images, remove artifacts and assure the absence of holes in the vessel's wall.

Similar volumetric images are obtained from the segmentation containing for each voxel the tag representing a different tissue such as: lipid-rich necrotic core, calcification, intra-plaque hemorrhage or vascular tissue.

3.4 Tissue kinematics with growth and remodeling

Atherosclerosis is a multifactorial arterial disease that seems to be related to a series of chemomechanical interactions that concurs for a long time before the disease starts to be dangerous. During the development of the disease, several tissue remodeling activities occur since the vascular wall is a dynamic structure that adapts to optimize

the biological environment. Homeostatic principles in different biomechanical properties have been hypothesized, such as Wall Shear Stress, axial stress or circumferential stress [95].

In order to describe the residual strains induced by the tissue remodeling of the vascular wall, an inelastic volumetric growth term is introduced.

3.4.1 Volumetric growth

Volumetric growth can be described by introducing an intermediate configuration Ω_0 representing the stress-free state, different from the initial reference configuration $\tilde{\Omega}_0$. The deformation gradient mapping $\tilde{\Omega}_0$ to Ω can be decomposed into a growth gradient \mathbf{G} , that represents the growth-related deformation from $\tilde{\Omega}_0$ to Ω , and the classic elastic contribution of the non-growth-related deformation \mathbf{F}_e from Ω_0 into Ω . The stress-free intermediate configuration (Ω_0) can be non-compatible. Given $\mathbf{G} \neq \mathbf{I}$ also in absence of boundary load, it is possible to observe residual stresses.

Hence, the total deformation gradient read, with a multiplicative composition:

$$\mathbf{F} = \frac{\partial \chi_{tot}}{\partial \tilde{\mathbf{X}}} = \mathbf{F}_e \mathbf{G}. \quad (3.4.1)$$

Possible choices on the growth deformation gradient are, for instance, to assume an isotropic change of volume [23], that is,

$$\mathbf{G}_{iso} = \alpha \mathbf{I}, \quad (3.4.2)$$

or an anisotropic tissue growth [45], formulated with the eigenvalue representation as:

$$\mathbf{G}_{ani} = G_1 \left(\mathbf{E}_1 \otimes \tilde{\mathbf{E}}_1 \right) + G_2 \left(\mathbf{E}_2 \otimes \tilde{\mathbf{E}}_2 \right) + G_3 \left(\mathbf{E}_3 \otimes \tilde{\mathbf{E}}_3 \right). \quad (3.4.3)$$

Here, G_i represent the growth related stretches along the principal directions and \mathbf{E}_i and $\tilde{\mathbf{E}}_i$ the eigenvector respectively in the reference configuration (Ω_0) and in the initial configuration ($\tilde{\Omega}_0$).

3.5 Constitutive description

The constitutive behavior of the vascular tissues is described in the framework of rubber-like hyperelastic material approaches.

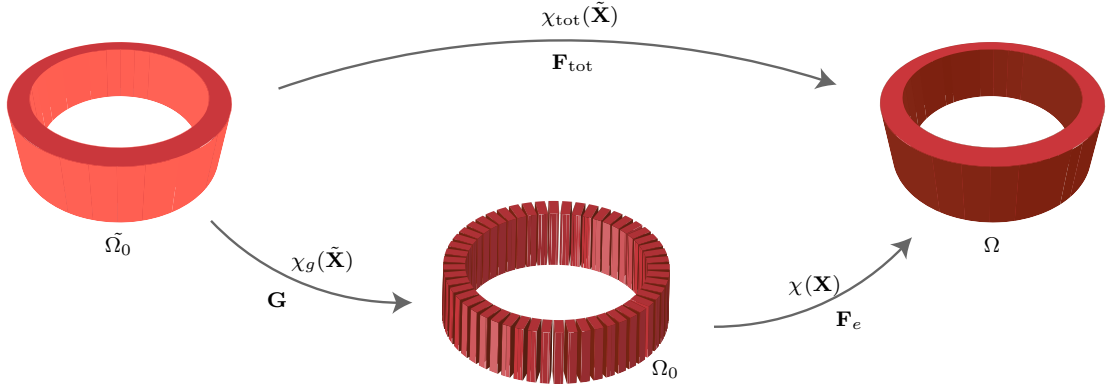


Figure 3.4: Representation of the tissue growth and remodeling through a kinematic description. The stress-free intermediate (eventually incompatible) configuration Ω_0 separates the growth-related and the non-growth-related motions. The deformation gradient is multiplicatively decomposed and the final deformation is due to both the deformation gradient and the growth tensor.

The strain energy is assumed to depend on the invariants of the elastic deformation such to ensure material objectivity requirements. By using the elastic Cauchy-Green deformation tensor $\mathbf{C}_e = \mathbf{F}_e^T \mathbf{F}_e$ as measure of deformation and assuming an isotropic response, it is possible to express the strain energy density function as a function only of the three invariants $I_{1e} = \text{tr } \mathbf{C}_e$, $I_{2e} = \frac{1}{2} [(\text{tr } \mathbf{C}_e)^2 + \text{tr} (\mathbf{C}_e^2)]$ and $I_{3e} = \det \mathbf{C}_e$, that is $\Psi = \Psi(I_{1e}, I_{2e}, I_{3e})$.

The elastic deformation of vascular tissues is modelled as perfectly incompressible. Therefore, the incompressibility constraint $J_e = 1$, with $J_e = \sqrt{I_{3e}}$, is introduced with a Lagrange multiplier approach, [39, 25]. In this case, the second Piola-Kirchhoff stress reads:

$$\mathbf{S} = 2 \left(\frac{\partial \Psi}{\partial I_{1e}} \frac{\partial I_{1e}}{\partial \mathbf{C}} + \frac{\partial \Psi}{\partial I_{2e}} \frac{\partial I_{2e}}{\partial \mathbf{C}} \right) - p \mathbf{J} \mathbf{C}^{-1} \quad (3.5.1)$$

where p is the Lagrange multiplier that represents an additional degree of freedom adding to the set of variables contained in the generalized displacement vector in eq. (3.2.3). A two-field variational problem is introduced with respect to the Lagrange

potential:

$$\begin{cases} \delta_{\mathbf{u}}\Pi_L(\mathbf{u}, p) = \int_{\Omega} \bar{\boldsymbol{\sigma}}(\mathbf{u}) : \text{grad}_s \delta \mathbf{u} dv - \int_{\Omega} p J(\mathbf{u}) \text{div} \delta \mathbf{u} dv - \delta_{\mathbf{u}}\Pi_{\text{ext}} \\ \quad = \int_{\Omega} (\bar{\boldsymbol{\sigma}}(\mathbf{u}) - p \mathbf{I}) : \text{grad}_s \delta \mathbf{u} dv - \delta_{\mathbf{u}}\Pi_{\text{ext}} = 0; \\ \delta_p\Pi_L(\mathbf{u}, p) = \int_{\Omega} \delta p (J_e(\mathbf{u}) - 1) dv - \delta_p\Pi_{\text{ext}} = 0, \end{cases} \quad (3.5.2)$$

and the linearization of the variational statements yields to:

$$\begin{cases} D_{\mathbf{u}}\delta_{\mathbf{u}}\Pi_L = \int_{\Omega} (\text{grad} \delta \mathbf{u} : \text{grad} \Delta \mathbf{u} \bar{\boldsymbol{\sigma}} + \text{grad} \delta \mathbf{u} : \mathbb{C} : \text{grad} \Delta \mathbf{u}) dv \\ D_{\mathbf{u}}\delta_p\Pi_L = D_p\delta_{\mathbf{u}}\Pi_L = \int_{\Omega} (-\text{grad} \delta \mathbf{u} : \text{grad} \Delta \mathbf{u} p \mathbf{I} + \text{grad} \delta \mathbf{u} : \bar{\mathbb{C}}_p : \text{grad} \Delta \mathbf{u}) dv, \\ D_p\delta_p\Pi_L = 0 \end{cases} \quad (3.5.3)$$

where $p = \text{tr} \boldsymbol{\sigma} / n_{\text{dim}}$ is the hydrostatic pressure, $\bar{\boldsymbol{\sigma}}$ the isochoric contribution to the stress tensor, $\bar{\mathbb{C}}$ is the isochoric contribution to the stiffness matrix, and $\bar{\mathbb{C}}_p$ is the volumetric one, [39].

We include three different materials, the vascular tissue (MATX), the calcifications (CALC) and the lipid-rich necrotic core (LRNC) with the same material descriptions of the intra-plaque hemorrhage (IPH).

Tissues distribution information is obtained from medical image segmentation. For each material, we consider an isotropic hyperelastic non-linear description following the Yeoh model [105], that has already been used to describe the components of plaque as well as vascular wall [50, 11]. The strain energy density function is dependent on the first invariant, as:

$$\Psi = \sum_1^3 c_i (I_{1e} - 3)^i, \quad (3.5.4)$$

where c_1 , c_2 and c_3 represent stress-like material parameters.

The material parameters are obtained from literature [11] and indicate in table 3.1. Extra files need to be generated to represent the tissue properties field describing how different tissues are distributed in space. Starting from the tissues identification indexes obtained from segmentation, a data structure is created through a Matlab procedure to associate each voxel spatial position with the corresponding material

	c_1	c_2	c_3
MATX	$2.35 \cdot 10^4$	$1.26 \cdot 10^5$	$1.12 \cdot 10^5$
CALC	$3.021 \cdot 10^5$	$-2.28 \cdot 10^5$	$2.61 \cdot 10^5$
LRNC	$2.96 \cdot 10^4$	$-3.32 \cdot 10^4$	$1.285 \cdot 10^5$
IPH	$2.96 \cdot 10^4$	$-3.32 \cdot 10^4$	$1.285 \cdot 10^5$

Table 3.1: Coefficient of the Yeoh constitutive model for the different tissues used in the FE analysis, expressed in Pa

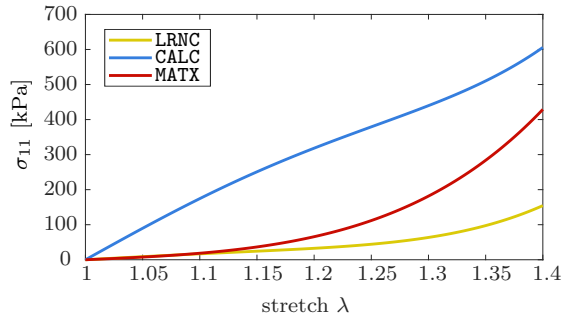


Figure 3.5: Stress vs. stretch curves for different tissue types at uniaxial extension.

coefficients c_i . Then each voxel is mapped to the corresponding mesh nodes through a global piecewise linear interpolation.

3.6 Growth formulation and algorithm

Following the homogeneous stress hypothesis, growth is here formulated such to minimize the stress gradient across the wall thickness.

The following algorithm (represented with a block diagram in fig. 3.6) is driven by the first principal stress σ_1 .

The proposed approach aims to reduce the maximum stress difference across the wall by computing a growth factor as the difference between the local stress and the average stress $\bar{\sigma}_1$ in the overall vascular tissues as:

$$\alpha = \frac{1}{c} \frac{\sigma_1 - \bar{\sigma}_1}{\max[\sigma_1, \bar{\sigma}_1]}, \quad (3.6.1)$$

where $1/c$ is a regularization factor with $c \in [2; 10]$, depending on material and geometric properties as well as on mesh quality, used to ensure a better convergence.

The average of the first principal stress $\bar{\sigma}_1$ is computed only within the vascular tissue as:

$$\bar{\sigma}_1 = \frac{\int_{\Omega} f \sigma_1 d\Omega}{\int_{\Omega} f d\Omega}, \quad (3.6.2)$$

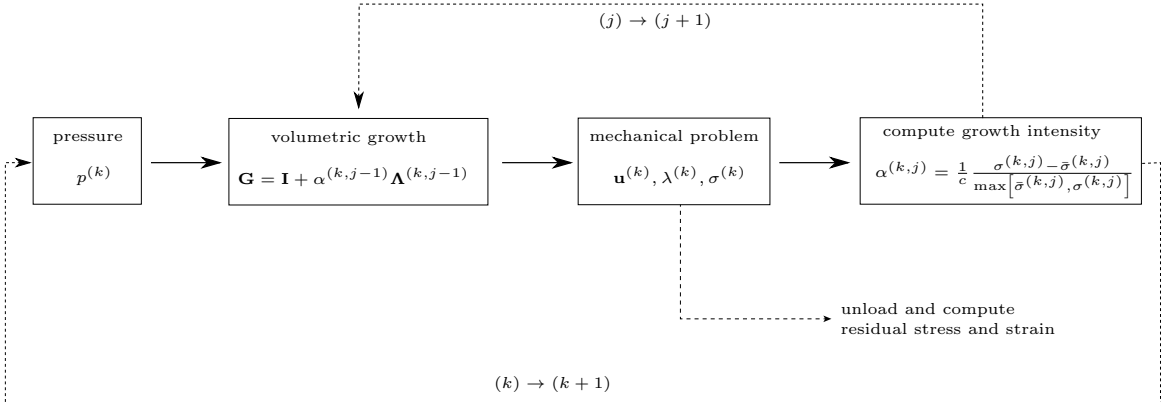


Figure 3.6: Growth algorithm that allows us to calculate the growth deformation gradient to homogenize the stress field. It is used up to mean pressure (given the oscillatory behavior of blood pressure the growth is assumed to reflect what happens at mean pressure). The k steps follow the load history to increment internal pressure from zero to the boundary condition (average blood pressure) while the j steps follow the growth scaling factor. For each step, the algorithm solves the mechanical problem and computes the stress field. Through the stresses, it is possible to compute the desired volumetric growth tensor (as described by eq. (3.6.4)) with the aim of minimizing the stress gradient. At each step, the applied growth is related to the computing at the previous step.

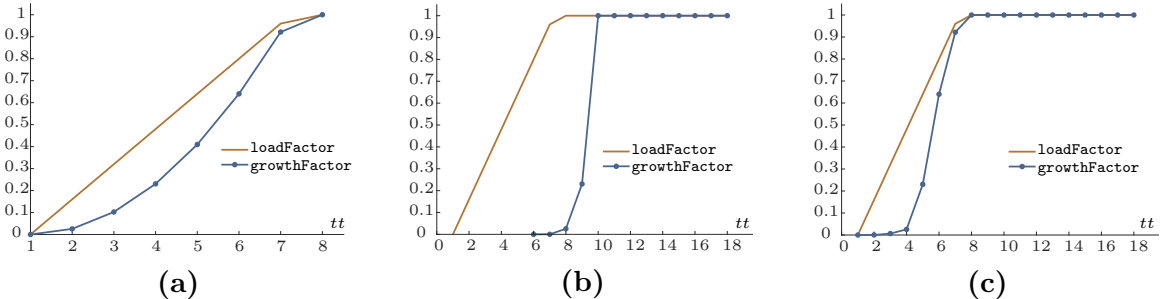


Figure 3.7: Normalized scaling factors used to modulate external load or activate growth. Different approaches are presented: in (a) growth and load are increased together until the maximum is reached, in (b) firstly the load is increased and then the growth is computed, and a hybrid approach is shown in (c). tt represent a fictitious time, while **loadFactor** and **growthFactor** represent respectively the k and j indexes shown in the general algorithm in fig. 3.6

where f is an indicator function of the vascular tissues, defined as:

$$f = \begin{cases} 1, & \in \text{MATX} \\ 0, & \notin \text{MATX} \end{cases} \quad (3.6.3)$$

The growth factor is projected along the first principal stress direction. Assuming a null rigid rotation during growth, the growth tensor is defined as:

$$\mathbf{G} = \mathbf{I} + \alpha \underbrace{(\hat{\sigma}_{1e_1} \mathbf{e}_1 \otimes \mathbf{e}_1 + \hat{\sigma}_{1e_2} \mathbf{e}_2 \otimes \mathbf{e}_2 + \hat{\sigma}_{1e_3} \mathbf{e}_3 \otimes \mathbf{e}_3)}_{\Lambda}. \quad (3.6.4)$$

Here, Λ is used to project the growth across the first principal stress direction in the global reference system ($\mathbf{e}_1, \mathbf{e}_2, \mathbf{e}_3$). Quantities, $\hat{\sigma}_{1ei}$ represent the normalized principal direction components with respect to the corresponding global reference axis \mathbf{e}_i :

$$\hat{\sigma}_{1ei} = \frac{(\sigma_1 \mathbf{n}_1) \cdot \mathbf{e}_i}{\sigma_1} = \mathbf{n}_1 \cdot \mathbf{e}_i, \quad (3.6.5)$$

where \mathbf{n}_1 represents the first principal stress direction and $i = 1, 2, 3$ the index running over the global reference directions.

The proposed algorithm allows the vascular tissues to redistribute in order to minimize the local differences in the first principal stress. Preliminary numerical analyses showed that using the first principal stress, and not averaged quantities as the Von Mises stress, numerical instability problems are avoided. In fact, a Von-Mises driven growth would correspond to an isotropic rational. In this case, instability issues might occur due to the required fixed constraints of the upper and lower vessel's end since isotropic growth can induce extra compressive loads perpendicularly to these constraints. Furthermore, it also allows us to confer directionality to the growth, driven by the highest tensile stresses. This reflects several aspects of biology where responses are anisotropic in space due to different stimuli in different directions.

It is noteworthy that the growth tensor applies only to vascular tissue, being not applied to both calcifications and lipid-rich necrotic core. Both calcification and lipid core do not seem to respond to local stress stimuli.

Due to the high non-linearities, the load and the growth intensity are modulated by independent scaling factors that are progressively increased in order to reduce numerical problems (see fig. 3.7).

Three different approaches are proposed. Due to the pulsatile behavior of the blood pressure and the long-term homeostasis of the vascular wall, not the entire

blood pressure waveform is followed but rather its time average. It is known as the mean arterial blood pressure defined as:

$$\text{MAP} = \frac{1}{T} \int_0^T p(x, t) dt \simeq \frac{1}{3} p_{sys}(x) + \frac{2}{3} p_{dias}(x), \quad (3.6.6)$$

where T is the duration of a cardiac cycle, and p_{sys} and p_{dias} are the systolic and diastolic blood pressure. The proposed approaches are triggered by the MAP in carotid arteries.

The first approach firstly increases the load and computes the stress state induced by the MAP, then switches to the growth computation through a staggered coupled formulation between each growth step and the mechanical analysis bases on MAP boundary conditions (see fig. 3.7a). The second approach follows the same staggered coupled formulation, however, it computes the growth at each load step (see fig. 3.7b). A third hybrid approach is proposed with the computation of growth at each load step and an extra growth loop once reached the MAP trigger (see fig. 3.7c).

In all approaches, a linear law is used to increase the external load and a quadratic one is used to slow down the growth at the initial steps.

The stopping criterion of the growth algorithm is evaluated in terms of the normalized deviation from the average homogenized stress, computed as:

$$\Delta\sigma_j = \frac{\sum_{i=1}^N |\sigma_i - \bar{\sigma}_1|}{N\bar{\sigma}_1}, \quad (3.6.7)$$

where N represents all the nodes and $\bar{\sigma}_1$ the average homogenized stress for each growing step j .

3.7 Synthesis of the complete workflow

The complete model starts from the volumetric images obtained from medical CTA with segmentation and tissues distribution directly from clinical-approved software. Volumetric images are converted with `iso2mesh` [48] into a structural mesh that is imported in the Comsol simulation environment [24], assigning different material properties to the different tissue domains as obtained from segmentation. $2 \cdot 5^3$ elements are used with quadratic shape function for the displacement and constant one for the auxiliary pressure. Both vessel's ends are fixed. To numerically solve the high non-linearity a load multiplier is introduced, increasing the internal pressure incrementally. The growth algorithm works until the average pressure is reached and the stopping criterion is satisfied. After the growth phase, the pressure is further increased near the systolic or higher pathological values to analyze the stress distribution or search for the risk of rupture. Moreover, it is possible to unload the vessel and remove external constraints to investigate residual strains.

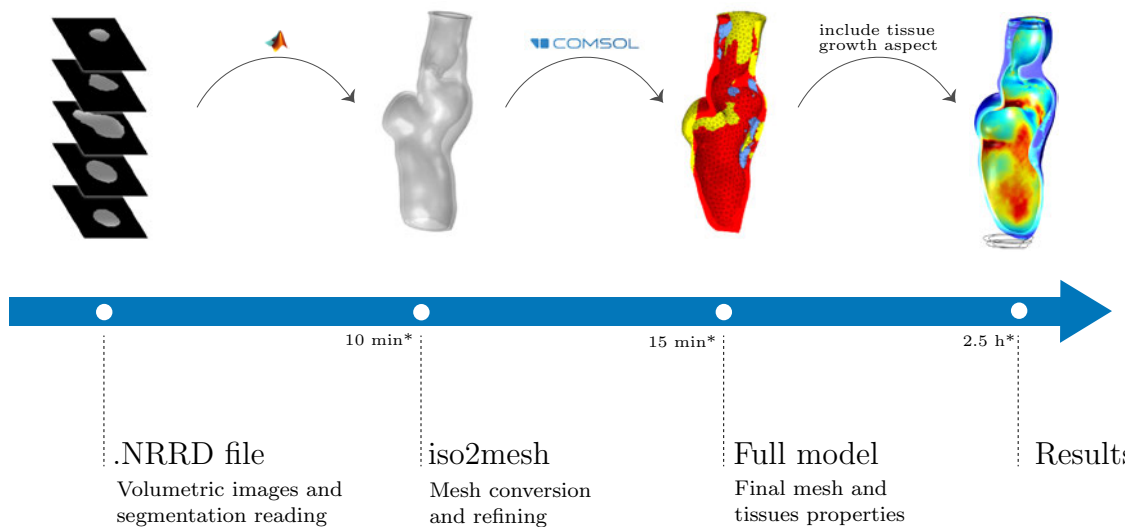


Figure 3.8: Generic workflow for the model. It starts with a conversion from medical images into a mesh, segmenting the images such to distinguish between the properties of the different tissues. The STL mesh models are imported into Comsol material properties assigned through a Matlab procedure. Finite element simulation routines in Comsol are employed to compute the finite element solution and investigate the stress state and residual strains. (*) Solving times are referred to a Windows11 workstation with i7-10850H and 32 GB RAM at 2933 MHz.

Chapter 4

Results

The results are divided into three sections, each will be discussed in order. After a brief discussion on the implementation of the growth procedure, the first section deal with a simple geometry representing a perfect cylinder used as a benchmark to better analyze the growth algorithm. The second and third sets of results analyze the real carotid disease case focusing on several specific slices, where the lumen is the tightest. The second shows the tissue remodeling effect, while the third one focuses on the effect over the peak stress and the stress distribution.

4.1 Benchmark case study

In order to better assess the growth algorithm an ideal cylindrical case is used. The geometry is similar in size to real blood vessels and is detailed in the appendix (fig. 5.1a). The material is considered homogeneous described by the MATX parameters.

By applying an internal pressure equal to the average vascular pressure near the carotid arteries it is possible to analyze the growth algorithm. A comparison between the standard FEM analysis and the growth model is shown in fig. 4.1.

Without considering growth, the standard analysis shows higher stresses on the internal side of the cylinder that gradually decrease across the thickness. The growth algorithm allows to obtain a general homogenization of the stress, with an evident reduction of the stress gradient along the vessel thickness, fig. 4.1b.

In a second case study, a general inclusion is considered to better evaluate the influence of non-remodeling tissues. The inclusion (see fig. 4.2b) is assumed to have

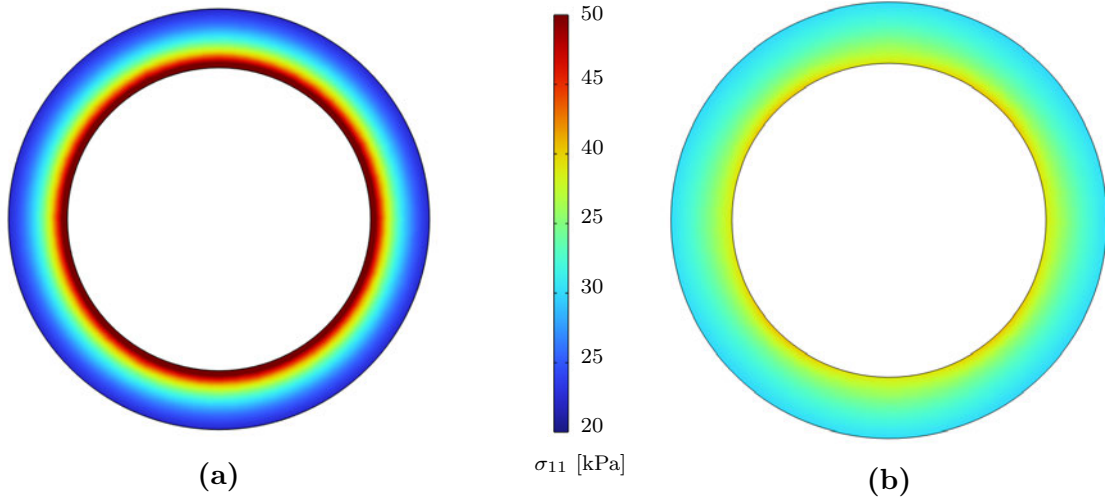


Figure 4.1: First principal stress for the inflated cylinder on standard (a) and growth (b) formulation on a half-height plane. It is possible to observe the stress homogenization in the analysis with the tissue growth. In the standard analysis, the stress varies from more than 50 kPa to less than 20 kPa. Instead, in the growth formulation stresses appear to be in a more restricted range.

material properties of calcification (**CALC**).

The growth algorithm works only on the vascular tissue and it corresponds to strong changes in the stress or strain distribution at the interface between different tissues. As shown in fig. 4.3 we can see a general homogenization in stress intensity with a reduction in the higher stress area. Furthermore, the difference between the higher and the lower stress is reduced in order to obtain a more uniform stress state across the thickness with respect to the one obtained without growth.

Despite the presence of the spherical inclusion of different materials, the homogenization algorithm works in the direction of interest. Moreover, despite the inclusion is not undergoing a growth process, it plays a fundamental role, since it creates a local high stress gradient driving the growth of the vascular tissue.

By unloading the vessel, it is possible to investigate the residual strains in the two benchmark case studies. As expected we can observe a general positive residual strain inside, representing a tensile state, and a general negative strain outside. Residual strain values appear to be as high as 10% and around -10% outside. The case with the

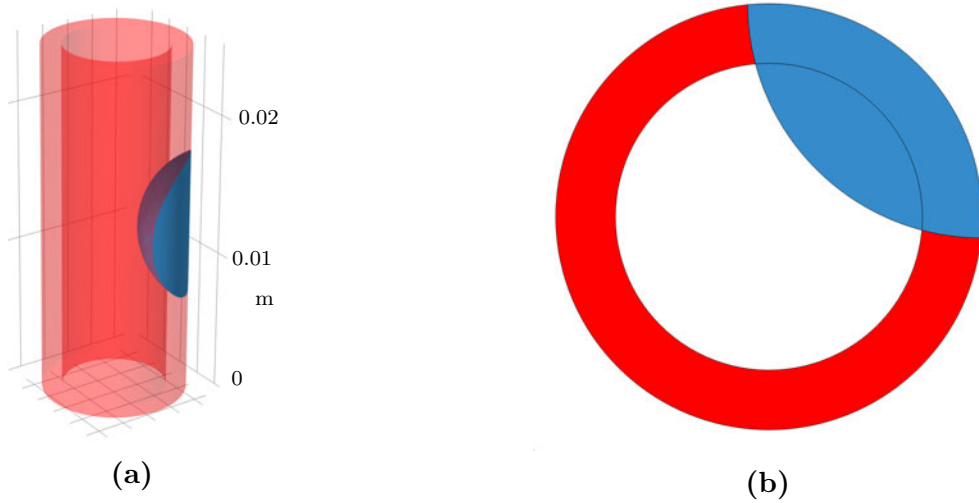


Figure 4.2: Ideal cylinder with the inclusion. The red domain ■ presents MATX material properties and the blue one ■ presents CALC material properties.

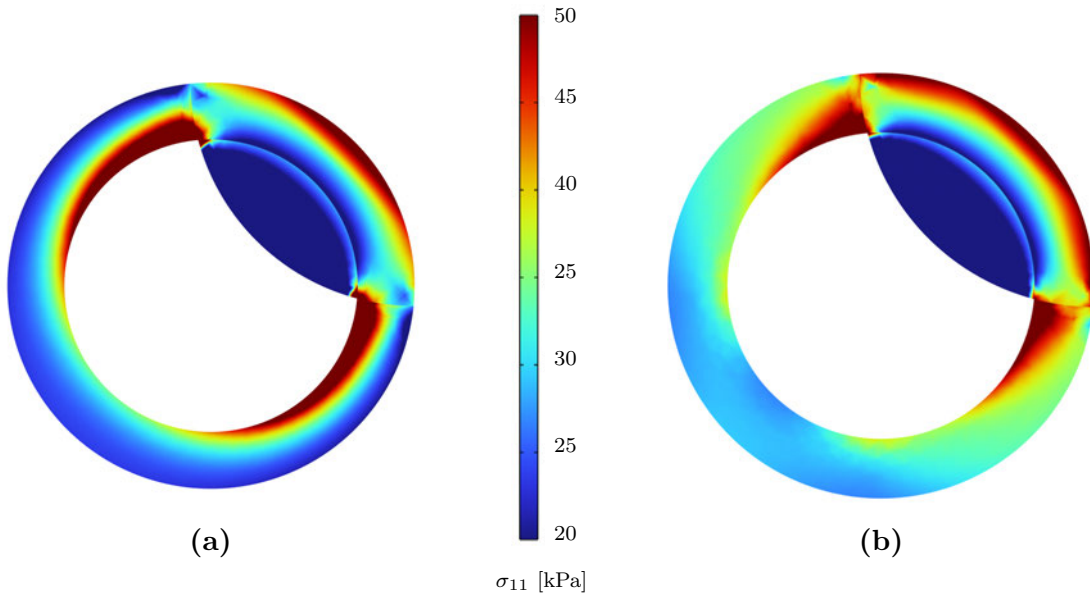


Figure 4.3: First principal stress for the inflated cylinder with inclusion (as calcification) on standard (a) and growth (b) formulation on a half-height plane. The stress pattern appears similar however in the growth formulation peak stresses are lower. The stress gradient across the wall appears to be reduced.

inclusion (fig. 4.5b) is a little more complex and the presence of the inclusion, inert to growth, reflects higher volumetric strain near the boundary of the different materials.

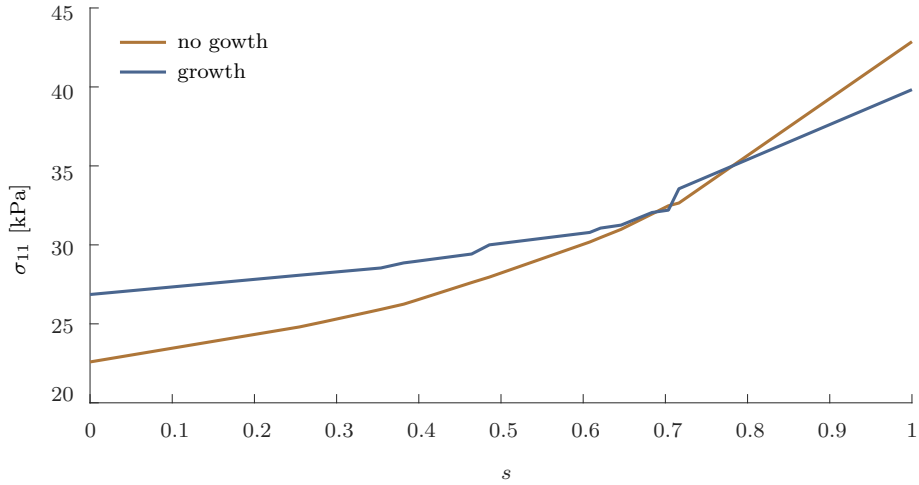


Figure 4.4: First principal stress over a cut line across the wall lumen (c), the coordinate s varies from zero, outside the wall, and 1 at the internal side. It is possible to observe how the stress difference is reduced by more than 50%.

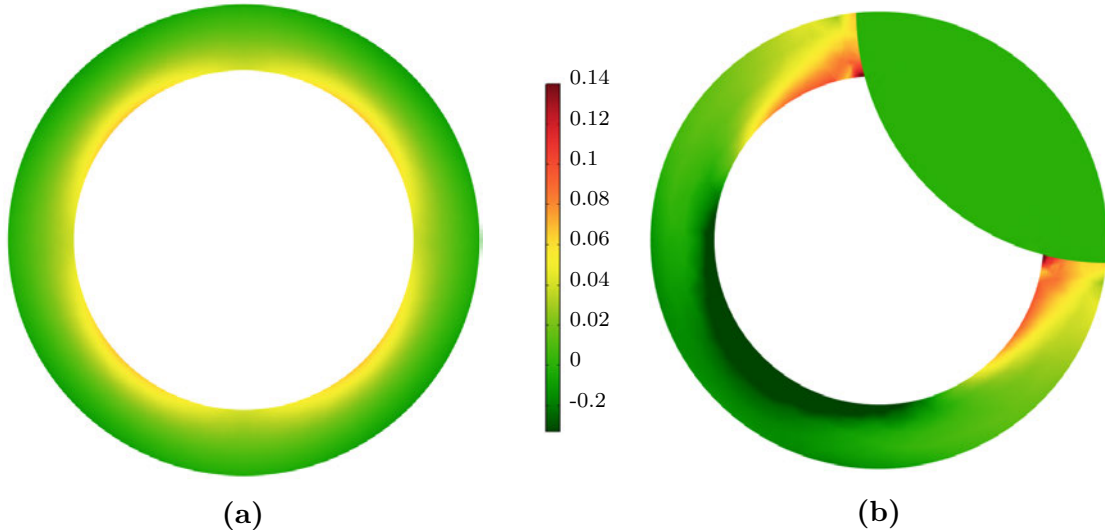


Figure 4.5: Residual strain for inflated normal cylinder without (a) and with (b) inclusion. Volumetric strain is shown on a half-height plane. The residual strain appears positive inside and slightly negative outside. In the simple cylinder (a), the positive strain is up to 10% instead the negative one is slightly lower than expected. For the case with inclusion (b) the residual strain appear higher where the peak stress was identified, right at the interface between the inclusion and the vascular tissue. Clearly, in the inclusion it is zero considering that the growth algorithm does not work on tissues other than the vascular one (MATX).

The pattern of positive internal and negative external strains is still present.

It is also noted that the fields in the ideal cylindrical geometries do not have exact polar symmetry (with respect to the center) and this is due to asymmetries in the mesh, see fig. 5.1a in Appendix.

4.2 Patient-specific case study

In order to practically apply the algorithm to real carotid arteries several medical volumetric images from different patient CTAs are considered. In the following, results from the most interesting case are reported (fig. 4.6a).

A volumetric three-dimensional reconstruction is shown in fig. 4.6 together with the most interesting slice. In this slice, the lumen is the tightest and the plaque tissue appears large and filled with lipid-rich tissue.

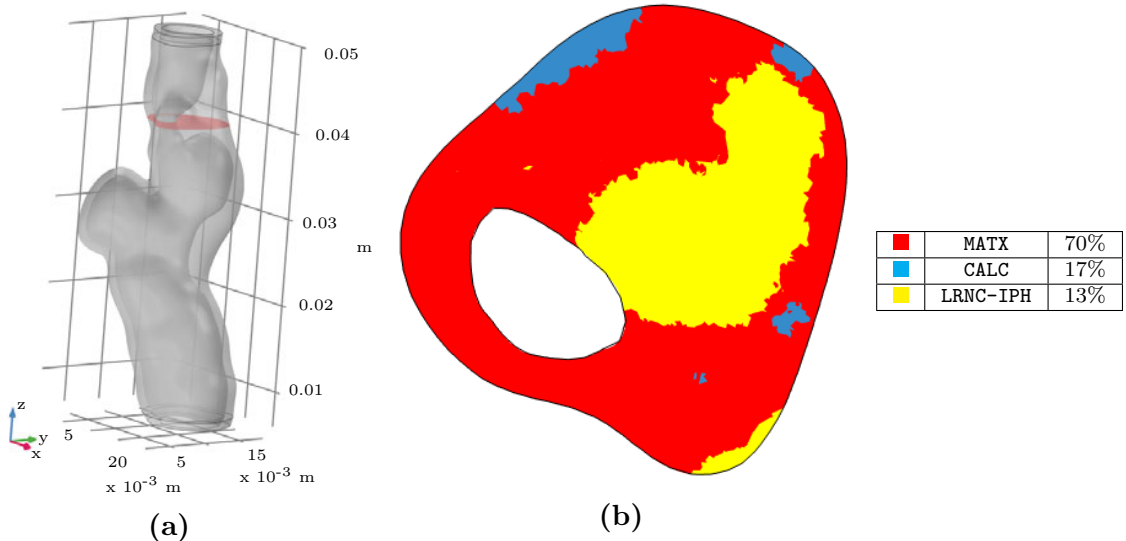


Figure 4.6: 3D reconstruction of the vessel for patient ID 643(a); Slice of interest (b) with different materials highlighted with different colors. In the table also the percentages of the constituents are shown for the whole vessel.

A mesh sensitivity analysis is conducted in order to investigate the optimal mesh density. Due to the multiple material descriptions of the problem it is interesting to account for a stable mesh able to distinguish between different tissue details without a too high computational cost.

Given the growth-related quantities of interest, the chosen mesh converge criterion is a measure of the variation in stress distribution measured through the normalized root mean square error of the differences between the discrete probability density

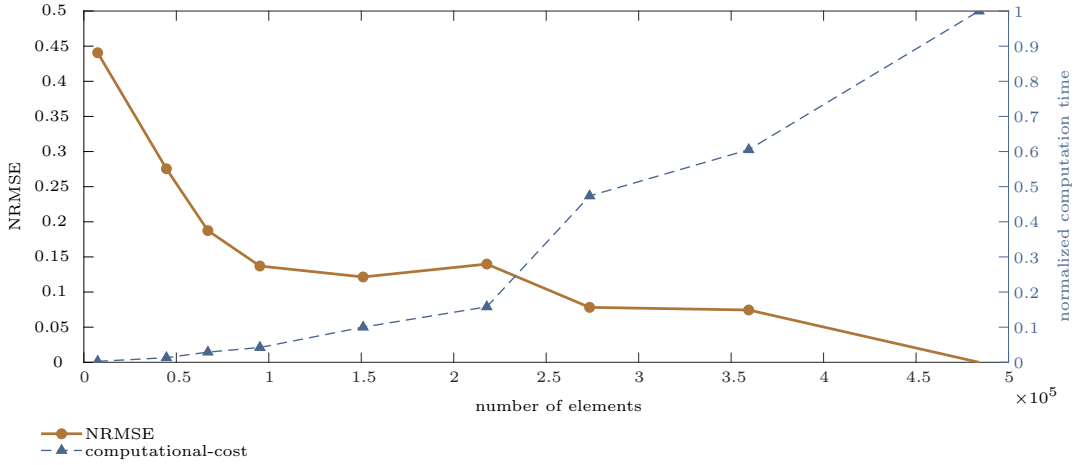


Figure 4.7: Mesh sensitivity analysis showing how NRMSE decrease with increasing in number of elements. Also the normalized computational time respect to the maximal one is shown.

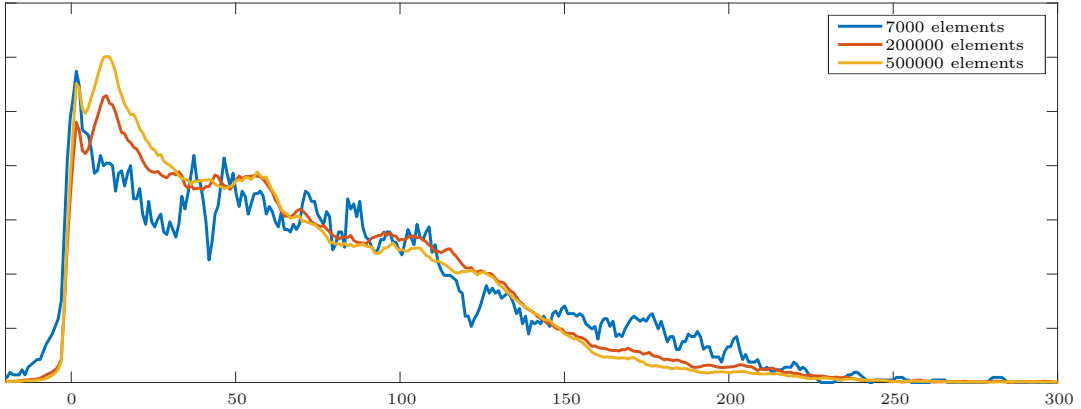


Figure 4.8: Stresses distributions obtained from meshes with a different number of elements.

functions of the stress distribution obtained at different mesh densities, that is:

$$\text{NRMSE} = \frac{\sqrt{\frac{1}{N} \sum_i^N |h_j - h_{true}|^2}}{\text{std}(h_j)}, \quad (4.2.1)$$

where j represents the selected mesh level and h is the discrete probability density function of the computed stress sampled in N intervals and h_{true} is the one referred to the mesh with the higher number of elements. Numerical results are shown in fig. 4.7.

A mesh with $2 \cdot 10^5$ elements is selected as the optimal between accuracy and solving time requirements.

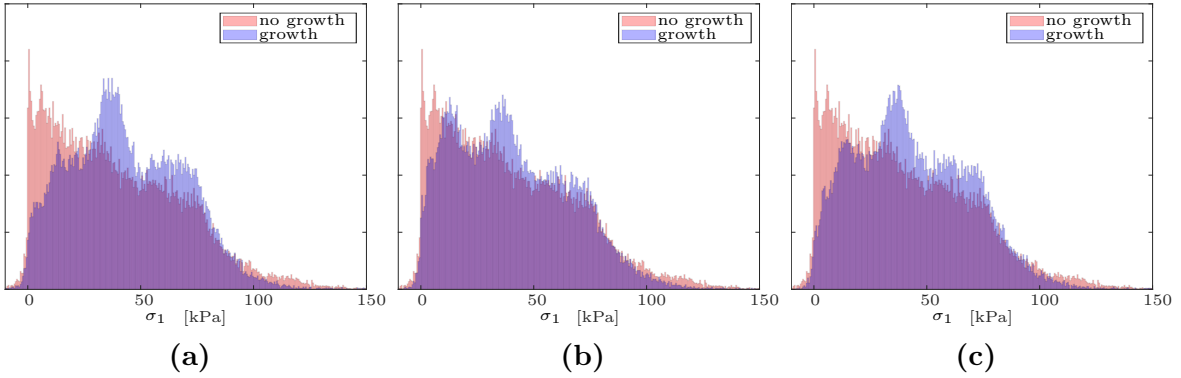


Figure 4.9: Comparison of the stress distributions between formulation with and without growth for the first (a), second (b) and third (c) proposed approaches of load-growth relation.

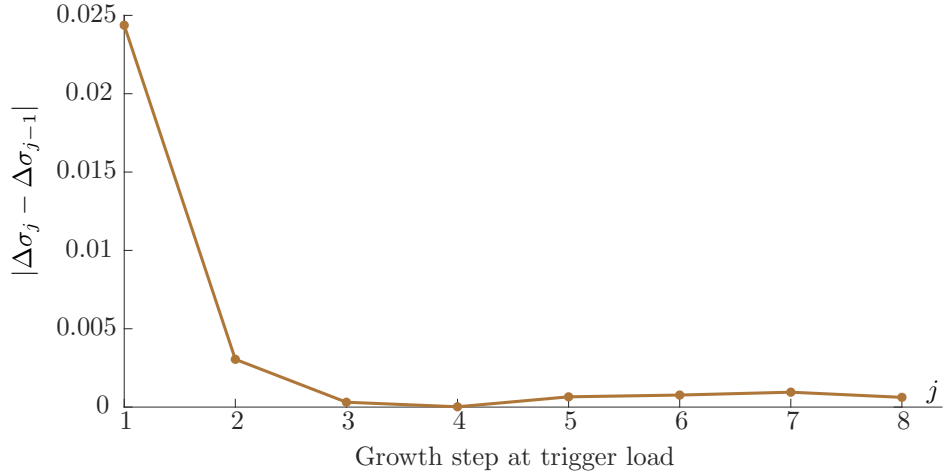


Figure 4.10: Relative normalized deviation (see eq. (3.6.7)) of the local stress from the averaged homogenized stress for each growing step j after reaching the trigger load for the patient-specific case for the hybrid approach.

The scaling factor, introduced in eq. (3.6.1), is set as $c = 4$ for patient ID 643, $c = 2$ for ID 710, $c = 10$ for ID 753 and $c = 8$ for ID 779.

4.2.1 Comparison between growth-load approaches

As introduced in section 3.6, three different approaches have been proposed showing different relations between the load multiplier and the growth scale factor.

From a theoretical viewpoint, it may be more consistent to first reach the trigger load (MAP) and then introduce the growth loop. However, this approach (i.e. the first

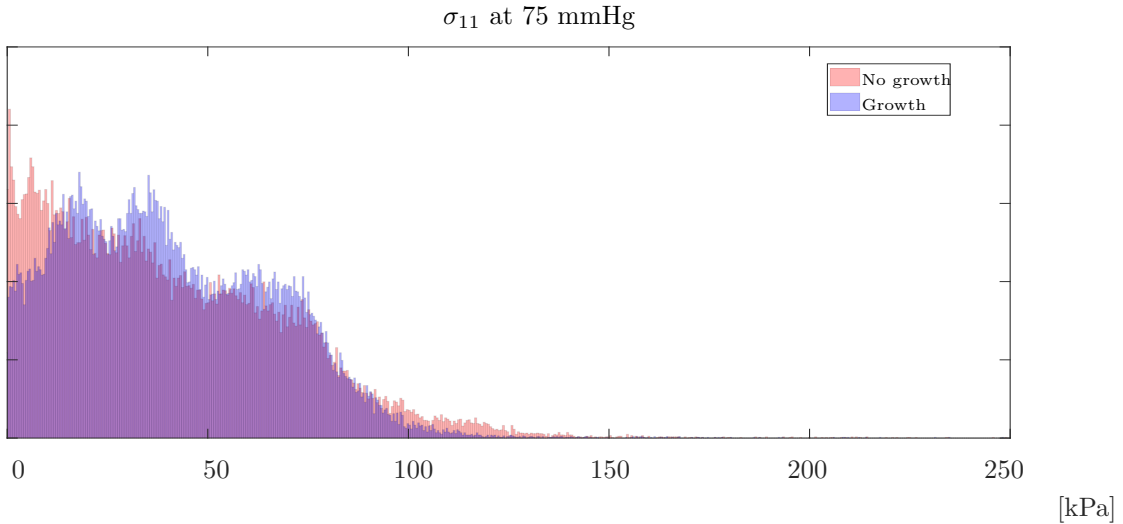


Figure 4.11: First principal stress distribution in the whole vessel at average pressure where the reduction of the peak stresses is strongly evident.

one in fig. 3.7a) requires at least half more steps to produce good results. The second presented approach links each load step with a corresponding growth computation until the MAP is reached. Computation cost is drastically reduced however it doesn't guarantee fully accurate growth results at the last step. To reduce this inconsistency a third approach is introduced where the growth algorithm works for each loading step gradually increasing both load and growth until the MAP is reached. Then, it performs the growth loop with this fixed pressure until the convergence criterion eq. (3.6.7) is satisfied as shown in fig. 4.10.

As shown in fig. 4.9, all the proposed approaches lead to a more homogenous stress state. The second one presents a slight deviation with respect to the first and third ones that appear very similar to each other. Both first and third approach compute more than a single step after reaching the target pressure, however the third one takes approximately half the step.

In the following patient-specific cases we used the third hybrid approach stopping the procedure after four extra steps later on reaching the MAP.

The comparison between the non-growth (standard) and the growth formulation is shown in fig. 4.12 at the average pressure.

In the analysis with the tissue remodeling, a more homogenous stress field appears,

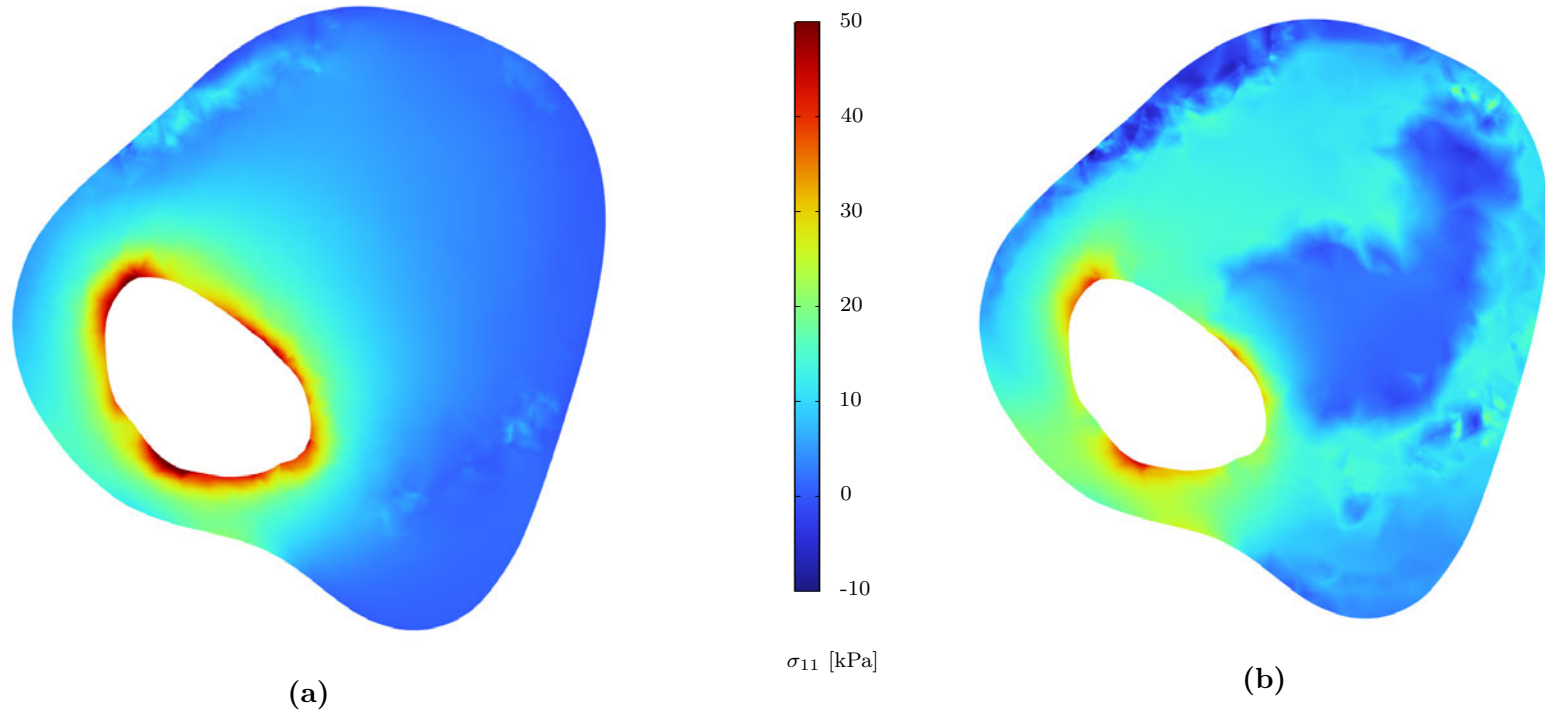


Figure 4.12: First principal stress field on the slice of interest with a boundary condition of **average blood pressure** and comparison between the standard (a) and the growth (b) analysis. The standard analysis shows a well-evident gradient of the stress across the wall thickness. Instead, by considering the growth algorithm (b), a more homogenous stress field is obtained. Furthermore, the peak stresses appear to be reduced. The lipid region, due to the more compliant behavior, appears to be less active in loading stress by considering the tissue redistribution.

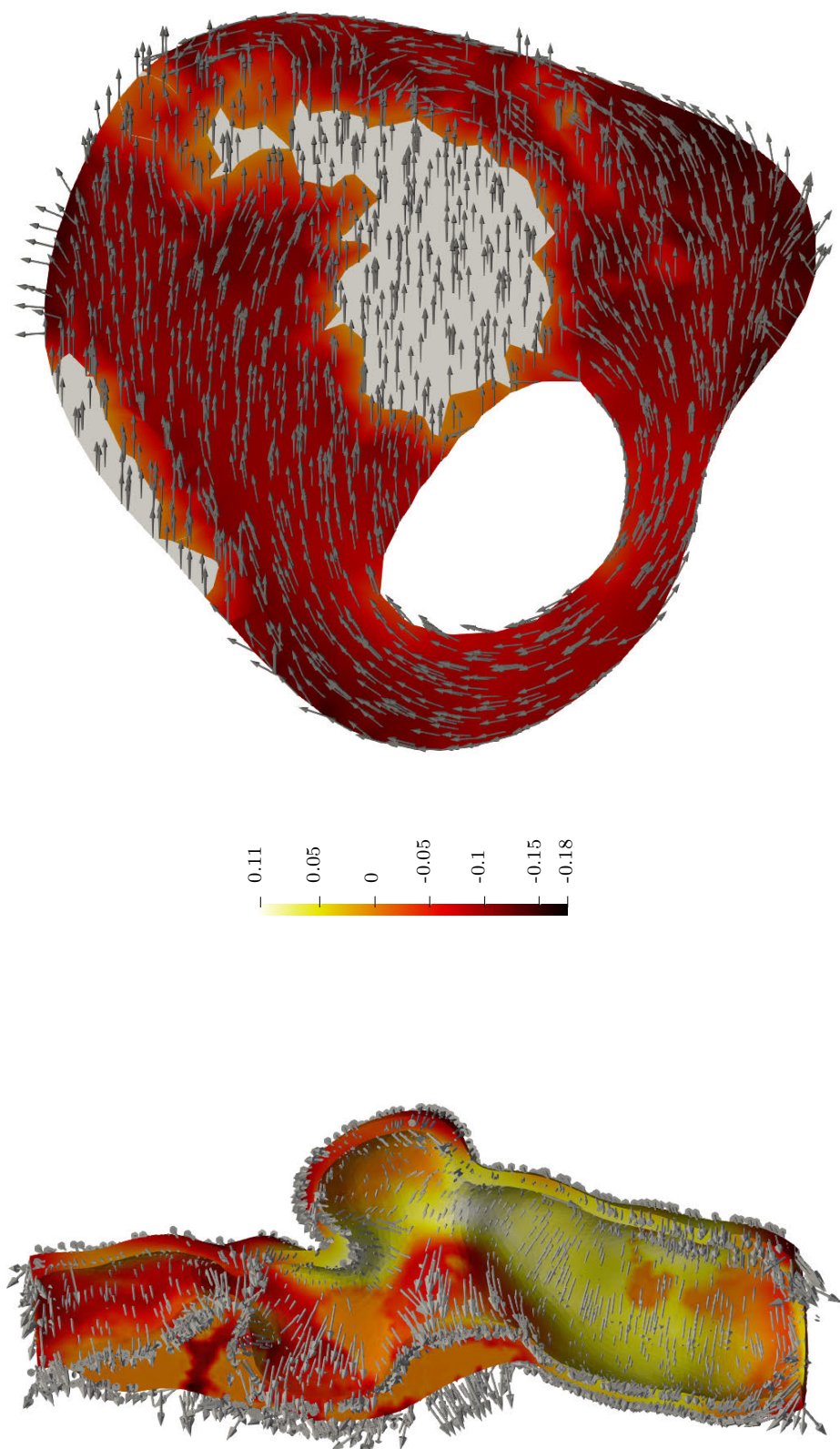


Figure 4.13: Residual growth intensity as volumetric strain represented through the color map and main growth direction computed at average pressure plotted over half vessel (left) and slice of interest (right).

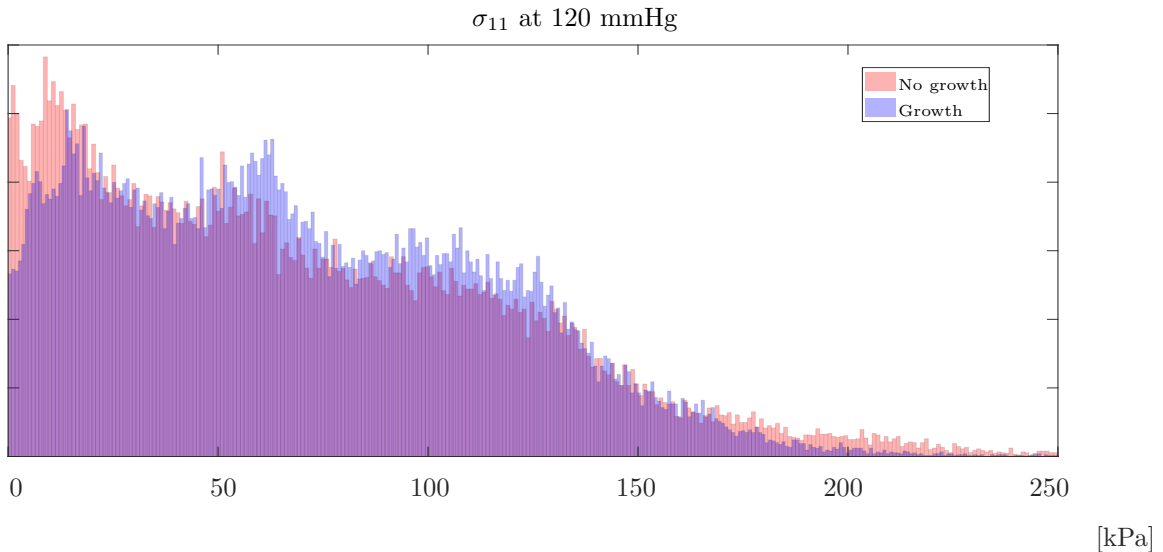


Figure 4.14: First principal stress distribution in the whole vessel at physiological systolic pressure.

as shown in fig. 4.11. Furthermore, the peak stresses on the internal side seem to be reduced. The growth process also highlights the differences between the vascular tissue and the lipid-rich area that is less involved in carrying the pressure load due to the different tissue properties.

4.2.2 Stress analysis

In order to better assess the rupture risk, the blood pressure is increased up to the systolic one, by maintaining the growth fixed to the one established by the average pressure. This reflects the physiological conditions induced by the oscillatory behavior of the pressure. While the homeostatic growth effect is regulated by the average condition throughout the time, the peak stress is related to the maximal pressure reached during the cardiac cycle in the systolic phase.

The stress fields are shown in fig. 4.15 for both the standard and the growth formulation. The standard formulation shows higher stress in the internal side of the vessel, as an annulus, with a high gradient through the wall thickness. Instead, the analysis including the tissue remodeling shows a relatively homogenized field and a significant reduction in the peak stress (up to 30%).

The size of the areas with higher stresses appears to be reduced with respect to a

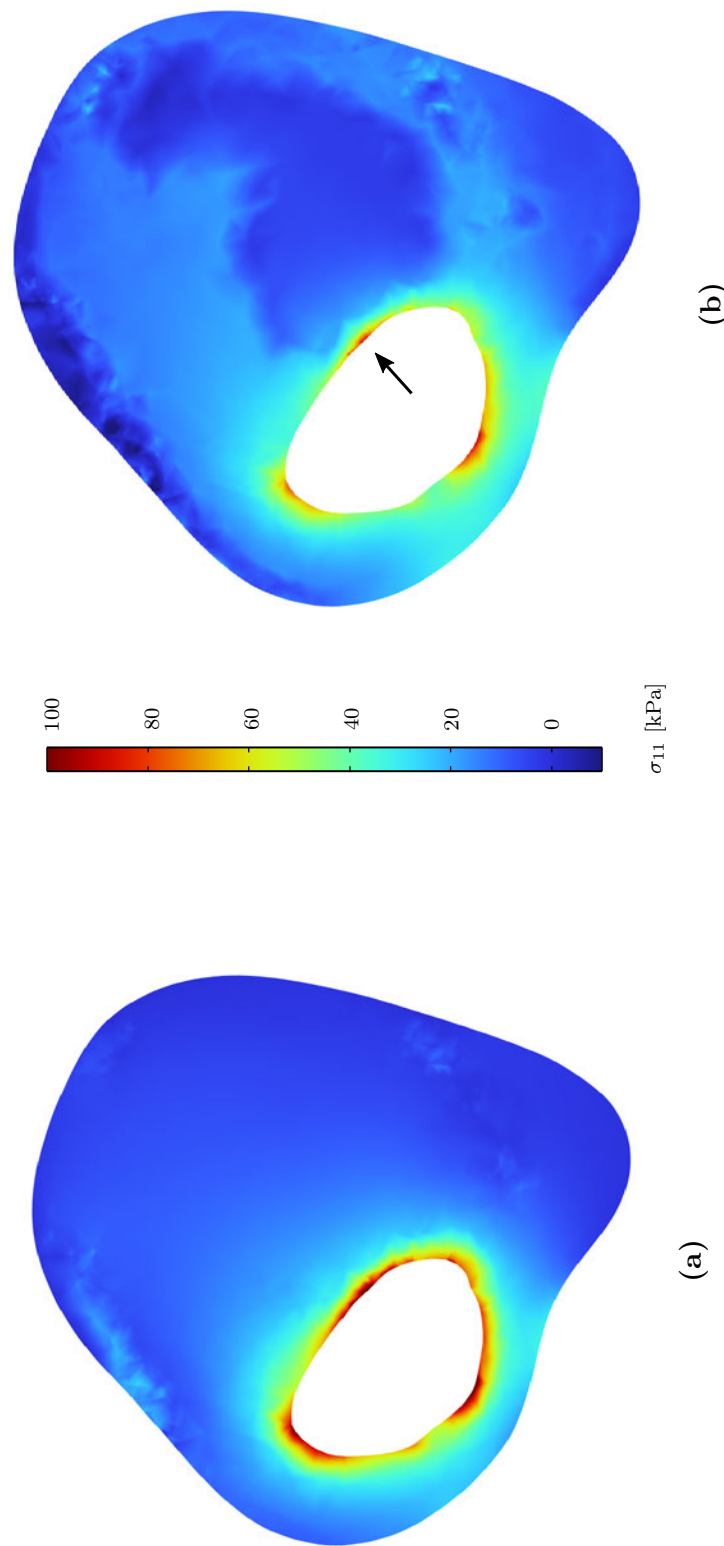


Figure 4.15: First principal stress field on the slice of interest with a boundary condition of systolic blood pressure and comparison between the standard (a) and the growth (b) analysis. The standard analysis shows a well-evident gradient of the stress across the wall thickness. Instead, by considering the growth algorithm (b), a more homogenous stress field is obtained. The stress pattern is similar to the average pressure (fig. 4.12) however notice that the color scale is doubled. In the solution with the growth formulation, the peak stress appears to be strongly reduced. Furthermore, it is interesting to observe how the area with higher stress is localized near the fibrous cap (arrow).

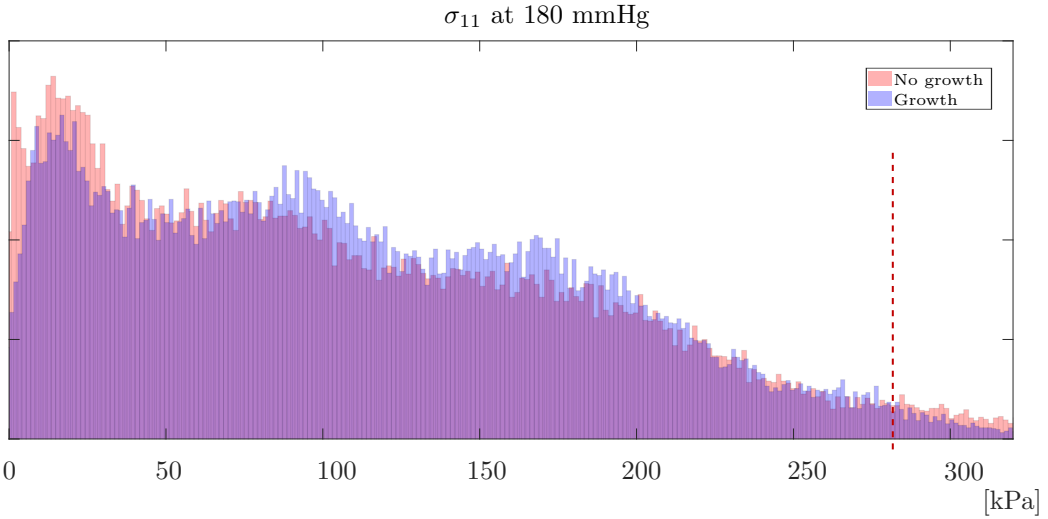


Figure 4.16: First principal stress distribution in the whole vessel at hypertension pressure.

standard analysis without considering growth. This is true for both the slice and the entire structure, as shown also by the histogram in fig. 4.14. Due to the occurrence of growth, the stress distribution appears more concentrated around average stress values.

Despite the growth being computed at average pressure, it propagates its effect up to the systolic one with still evidence of stress intensity reduction at the lumen side of the wall. Furthermore, due to the confinement of the growth to the vascular tissue also the localizations occurring at the interface between different tissues is highlighted. As expected the lipid-rich necrotic core shows a less load-carrying behavior with respect to the main MATX bulk of the slices. This is also evident by observing the plaque side, where the presence of the calcification leads to a lower stress state as shown in fig. 4.15b.

Peak stresses at systolic pressure are significantly lower than the critical limit of 300 kPa, the typical values used to indicate plaque rupture [11]. However, the histogram gives a more complete and detailed description of the full vessel stress state.

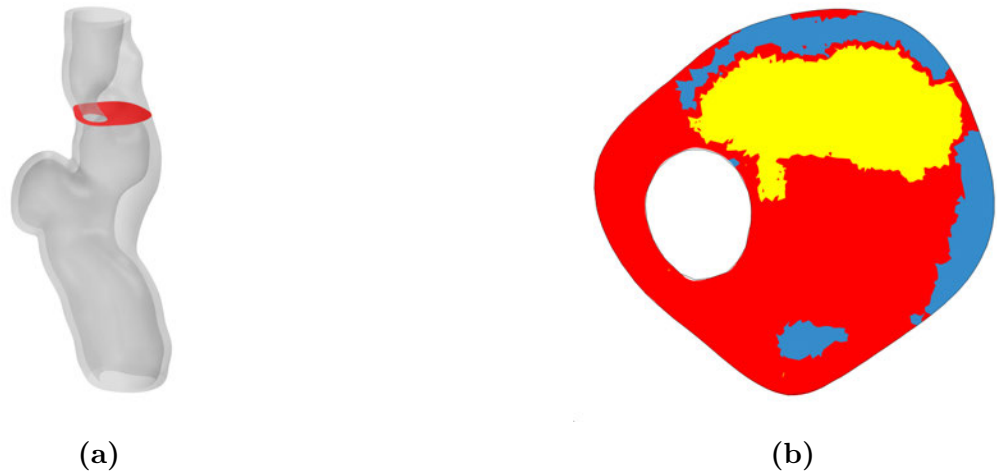


Figure 4.17: Second slice of the first patient-specific analysis: the slice of interest (a) and the tissues distribution (b).

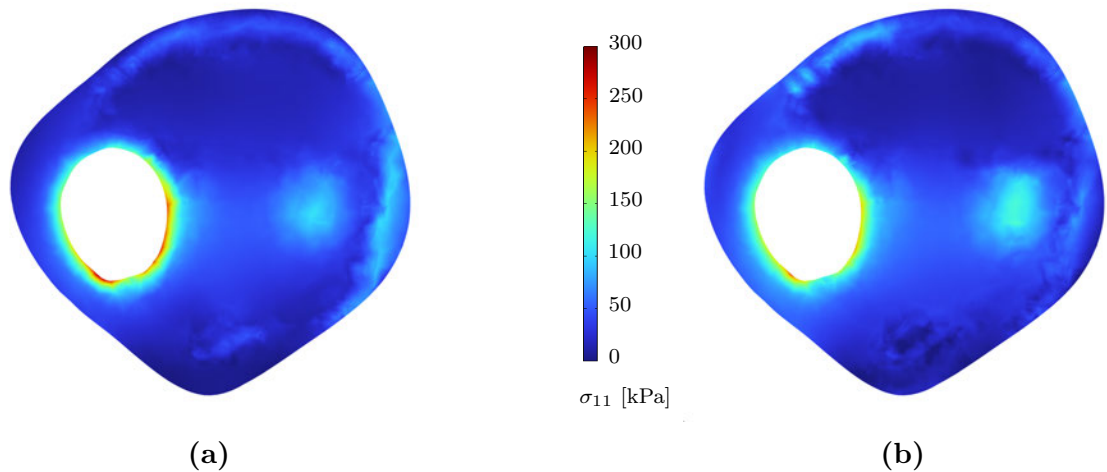


Figure 4.18: First principal stress field on the second slice of interest with a boundary condition of 180 mmHg and comparison between the standard (a) and the growth (b) analysis. The growth one shows a reduction of peak stresses and a more homogenous stress field.

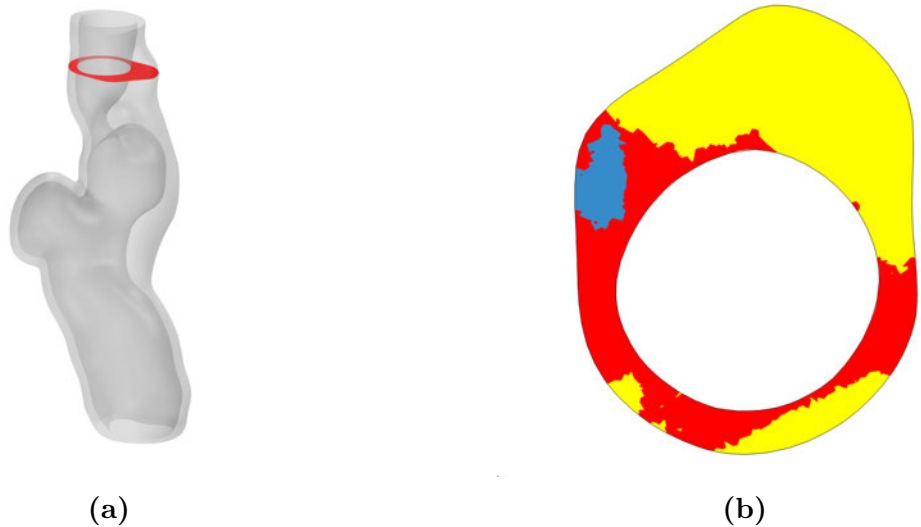


Figure 4.19: Third slice of the first patient-specific analysis: the slice of interest (a) and the tissues distribution (b).

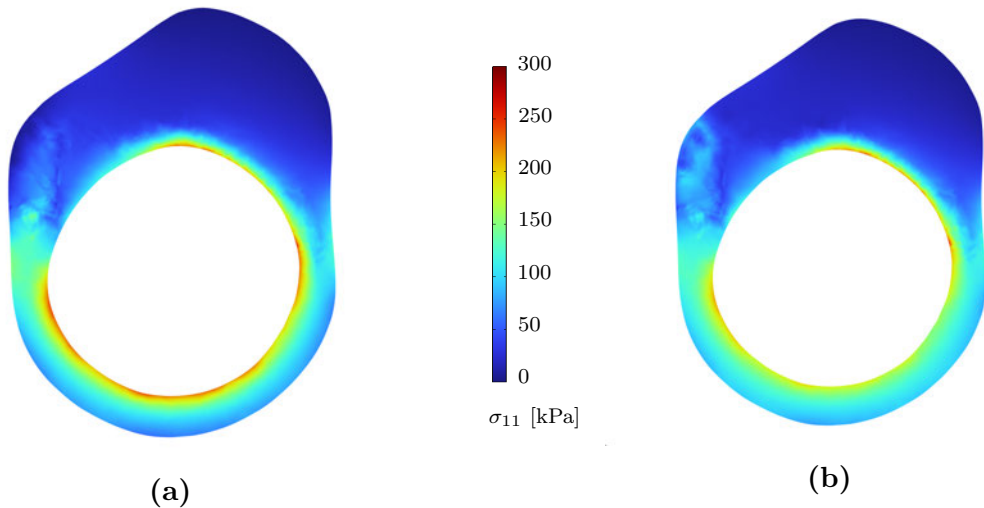


Figure 4.20: First principal stress field on the third slice of interest with a boundary condition of 180 mmHg and comparison between the standard (a) and the growth (b) analysis. The growth one shows a reduction of peak stresses and a more homogenous stress field.

In a final step, the pressure is increased up to pressure values typical of hypertension, corresponding to 180 mmHg. As shown in fig. 4.16, the model with growth confirms lower peak stress. Both standard and growth models show dangerous stress

higher than 280 kPa that could potentially lead to plaque rupture. However, the model with remodeling shows smaller areas with such elevated values, that is 2.2% of the total tissues vs 4.3%. Such peak stress reduction is evident from different section of the atherosclerotic plaque as shown in fig. 4.18 or fig. 4.20.

4.2.3 Residual strains

Another interesting simulation outcome is obtained by reducing the loading pressure to zero, to eventually observe residual strain and stress due to the growth mechanism.

By completely removing both the pressure load and the external constraints, residual volumetric strains are clearly observable, as plotted in fig. 4.21. This is related to the growth algorithm and shows how the vessel has remodeled itself under the influence of the average pressure.

The residual strain appears negative outside, up to -10%, and positive inside, up to 5%. Higher positive strains appear near the interface with the lipid-rich tissue in the plaque core and near the fibrous cap.

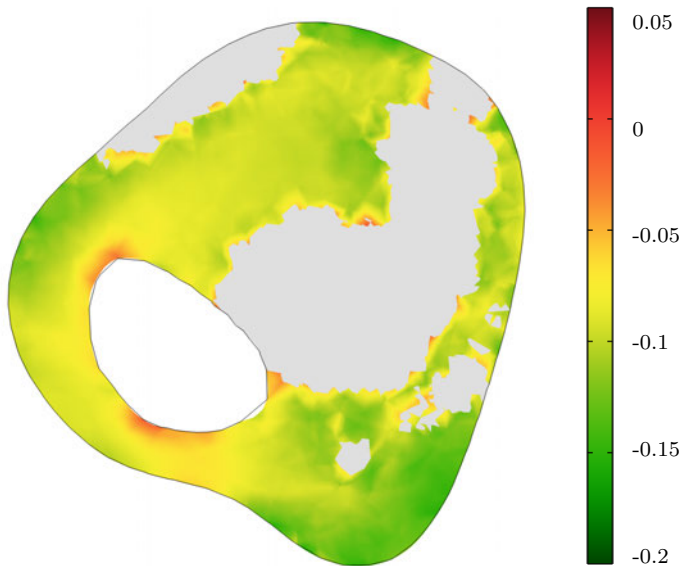


Figure 4.21: Residual strain on the slice of interest. Volumetric strains are shown for vascular tissue (MATX) and appear positive on the internal side and negative outside.

4.3 Comparison between different patients

In order to better verify the performance and significance of the developed computational tool, three additional patients have been analyzed.

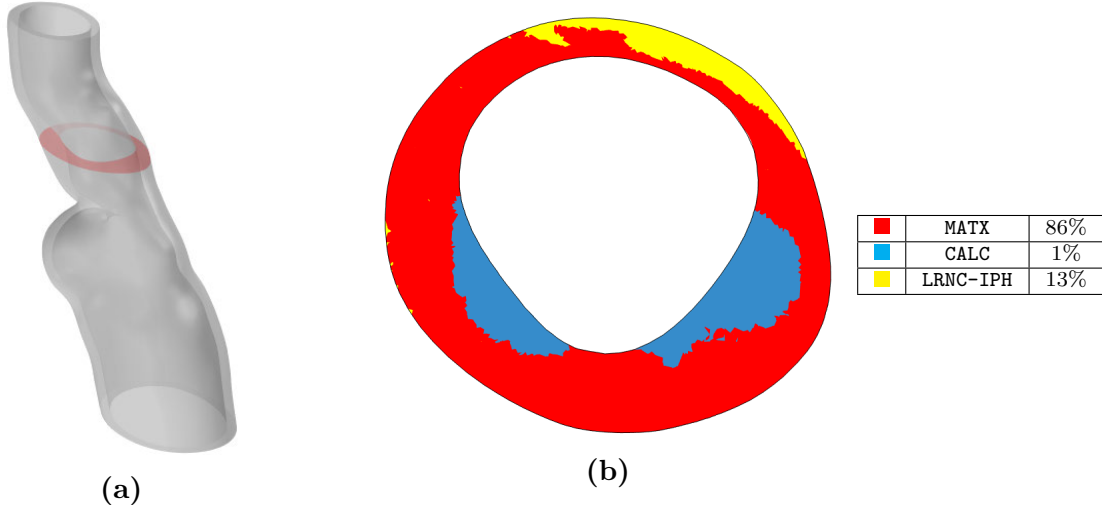


Figure 4.22: 3D reconstruction of the vessel for patient ID 779 (a); Slice of interest (b) with different materials highlighted with different colors. In the table also the percentages of the constituents are shown for the whole vessel.

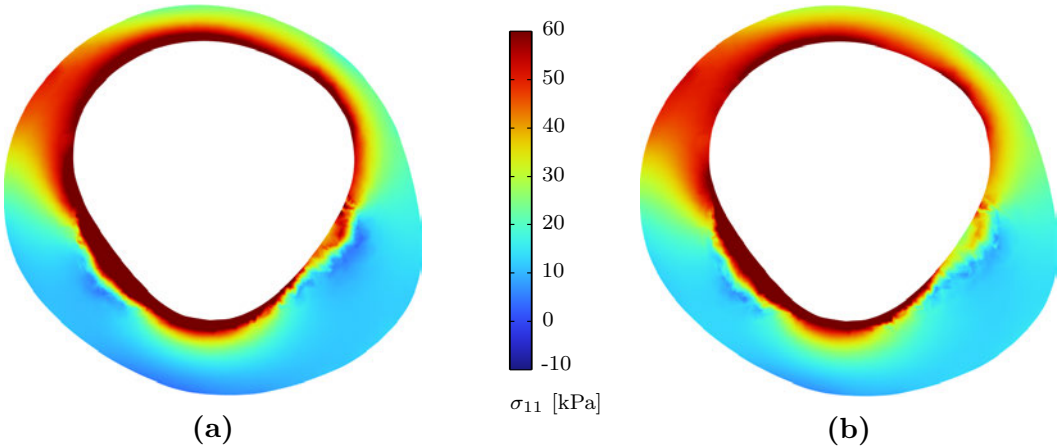


Figure 4.23: First principal stress field on the slice of interest with a boundary condition of **average blood pressure** and comparison between the standard (a) and the growth (b) analysis.

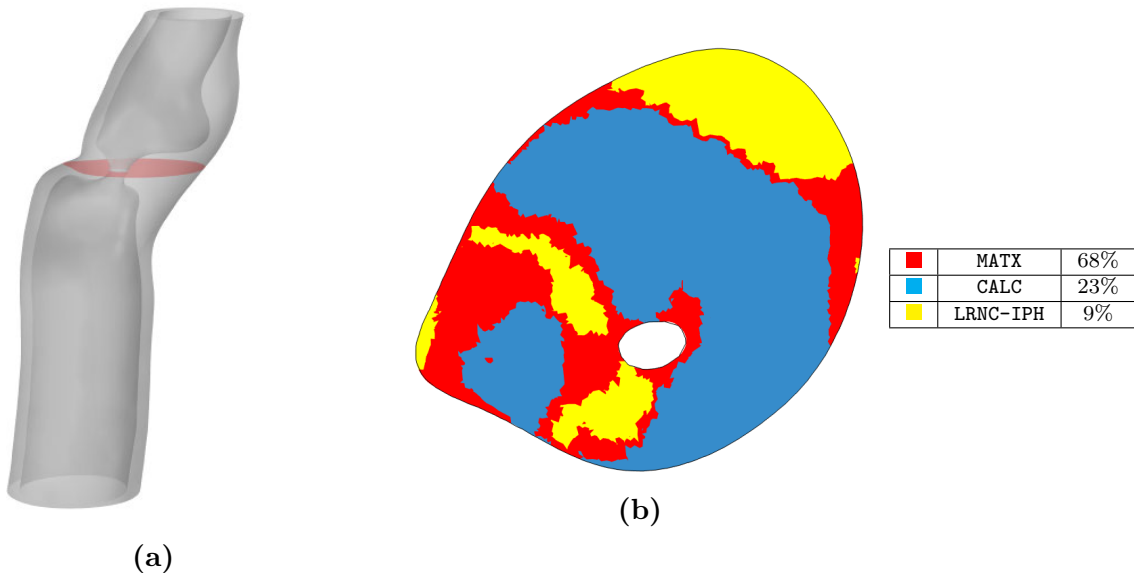


Figure 4.24: 3D reconstruction of the vessel for patient ID 753 (a); Slice of interest (b) with different materials highlighted with different colors. In the table also the percentages of the constituents are shown for the whole vessel.

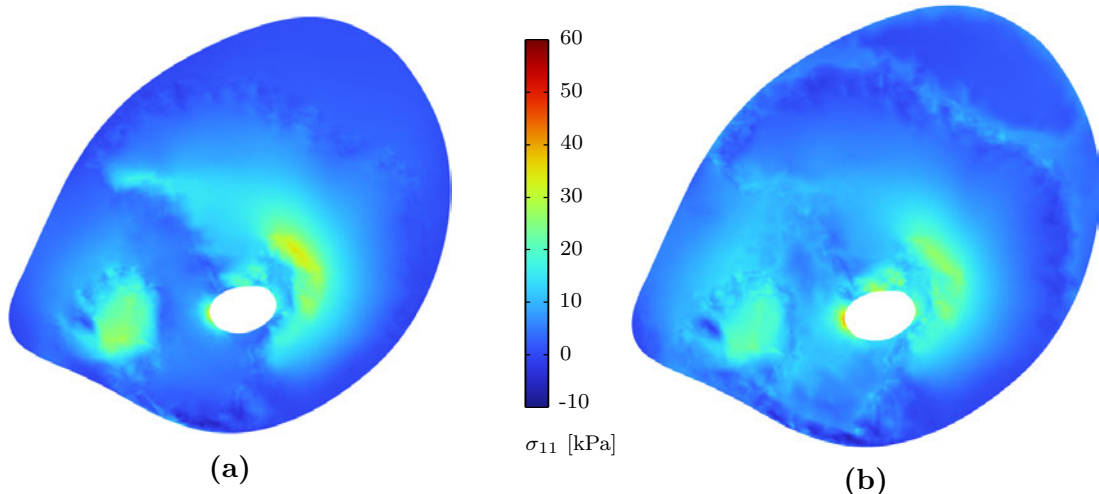


Figure 4.25: First principal stress field on the slice of interest with a boundary condition of **average blood pressure** and comparison between the standard (a) and the growth (b) analysis.

These new cases allow us to highlight different effects due to both thin and thick vessel walls. Results in figs. 4.23 and 5.3 show how tissue distribution can affect homogenization. Peak stress reduction is still present, however, due to the thin vascular

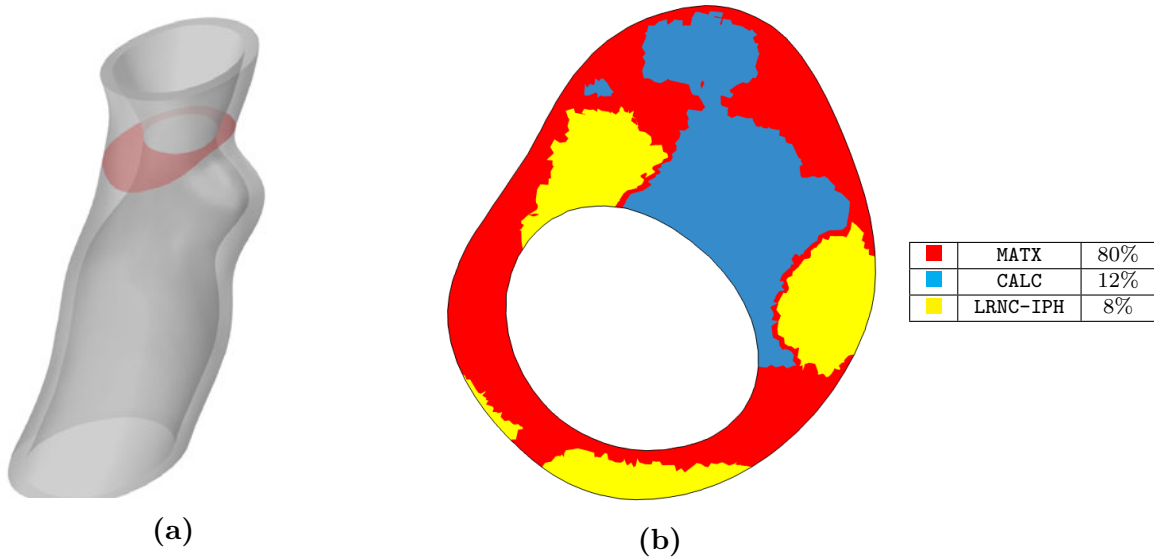


Figure 4.26: 3D reconstruction of the vessel from patient ID 710 (a); Slice of interest (b) with different materials highlighted with different colors. In the table also the percentages of the constituents are shown for the whole vessel.

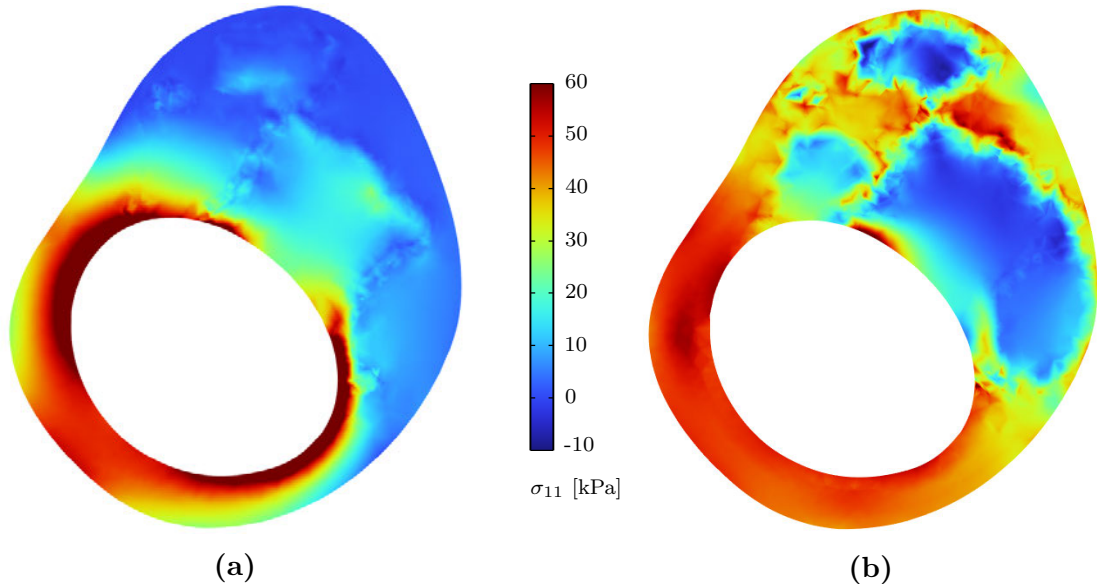


Figure 4.27: First principal stress field on the slice of interest with a boundary condition of **average blood pressure** and comparison between the standard (a) and the growth (b) analysis.

wall could be harder to homogenize. A similar effect is shown in fig. 4.20.

Extremely thick walls generally lead to lower stresses, as shown in figs. 4.25 and 5.5,

but the peak stress reduction is still present, as shown in fig. 4.18.

Comparison between fig. 5.5 and fig. 4.18 highlights how tissue distribution affects the resulting homogenized stress state leading to different growth outcomes. For instance, due to the calcification-type tissue interfaces, a high-stress area remains located right on the fibrous cap as shown in figs. 4.27b and 5.7b. This higher stress area is present both at the average pressure and at the systolic pressure highlighting how particular combination of pathological tissues and geometries could lead to a serious rupture risk.

Further results from these three cases are shown in the Appendix.

Chapter 5

Discussion and conclusion

The present thesis develops a computational tool for the stress analysis of atherosclerotic regions of patient-specific carotid structures. Simulations account for a growth and remodeling formulation that employs a multi-material description. Adopting a growth strategy based on the homogenous stress hypothesis, residual strains and stresses for vascular vessels are computed in realistic clinical scenarios. Accordingly, their impact in determining the biomechanical state of the vessel could be accounted for, increasing the accuracy of *in silico* strategies for risk evaluation and plaque rupture estimation.

Obtained results demonstrated that the use of advanced simulation techniques, based on medical imaging and refined numerical methods, are effective tools to analyze clinical scenarios in a patient-specific context and to characterize the atherosclerosis plaque biomechanical environment. Moreover, the presented cases show how taking into account residual strain leads to generally different results compared to more standard finite element analyses that neglect growth and remodeling.

The finite element results generally show reasonable negative stretches on the internal side of the vessel and positive ones on the outside. The resulting residual strains lead to a more homogenous stress state with lower peak stresses if compared to the ones obtained without considering growth. Residual strains are in the expected range. It is however important to observe that due to the high non-linearities of the

materials, small differences in strains can correspond to large differences in stresses. Therefore, uncertainties in material properties may affect this outcome.

The aforementioned analyses show how including residual strain leads to generally lower peak stresses. Remarkable is the fact that, despite the homogenization and reduction of peak stresses, numerical analyses show how areas of highest stresses remain right close to the fibrous cap. This is very interesting in order to evaluate the rupture risk since it corresponds to the typical location of plaque rupture. This outcome requires further investigations considering more refined modeling descriptions, for instance, including tissue damage and fracture models.

Considering that the algorithm works only on non-atherosclerotic vascular tissue, the results are strongly dependent on the distribution of plaque materials. While this is desired to account for patient-specific properties, it requires careful case-by-case evaluation of the results. These analyses show significant differences in the growth outcome for extremely thin or thick walls. Very thick walls are constituted by a significant amount of load-bearing material leading to generally lower stresses and a minor significance of stresses homogenization. However, a peak stress reduction is still evident.

Several models, often developed in academia, start to be enough consisted to be applied in clinical procedures. From the description of physiopathology, they could allow driving fundamental research as well as device-related studies. For atherosclerotic plaque, several studies investigate the mechanical effect of typical treatments such as stents and balloons [33, 34]. Furthermore, several medical devices start to be developed as simulative software that could help clinicians in the evaluation, treatment and follow-up of pathologies and patients.

The presented formulation could lead to a more reliable *in vivo* stress prediction with respect to standard analyses. However, further improvements could be done as regards a more detailed description of tissue growth that accounts for chemo-biological effects or a fully coupled loading-growth approach. We also based the growth homogenization and remodeling on the first principle stress without any conclusive experi-

mental evidence. In addition, the blood pressure was applied homogeneously and this could be improved by considering a fluid dynamics approach.

Furthermore, the model is based on isotropic tissue description following the Yeoh hyperelastic model. Several studies show that this is a reasonable approach in this context [59, 41, 42], however, the effects of anisotropic tissue may be considered. Finally, growth is modulated by a scale factor introduced to avoid numerical instabilities. This factor has to be calibrated for each patient-specific model, generally depending on the considered geometry, mesh quality, and tissue distribution at hand.

Clearly, every G&R theory, like the one here proposed, requires a strong cross-interaction between different disciplines in order to specify the typologies of cells and tissues that could grow and the law that describes their growth. In particular, the developed model is based on a mechanistic approach grounded on the homogeneous stress hypothesis. Lately, we observe the emergence of a completely different paradigm, where models are data-driven through artificial intelligence. Deep-learning models could be used to estimate tissue description [51] as well as to estimate behavior and tissue functionalities in order to better understand complex processes such as growth and remodeling [52]. In this context, the developed approach can serve as a tool that can support the development of more physically-sound surrogate models trained via machine learning approaches. The combination between model-based and data-based strategies could lead to a revolutionary approach in the bio-mechanical evaluation of patients, and also in the context of plaque rupture risk evaluation.

Acknowledgements

I would like to express my deepest appreciation to my thesis advisor, Prof. Michele Marino and my University. His office door was always open for providing guidance and feedback throughout this project and more. He allowed me to develop this innovative and interesting master's thesis and to carry out this research work in collaboration with the KTH Royal Institute of Technology in Stockholm.

Consequently, I am also extremely grateful to Prof. Christian Thomas Gasser who supervised my internship at KTH and the whole project. This experience has given me the opportunity to learn a lot and to work in this cutting-edge environment.

Clearly, none of this would have been possible without the support of my family and my girlfriend. They always support me and encouraged me to always do more and better. Thanks.

I am also grateful to my friends and colleagues with whom I have shared the joys and difficulties of these years.

Thanks.

References

- [1] Khaled M. Abdelrahman et al. “Coronary Computed Tomography Angiography From Clinical Uses to Emerging Technologies”. In: *Journal of the American College of Cardiology* 76.10 (Sept. 2020), pp. 1226–1243. ISSN: 07351097. DOI: 10.1016/j.jacc.2020.06.076.
- [2] George S. Abela et al. “Effect of Cholesterol Crystals on Plaques and Intima in Arteries of Patients With Acute Coronary and Cerebrovascular Syndromes”. In: *The American Journal of Cardiology* 103.7 (Apr. 2009), pp. 959–968. ISSN: 00029149. DOI: 10.1016/j.amjcard.2008.12.019.
- [3] Ali C. Akyildiz, Hilary E. Barrett, and Frank J.H. Gijsen. “Identification of Coronary Plaque Mechanical Properties from Ex Vivo Testing”. In: *Biomechanics of Coronary Atherosclerotic Plaque*. Elsevier, 2021, pp. 411–432. ISBN: 978-0-12-817195-0. DOI: 10.1016/B978-0-12-817195-0.00018-4.
- [4] Ali C. Akyildiz, Lambert Speelman, and Frank J.H. Gijsen. “Mechanical Properties of Human Atherosclerotic Intima Tissue”. In: *Journal of Biomechanics* 47.4 (Mar. 2014), pp. 773–783. ISSN: 00219290. DOI: 10.1016/j.jbiomech.2014.01.019.
- [5] V. Alastruñ et al. “Numerical Framework for Patient-Specific Computational Modelling of Vascular Tissue”. In: *International Journal for Numerical Methods in Biomedical Engineering* 26.1 (Jan. 2010), pp. 35–51. ISSN: 20407939, 20407947. DOI: 10.1002/cnm.1234.
- [6] L Arroyo. “Mechanisms of Plaque Rupture Mechanical and Biologic Interactions”. In: *Cardiovascular Research* 41.2 (Feb. 1, 1999), pp. 369–375. ISSN: 00086363. DOI: 10.1016/S0008-6363(98)00308-3.
- [7] Ruxandra Barbulescu and Daniel Ioan. “Multi-Scale and Reduced Modelling of Biological Systems”. In: (May 2015), pp. 597–602. DOI: 10.1109/ATEE.2015.7133876.
- [8] Henry J.M. Barnett et al. “Benefit of Carotid Endarterectomy in Patients with Symptomatic Moderate or Severe Stenosis”. In: *New England Journal of Medicine* 339.20 (Nov. 12, 1998), pp. 1415–1425. ISSN: 0028-4793, 1533-4406. DOI: 10.1056/NEJM199811123392002.
- [9] Renate W. Boekhoven et al. “Towards Mechanical Characterization of Intact Endarterectomy Samples of Carotid Arteries during Inflation Using Echo-CT”. In: *Journal of Biomechanics* 47.4 (Mar. 2014), pp. 805–814. ISSN: 00219290. DOI: 10.1016/j.jbiomech.2014.01.016.
- [10] F. A. Braeu et al. “Homogenized Constrained Mixture Models for Anisotropic Volumetric Growth and Remodeling”. In: *Biomechanics and Modeling in Mechanobiology* 16.3 (June 2017), pp. 889–906. ISSN: 1617-7959, 1617-7940. DOI: 10.1007/s10237-016-0859-1.
- [11] Andrew J Buckler. “Patient-Specific Biomechanical Analysis of Atherosclerotic Plaques Enabled by Histologically Validated Tissue Characterization from Computed Tomography Angiography: A Case Study”. In: *Journal of the Mechanical Behavior of Biomedical Materials* (2022), p. 7.

-
- [12] Vincent Calvez et al. “Mathematical Modelling of the Atherosclerotic Plaque Formation”. In: *ESAIM: Proceedings* 28 (2009). Ed. by M. Ismail, B. Maury, and J.-F. Gerbeau, pp. 1–12. ISSN: 1270-900X. DOI: 10.1051/proc/2009036.
- [13] “Carotid Artery Diameter in Men and Women and the Relation to Body and Neck Size”. In: 37 (). ISSN: 0039-2499, 1524-4628. DOI: 10.1161/01.STR.0000206440.48756.f7. URL: <https://www.ahajournals.org/doi/10.1161/01.STR.0000206440.48756.f7>.
- [14] Sandra Carr et al. “Atherosclerotic Plaque Rupture in Symptomatic Carotid Artery Stenosis”. In: *Journal of Vascular Surgery* 23.5 (May 1996), pp. 755–766. ISSN: 07415214. DOI: 10.1016/S0741-5214(96)70237-9.
- [15] Chen-Ket Chai et al. “Compressive Mechanical Properties of Atherosclerotic Plaques - Indentation Test to Characterise the Local Anisotropic Behaviour”. In: *Journal of Biomechanics* 47.4 (Mar. 2014), pp. 784–792. ISSN: 00219290. DOI: 10.1016/j.jbiomech.2014.01.018.
- [16] Chen-Ket Chai et al. “Local anisotropic mechanical properties of human carotid atherosclerotic plaques - Characterisation by micro-indentation and inverse finite element analysis”. In: *Journal of the Mechanical Behavior of Biomedical Materials* 43 (2015), pp. 59–68. ISSN: 1751-6161. DOI: <https://doi.org/10.1016/j.jmbbm.2014.12.004>.
- [17] Bo Cheng et al. “Cellular Mechanosensing of the Biophysical Microenvironment: A Review of Mathematical Models of Biophysical Regulation of Cell Responses”. In: *Physics of Life Reviews* 22–23 (Dec. 2017), pp. 88–119. DOI: 10.1016/j.plrev.2017.06.016.
- [18] G C Cheng et al. “Distribution of Circumferential Stress in Ruptured and Stable Atherosclerotic Lesions. A Structural Analysis with Histopathological Correlation.” In: *Circulation* 87.4 (Apr. 1993), pp. 1179–1187. ISSN: 0009-7322, 1524-4539. DOI: 10.1161/01.CIR.87.4.1179.
- [19] C. J. Chuong and Y. C. Fung. “On Residual Stresses in Arteries”. In: *Journal of Biomechanical Engineering* 108.2 (May 1, 1986), pp. 189–192. ISSN: 0148-0731, 1528-8951. DOI: 10.1115/1.3138600.
- [20] Myriam Cilla, Estefania Pena, and Miguel A. Martinez. “Mathematical Modelling of Atheroma Plaque Formation and Development in Coronary Arteries”. In: *Journal of The Royal Society Interface* 11.90 (Jan. 6, 2014), p. 20130866. ISSN: 1742-5689, 1742-5662. DOI: 10.1098/rsif.2013.0866.
- [21] North American Symptomatic Carotid Endarterectomy Trial Collaborators. “Beneficial Effect of Carotid Endarterectomy in Symptomatic Patients with High-Grade Carotid Stenosis”. In: *New England Journal of Medicine* 325.7 (Aug. 15, 1991), pp. 445–453. ISSN: 0028-4793, 1533-4406. DOI: 10.1056/NEJM199108153250701.
- [22] Catherine Bjerre Collin et al. “Computational Models for Clinical Applications in Personalized Medicine-Guidelines and Recommendations for Data Integration and Model Validation”. In: *Journal of Personalized Medicine* 12.2 (2022). DOI: 10.3390/jpm12020166. (Visited on 04/05/2023).
- [23] “Computational modeling of arterial wall growth: Attempts towards patient-specific simulations based on computer tomography”. In: 6 (). ISSN: 1617-7959, 1617-7940. DOI: 10.1007/s10237-006-0062-x. URL: <http://link.springer.com/10.1007/s10237-006-0062-x>.
- [24] Comsol. *General-purpose simulation software based on advanced numerical methods*. 2022. URL: <https://www.comsol.com>.
- [25] Comsol. *Incompressible hyperelastic materials and the locking problem*. 2022. URL: https://doc.comsol.com/5.5/doc/com.comsol.help.sme/sme_ug_theory.06.28.html#3782672.

-
- [26] Anna Corti et al. “A Fully Coupled Computational Fluid Dynamics - Agent-Based Model of Atherosclerotic Plaque Development: Multiscale Modeling Framework and Parameter Sensitivity Analysis”. In: *Computers in Biology and Medicine* 118 (Mar. 2020), p. 103623. ISSN: 00104825. DOI: 10.1016/j.combiomed.2020.103623.
- [27] C. J. Cyron and J. D. Humphrey. “Growth and Remodeling of Load-Bearing Biological Soft Tissues”. In: *Meccanica* 52.3 (Feb. 2017), pp. 645–664. ISSN: 0025-6455, 1572-9648. DOI: 10.1007/s11012-016-0472-5.
- [28] A. Delfino et al. “Residual Strain Effects on the Stress Field in a Thick Wall Finite Element Model of the Human Carotid Bifurcation”. In: *Journal of Biomechanics* 30.8 (Aug. 1997), pp. 777–786. ISSN: 00219290. DOI: 10.1016/S0021-9290(97)00025-0.
- [29] Yepeng Du et al. “A Study of the Fluid-Structure Interaction of the Plaque Circumferential Distribution in the Left Coronary Artery”. en. In: *Applied Sciences* 12.12 (June 2022). ISSN: 2076-3417. DOI: 10.3390/app12126200.
- [30] Jonas F. Eichinger et al. “Mechanical Homeostasis in Tissue Equivalents: A Review”. In: *Biomechanics and Modeling in Mechanobiology* 20.3 (June 2021), pp. 833–850. ISSN: 1617-7959, 1617-7940. DOI: 10.1007/s10237-021-01433-9.
- [31] ElucidVivo. *Elucid - See Beyond the Lumen*. 2022. URL: <https://elucid.com>.
- [32] Gunnar Engstrom et al. “Geographic Distribution of Stroke Incidence Within an Urban Population: Relations to Socioeconomic Circumstances and Prevalence of Cardiovascular Risk Factors”. In: *Stroke* 32.5 (May 2001), pp. 1098–1103. ISSN: 0039-2499, 1524-4628. DOI: 10.1161/01.STR.32.5.1098.
- [33] Javier Escuer et al. “Mathematical Modelling of the Restenosis Process after Stent Implantation”. In: *Journal of The Royal Society Interface* 16.157 (Aug. 2019), p. 20190313. ISSN: 1742-5689, 1742-5662. DOI: 10.1098/rsif.2019.0313.
- [34] Javier Escuer et al. “Mathematical Modelling of Endovascular Drug Delivery: Balloons versus Stents”. In: *International Journal of Pharmaceutics* 620 (May 2022), p. 121742. ISSN: 03785173. DOI: 10.1016/j.ijpharm.2022.121742.
- [35] GÃ©rard Finet, Jacques Ohayon, and Gilles Rioufol. “Biomechanical Interaction between Cap Thickness, Lipid Core Composition and Blood Pressure in Vulnerable Coronary Plaque: Impact on Stability or Instability.” in: *Coronary Artery Disease* 15.1 (Feb. 2004), pp. 13–20. ISSN: 0954-6928. DOI: 10.1097/00019501-200402000-00003.
- [36] Y. C. Fung. *Biomechanics*. New York, NY: Springer New York, 1990. DOI: 10.1007/978-1-4419-6856-2.
- [37] Y. C. Fung. “What Are the Residual Stresses Doing in Our Blood Vessels?” In: *Annals of Biomedical Engineering* 19.3 (May 1991), pp. 237–249. ISSN: 0090-6964, 1573-9686. DOI: 10.1007/BF02584301.
- [38] Y C Fung and S Q Liu. “Change of Residual Strains in Arteries Due to Hypertrophy Caused by Aortic Constriction.” In: *Circulation Research* 65.5 (Nov. 1989), pp. 1340–1349. ISSN: 0009-7330, 1524-4571. DOI: 10.1161/01.RES.65.5.1340.
- [39] T. Christian Gasser. *Vascular Biomechanics: Concepts, Models, and Applications*. 1st ed. Sweden: Springer, Jan. 1, 2021. 622 pp. ISBN: 978-3-030-70966-2. DOI: 10.1007/978-3-030-70966-2.
- [40] Milad Ghasemi, David R. Nolan, and CaitrÃona Lally. “Assessment of Mechanical Indicators of Carotid Plaque Vulnerability: Geometrical Curvature Metric, Plaque Stresses and Damage in Tissue Fibres”. In: *Journal of the Mechanical Behavior of Biomedical Materials* 103 (Mar. 2020), p. 103573. ISSN: 17516161. DOI: 10.1016/j.jmbbm.2019.103573.

-
- [41] Meike Gierig, Peter Wriggers, and Michele Marino. “Computational model of damage-induced growth in soft biological tissues considering the mechanobiology of healing”. en. In: *Biomechanics and Modeling in Mechanobiology* 20.4 (). DOI: 10.1007/s10237-021-01445-5. (Visited on 04/06/2023).
- [42] Meike Gierig, Peter Wriggers, and Michele Marino. “Arterial tissues and their inflammatory response to collagen damage: A continuum in silico model coupling nonlinear mechanics, molecular pathways, and cell behavior”. en. In: *Computers in Biology and Medicine* 158 (May 2023). DOI: 10.1016/j.combiomed.2023.106811. (Visited on 04/06/2023).
- [43] Frank J.H. Gijsen and Francesco Migliavacca. “Plaque Mechanics”. In: *Journal of Biomechanics* 47.4 (Mar. 2014), pp. 763–764. ISSN: 00219290. DOI: 10.1016/j.jbiomech.2014.01.031.
- [44] Vincent M. Heiland et al. “Identification of Carotid Plaque Tissue Properties Using an Experimental - Numerical Approach”. In: *Journal of the Mechanical Behavior of Biomedical Materials* 27 (Nov. 2013), pp. 226–238. ISSN: 17516161. DOI: 10.1016/j.jmbbm.2013.05.001.
- [45] G Himpel et al. “Computational Modelling of Isotropic Multiplicative Growth”. en. In: (2005).
- [46] Gerhard A. Holzapfel and R. W. Ogden, eds. *Mechanics of biological tissue*. en. Meeting Name: IUTAM Symposium on Mechanics of Biological Tissue. Berlin ; New York: Springer, 2006. ISBN: 978-3-540-25194-1.
- [47] Gerhard A. Holzapfel et al. “Layer-Specific 3D Residual Deformations of Human Aortas with Non-Atherosclerotic Intimal Thickening”. In: *Annals of Biomedical Engineering* 35.4 (Mar. 16, 2007), pp. 530–545. ISSN: 0090-6964, 1573-9686. DOI: 10.1007/s10439-006-9252-z.
- [48] iso2mesh. *A 3D surface and volumetric mesh generator for MATLAB/Octave*. 2022. URL: <http://iso2mesh.sf.net/cgi-bin/index.cgi>.
- [49] Frank D. Kolodgie et al. “Intraplaque Hemorrhage and Progression of Coronary Atheroma”. In: *New England Journal of Medicine* 349.24 (Dec. 11, 2003), pp. 2316–2325. ISSN: 0028-4793, 1533-4406. DOI: 10.1056/NEJMoa035655.
- [50] Michael G. Lawlor et al. “Experimental determination of circumferential properties of fresh carotid artery plaques”. In: *Journal of Biomechanics* 44.9 (2011), pp. 1709–1715. ISSN: 0021-9290. DOI: <https://doi.org/10.1016/j.jbiomech.2011.03.033>.
- [51] Kevin Linka et al. “Constitutive Artificial Neural Networks: A Fast and General Approach to Predictive Data-Driven Constitutive Modeling by Deep Learning”. In: *Journal of Computational Physics* 429 (Mar. 2021), p. 110010. ISSN: 00219991. DOI: 10.1016/j.jcp.2020.110010.
- [52] Kevin Linka et al. “Predicting and Understanding Arterial Elasticity from Key Microstructural Features by Bidirectional Deep Learning”. In: *Acta Biomaterialia* 147 (July 2022), pp. 63–72. ISSN: 17427061. DOI: 10.1016/j.actbio.2022.05.039.
- [53] Ondrej Lisicky et al. “Constitutive Models and Failure Properties of Fibrous Tissues of Carotid Artery Atheroma Based on Their Uniaxial Testing”. In: *Journal of Biomechanics* 129 (Dec. 2021), p. 110861. ISSN: 00219290. DOI: 10.1016/j.jbiomech.2021.110861.
- [54] Ian Loftus. *Mechanisms of Plaque Rupture*. eng. Ed. by Robert Fitridge and Matthew Thompson. Adelaide (AU): University of Adelaide Press, 2011. ISBN: 978-0-9871718-2-5. (Visited on 04/05/2023).
- [55] H M Loree et al. “Effects of Fibrous Cap Thickness on Peak Circumferential Stress in Model Atherosclerotic Vessels.” In: *Circulation Research* 71.4 (Oct. 1992), pp. 850–858. ISSN: 0009-7330, 1524-4571. DOI: 10.1161/01.RES.71.4.850.

-
- [56] Jinqiu Lu, Wanying Duan, and Aike Qiao. “Finite Element Analysis of Mechanics of Neovessels with Intraplaque Hemorrhage in Carotid Atherosclerosis”. In: *BioMedical Engineering OnLine* 14.S1 (Jan. 2015), S3. ISSN: 1475-925X. DOI: 10.1186/1475-925X-14-S1-S3.
- [57] John Lynch et al. “Socioeconomic Status and Carotid Atherosclerosis”. In: *Circulation* 92.7 (Oct. 1995), pp. 1786–1792. ISSN: 0009-7322, 1524-4539. DOI: 10.1161/01.CIR.92.7.1786.
- [58] Natalia Maldonado et al. “A Mechanistic Analysis of the Role of Microcalcifications in Atherosclerotic Plaque Stability: Potential Implications for Plaque Rupture”. In: *American Journal of Physiology-Heart and Circulatory Physiology* 303.5 (Sept. 1, 2012), H619–H628. ISSN: 0363-6135, 1522-1539. DOI: 10.1152/ajpheart.00036.2012.
- [59] Michele Marino et al. “A chemo-mechano-biological formulation for the effects of biochemical alterations on arterial mechanics: the role of molecular transport and multiscale tissue remodelling”. en. In: *Journal of The Royal Society Interface* 14.136 (Nov. 2017). ISSN: 1742-5689, 1742-5662. DOI: 10.1098/rsif.2017.0615. URL: <https://royalsocietypublishing.org/doi/10.1098/rsif.2017.0615> (visited on 04/06/2023).
- [60] Jean-Louis Martiel et al. “Chapter 19 - Importance of residual stress and basal tone in healthy and pathological human coronary arteries”. In: *Biomechanics of Coronary Atherosclerotic Plaque*. Ed. by Jacques Ohayon, Gerard Finet, and Roderic Ivan Pettigrew. Vol. 4. Biomechanics of Living Organs. Academic Press, 2021, pp. 433–461. DOI: <https://doi.org/10.1016/B978-0-12-817195-0.00019-6>.
- [61] D Martin et al. “Analysis of Haemodynamic Factors Involved in Carotid Atherosclerosis Using Computational Fluid Dynamics”. In: *The British Journal of Radiology* 82 (special_issue_1 Jan. 2009), S33–S38. ISSN: 0007-1285, 1748-880X. DOI: 10.1259/bjr/59367266.
- [62] Matlab. *MathWorks*. 2022. URL: <http://matlab.mathworks.com>.
- [63] Andreas Menzel and Ellen Kuhl. “Frontiers in Growth and Remodeling”. In: *Mechanics Research Communications* 42 (June 2012), pp. 1–14. ISSN: 00936413. DOI: 10.1016/j.mechrescom.2012.02.007.
- [64] Emmanuel Messas et al. “Management of Carotid Stenosis for Primary and Secondary Prevention of Stroke: State-of-the-Art 2020: A Critical Review”. In: *European Heart Journal Supplements* 22 (Supplement_M Dec. 5, 2020), pp. M35–M42. ISSN: 1520-765X, 1554-2815. DOI: 10.1093/eurheartj/suaa162.
- [65] J.-B. Michel et al. “Intraplaque Haemorrhages as the Trigger of Plaque Vulnerability”. In: *European Heart Journal* 32.16 (Aug. 2, 2011), pp. 1977–1985. ISSN: 0195-668X, 1522-9645. DOI: 10.1093/eurheartj/ehr054.
- [66] Majid M Mughal et al. “Symptomatic and Asymptomatic Carotid Artery Plaque”. In: *Expert Review of Cardiovascular Therapy* 9.10 (Oct. 2011), pp. 1315–1330. ISSN: 1477-9072, 1744-8344. DOI: 10.1586/erc.11.120.
- [67] Jacques Ohayon, Gerard Finet, and Roderic Pettigrew, eds. *Biomechanics of Coronary Atherosclerotic Plaque: From Model to Patient*. Biomechanics of Living Organs. London: Academic Press, 2020. 675 pp. ISBN: 978-0-12-817195-0.
- [68] Jacques Ohayon et al. “Influence of Residual Stress/Strain on the Biomechanical Stability of Vulnerable Coronary Plaques: Potential Impact for Evaluating the Risk of Plaque Rupture”. In: *American Journal of Physiology-Heart and Circulatory Physiology* 293.3 (Sept. 2007), H1987–H1996. ISSN: 0363-6135, 1522-1539. DOI: 10.1152/ajpheart.00018.2007.
- [69] D H O’Leary et al. “Distribution and Correlates of Sonographically Detected Carotid Artery Disease in the Cardiovascular Health Study. The CHS Collaborative Research Group.” In: *Stroke* 23.12 (Dec. 1992), pp. 1752–1760. DOI: 10.1161/01.STR.23.12.1752.

-
- [70] Hideki Ota et al. “Hemorrhage and Large Lipid-Rich Necrotic Cores Are Independently Associated With Thin or Ruptured Fibrous Caps: An In Vivo 3T MRI Study”. In: *Arteriosclerosis, Thrombosis, and Vascular Biology* 29.10 (Oct. 2009), pp. 1696–1701. ISSN: 1079-5642, 1524-4636. DOI: 10.1161/ATVBAHA.109.192179.
- [71] Marie OuarnÃ©c, Andreia Pena, and ClÃ¡udio Areias Franco. “From Remodeling to Quiescence: The Transformation of the Vascular Network”. In: *Cells & Development* 168 (Dec. 2021), p. 203735. ISSN: 26672901. DOI: 10.1016/j.cdev.2021.203735.
- [72] E. Pena et al. “On the Numerical Treatment of Initial Strains in Biological Soft Tissues”. In: *International Journal for Numerical Methods in Engineering* 68.8 (Nov. 19, 2006), pp. 836–860. ISSN: 00295981, 10970207. DOI: 10.1002/nme.1726.
- [73] George W. Petty et al. “Ischemic Stroke Subtypes: A Population-Based Study of Incidence and Risk Factors”. In: *Stroke* 30.12 (Dec. 1999), pp. 2513–2516. ISSN: 0039-2499, 1524-4628. DOI: 10.1161/01.STR.30.12.2513.
- [74] Gineesh M. Pillai, J. S. Jayakumar, and R. Ajith Kumar. “Fluid-Structure Interaction Analysis in an Atherosclerosis Carotid Artery”. In: (2022). Ed. by Pinakeswar Mahanta et al. DOI: 10.1007/978-981-16-3497-0_2.
- [75] G[acute]eacut[e]rard E. Plante. “Vascular Response to Stress in Health and Disease”. In: *Metabolism* 51.6 (June 2002), pp. 25–30. ISSN: 00260495. DOI: 10.1053/meta.2002.33187.
- [76] Stanislav Polzer et al. “A Numerical Implementation to Predict Residual Strains from the Homogeneous Stress Hypothesis with Application to Abdominal Aortic Aneurysms”. In: *Annals of Biomedical Engineering* 41.7 (July 2013), pp. 1516–1527. ISSN: 0090-6964, 1573-9686. DOI: 10.1007/s10439-013-0749-y.
- [77] A. Rachev, N. Stergiopoulos, and J.-J. Meister. “A Model for Geometric and Mechanical Adaptation of Arteries to Sustained Hypertension”. In: *Journal of Biomechanical Engineering* 120.1 (Feb. 1, 1998), pp. 9–17. ISSN: 0148-0731, 1528-8951. DOI: 10.1115/1.2834313.
- [78] Edward K. Rodriguez, Anne Hoger, and Andrew D. McCulloch. “Stress-Dependent Finite Growth in Soft Elastic Tissues”. In: *Journal of Biomechanics* 27.4 (Apr. 1994), pp. 455–467. ISSN: 00219290. DOI: 10.1016/0021-9290(94)90021-3.
- [79] Giuseppe Sangiorgi et al. *Carotid Atherosclerotic Disease*. en. CRC Press, 2008. ISBN: 978-0-429-16368-5.
- [80] Giuseppe Sangiorgi et al. *Carotid Atherosclerotic Disease*. CRC Press, 2008. ISBN: 978-0-429-16368-5.
- [81] Taisiya Sigaeva et al. “Anisotropic Residual Stresses in Arteries”. In: *Journal of The Royal Society Interface* 16.151 (Feb. 2019), p. 20190029. ISSN: 1742-5689, 1742-5662. DOI: 10.1098/rsif.2019.0029.
- [82] Gerhard Sommer et al., eds. *Solid (Bio)Mechanics: Challenges of the Next Decade*. Vol. 24. Studies in Mechanobiology, Tissue Engineering and Biomaterials. Cham: Springer International Publishing, 2022. ISBN: 978-3-030-92338-9 978-3-030-92339-6. DOI: 10.1007/978-3-030-92339-6.
- [83] Susan Standring, ed. *Gray’s anatomy E-book: The anatomical basis of clinical practice*. 42nd ed. Elsevier, 2021.
- [84] Mariana Suarez-Bagnasco and Roberto Suarez-Antola. “Contributions to the study of the possible physiological and pathophysiological consequences of the nonuniform distribution of the formed elements of blood. Part two: expanded discussion”. en. In: (2020). DOI: 10.13140/RG.2.2.24936.90887.

-
- [85] Larry A. Taber. “Biomechanics of Growth, Remodeling, and Morphogenesis”. In: *Applied Mechanics Reviews* 48.8 (Aug. 1, 1995), pp. 487–545. ISSN: 0003-6900, 2379-0407. DOI: 10.1115/1.3005109.
- [86] Larry A. Taber and Daniel W. Eggers. “Theoretical Study of Stress-Modulated Growth in the Aorta”. In: *Journal of Theoretical Biology* 180.4 (June 1996), pp. 343–357. ISSN: 00225193. DOI: 10.1006/jtbi.1996.0107.
- [87] Keiichi Takamizawa and Kozaburo Hayashi. “Strain Energy Density Function and Uniform Strain Hypothesis for Arterial Mechanics”. In: *Journal of Biomechanics* 20.1 (Jan. 1987), pp. 7–17. ISSN: 00219290. DOI: 10.1016/0021-9290(87)90262-4.
- [88] Dalin Tang et al. “Local Maximal Stress Hypothesis and Computational Plaque Vulnerability Index for Atherosclerotic Plaque Assessment”. In: *Annals of Biomedical Engineering* 33.12 (Dec. 2005), pp. 1789–1801. ISSN: 0090-6964, 1573-9686. DOI: 10.1007/s10439-005-8267-1.
- [89] Zhongzhao Teng et al. “A Uni-Extension Study on the Ultimate Material Strength and Extreme Extensibility of Atherosclerotic Tissue in Human Carotid Plaques”. In: *Journal of Biomechanics* 48.14 (Nov. 2015), pp. 3859–3867. ISSN: 00219290. DOI: 10.1016/j.jbiomech.2015.09.037.
- [90] “There is urgent need to treat atherosclerotic cardiovascular disease risk earlier, more intensively, and with greater precision: A review of current practice and recommendations for improved effectiveness”. In: 12 (). ISSN: 26666677. DOI: 10.1016/j.ajpc.2022.100371. URL: <https://linkinghub.elsevier.com/retrieve/pii/S2666667722000551>.
- [91] Adam Timmis et al. “European Society of Cardiology: Cardiovascular Disease Statistics 2019”. In: *European Heart Journal* 41.1 (Jan. 1, 2020), pp. 12–85. ISSN: 0195-668X, 1522-9645. DOI: 10.1093/eurheartj/ehz859.
- [92] Ramesh N. Vaishnav and Jafar Vossoughi. “Residual Stress and Strain in Aortic Segments”. In: *Journal of Biomechanics* 20.3 (Jan. 1987), pp. 235–239. ISSN: 00219290. DOI: 10.1016/0021-9290(87)90290-9.
- [93] J. Scott VanEpps and David A. Vorp. “Mechanopathobiology of Atherogenesis: A Review”. In: *Journal of Surgical Research* 142.1 (Sept. 2007), pp. 202–217. ISSN: 00224804. DOI: 10.1016/j.jss.2006.11.001.
- [94] Kaushik P. Venkatesh, Marium M. Raza, and Joseph C. Kvedar. “Health digital twins as tools for precision medicine: Considerations for computation, implementation, and regulation”. en. In: *npj Digital Medicine* 5.1 (2022). ISSN: 2398-6352. DOI: 10.1038/s41746-022-00694-7. (Visited on 04/05/2023).
- [95] Jessica E. Wagenseil and Robert P. Mecham. “Vascular Extracellular Matrix and Arterial Mechanics”. In: *Physiological Reviews* 89.3 (July 2009), pp. 957–989. ISSN: 0031-9333, 1522-1210. DOI: 10.1152/physrev.00041.2008.
- [96] M.T. Walsh et al. “Uniaxial Tensile Testing Approaches for Characterisation of Atherosclerotic Plaques”. In: *Journal of Biomechanics* 47.4 (Mar. 2014), pp. 793–804. ISSN: 00219290. DOI: 10.1016/j.jbiomech.2014.01.017.
- [97] Chong Wang, Xiaomei Guo, and Ghassan S. Kassab. “A New Observation on the Stress Distribution in the Coronary Artery Wall”. In: *Journal of Biomechanical Engineering* 131.11 (Nov. 1, 2009), p. 111011. ISSN: 0148-0731, 1528-8951. DOI: 10.1115/1.4000106.
- [98] Liang Wang et al. “Image-Based Finite Element Modeling Approach for Characterizing In Vivo Mechanical Properties of Human Arteries”. In: *Journal of Functional Biomaterials* 13.3 (Sept. 11, 2022), p. 147. ISSN: 2079-4983. DOI: 10.3390/jfb13030147.

-
- [99] Carina Wendorff et al. “Impact of Sex and Age on Carotid Plaque Instability in Asymptomatic Patients-Results from the Munich Vascular Biobank”. In: *Vasa* 45.5 (Sept. 2016), pp. 411–416. ISSN: 0301-1526, 1664-2872. DOI: 10.1024/0301-1526/a000557.
- [100] World Health Organization (WHO). *Cardiovascular Diseases (CVDs)*. 2021. URL: [https://www.who.int/news-room/fact-sheets/detail/cardiovascular-diseases-\(cvds\)](https://www.who.int/news-room/fact-sheets/detail/cardiovascular-diseases-(cvds)).
- [101] S. D. Williamson et al. “On the Sensitivity of Wall Stresses in Diseased Arteries to Variable Material Properties”. In: *Journal of Biomechanical Engineering* 125.1 (Feb. 1, 2003), pp. 147–155. ISSN: 0148-0731, 1528-8951. DOI: 10.1115/1.1537736.
- [102] Peter W.F. Wilson et al. “Cumulative Effects of High Cholesterol Levels, High Blood Pressure, and Cigarette Smoking on Carotid Stenosis”. In: *New England Journal of Medicine* 337.8 (Aug. 21, 1997), pp. 516–522. ISSN: 0028-4793, 1533-4406. DOI: 10.1056/NEJM199708213370802.
- [103] R. J. Wityk et al. “Race and Sex Differences in the Distribution of Cerebral Atherosclerosis”. In: *Stroke* 27.11 (Nov. 1996), pp. 1974–1980. ISSN: 0039-2499, 1524-4628. DOI: 10.1161/01.STR.27.11.1974.
- [104] Harvey Wolinsky and Seymour Glagov. “A Lamellar Unit of Aortic Medial Structure and Function in Mammals”. In: *Circulation Research* 20.1 (Jan. 1967), pp. 99–111. ISSN: 0009-7330, 1524-4571. DOI: 10.1161/01.RES.20.1.99.
- [105] Oon Hock Yeoh. “Some Forms of the Strain Energy Function for Rubber”. In: *Rubber Chemistry and Technology* 66 (1993), pp. 754–771.

Appendix A

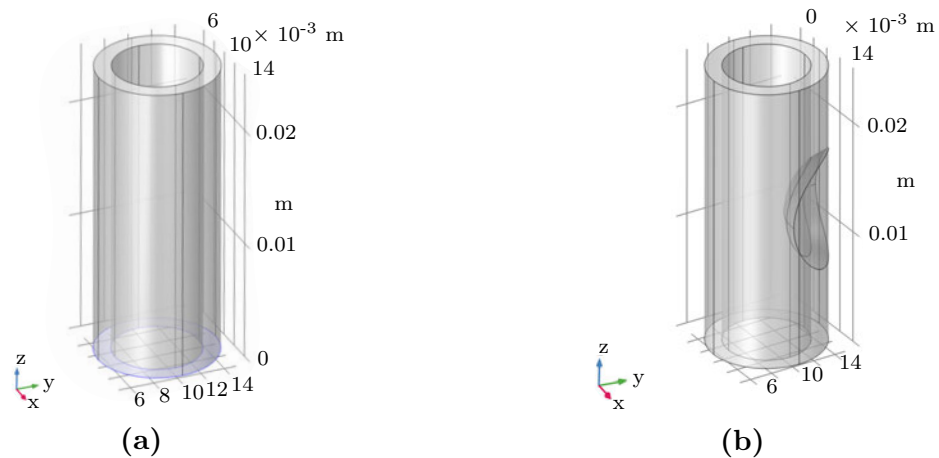


Figure 5.1: The geometry of the inflated cylinder: simple (a) and with the inclusion (b). The curve surface is splitted into four regions (both for the external and the internal ones) from Comsol as you can see from the vertical lines.

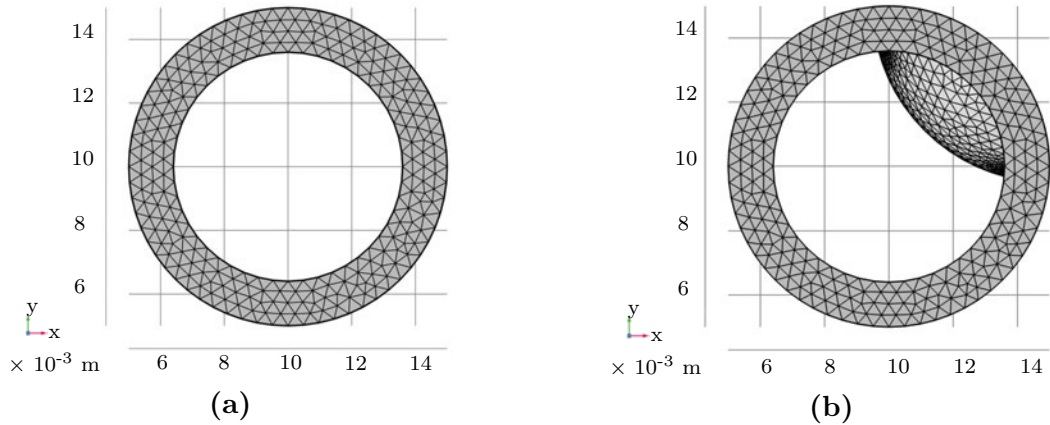


Figure 5.2: Average mesh density of the inflated cylinder: simple (a) and with the inclusion (b). We need at least four layers across the lumen to efficiently apply the growth algorithm.

Appendix B

5.1 Patient (ID: 779)

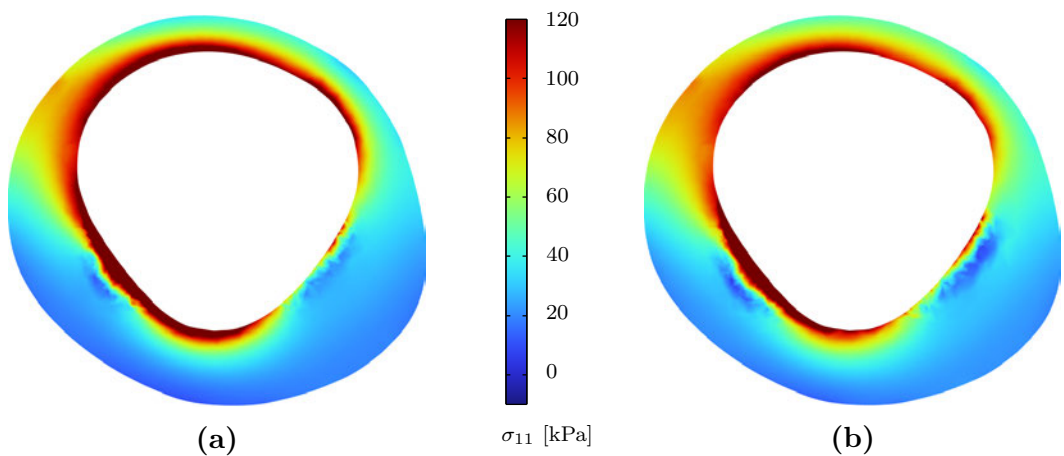


Figure 5.3: First principal stress field on the slice of interest with a boundary condition of **systolic blood pressure** and comparison between the standard (a) and the growth (b) analysis.

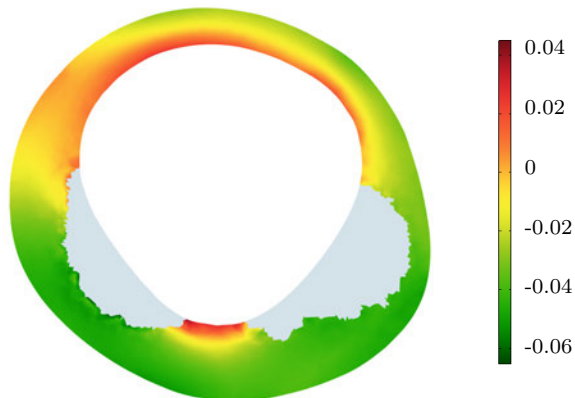


Figure 5.4: Residual volumetric strain on the slice of interest shown only for vascular tissue (MATX).

5.2 Patient (ID: 753) - bulk material effect

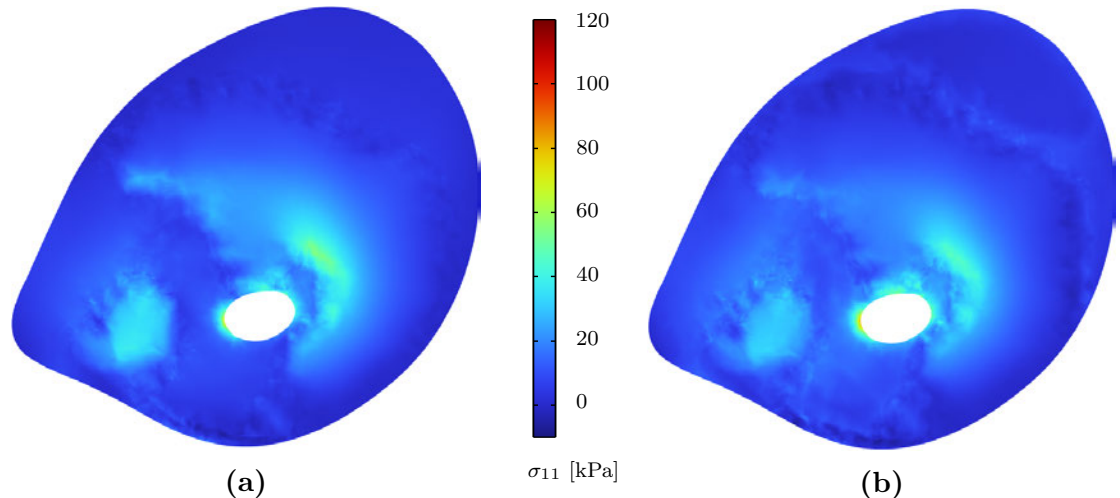


Figure 5.5: First principal stress field on the slice of interest with a boundary condition of **systolic blood pressure** and comparison between the standard (a) and the growth (b) analysis.

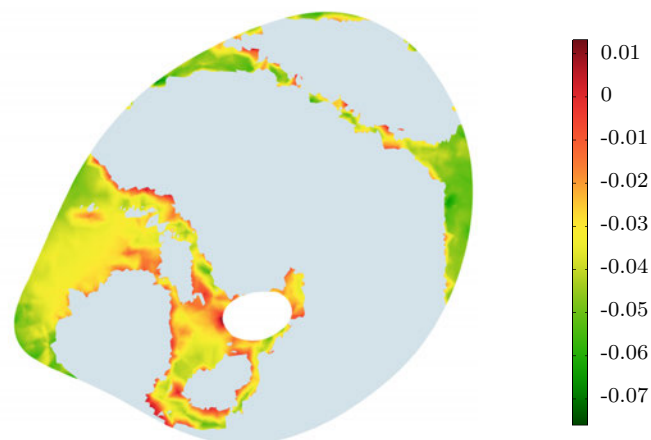


Figure 5.6: Residual volumetric strain on the slice of interest shown only for vascular tissue (MATX).

5.3 Patient (ID: 710) - calcifications

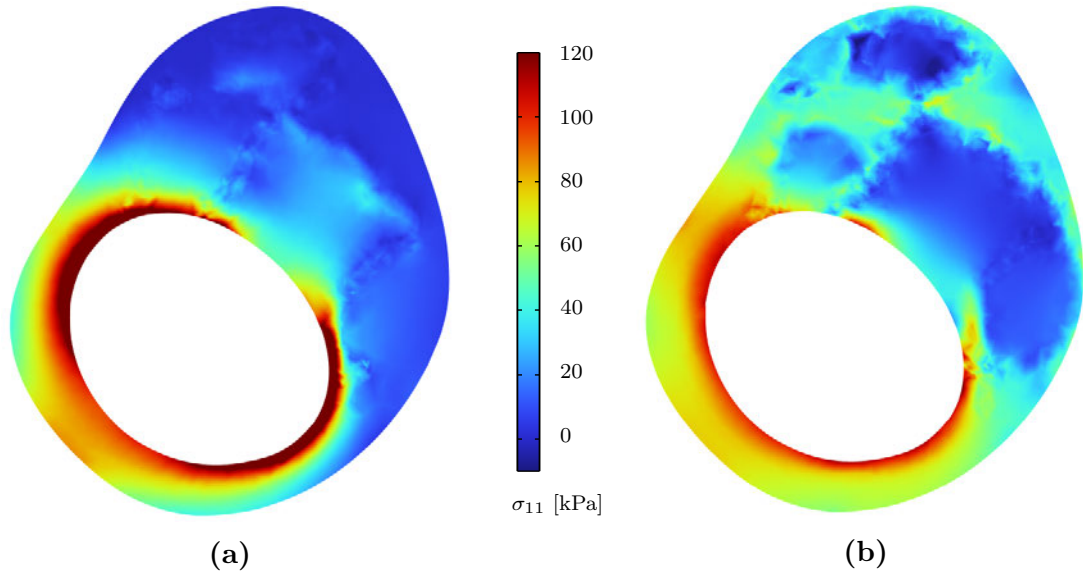


Figure 5.7: First principal stress field on the slice of interest with a boundary condition of **systolic blood pressure** and comparison between the standard (a) and the growth (b) analysis.

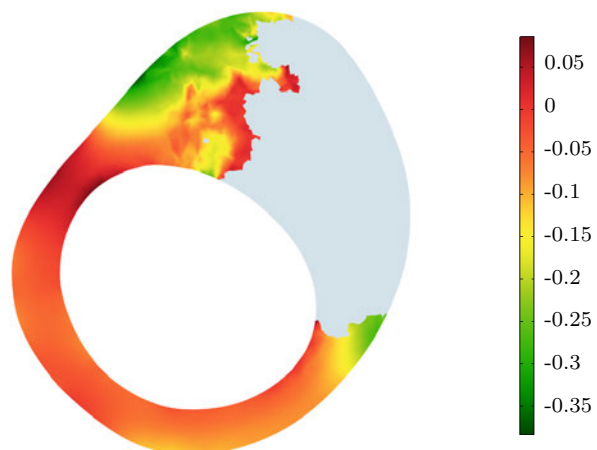


Figure 5.8: Residual volumetric strain on the slice of interest shown only for vascular tissue (MATX).

Appendix C

Showed Finite Element analysis have been solved through Comsol Multiphysics. It is a simulation software used for various physics and engineering applications. In particular, the software allows to easily implement Finite Element analysis also considering multiphysics formulations. In this case the thermo-mechanical coupling was exploited in order to access further degrees of freedom in each element by exploiting the volumetric growth.

5.4 Staggered approach

Simulations have been solved through a staggered approach that allows obtaining a relatively fast convergent formulation with good accuracy.

This staggered approach allows us also to insert a step to compute the tissue growth and remodeling based on mechanical stress. It requires state variable available from Comsol 6.0.

To overcome the large non-linearities of the problem, the analysis is carried out on different load steps. It allows also us to consider several scenarios. For instance, it is possible to drive the load to the average blood pressure to compute growth or systolic blood pressure to analyze the risk of plaque rupture. Furthermore, it is possible to unload the configuration to investigate residual stress and strain.

Through the state variables, it is possible to compute the current stress state at each step and then compare it to the average stress as explained in the growth formulation. However, it requires storing at least three values (growths in each global direction) for each node. Furthermore, extra temporary variables may be needed to compute the growth as the older one or previous stress state and it is not difficult to

rapidly extend the degrees of freedom for each node

Despite this state variables require not complex and iterative calculation (as algebraic system solving) they are large data (obviously depending on the number of nodes) that have to be stored in the computer RAM. Furthermore, this model requires also a thermo-mechanical coupled formulation for incompressible material and so at least Lagrange pressure and thermal strain need to be stored and computed.

It is clearly a time-demanding problem however it is important to follow the Comsol guidelines about degrees of freedom and RAM availability of more or less 1.5 GB of RAM per million of DoFs. If the global amount of DoF exceeded the RAM amount the solver will go out of memory (and start writing on the hard drive expecting data) and the solving time exponentially increases.

In this model the first step to reduce the required DoFs for state variables is to express the growth conditions as nested if conditions including:

- Condition to separate healthy tissue from the pathological one
- Average stress state computation
- Growth computation
- Growth scaling across the first principal stress direction

The model follows the above logic:

```
IF tissue is healthy:  
    COMPUTE average stress  
    PROJECT through first principal stress direction components  
    SCALE growth with growth law and scaling factor
```

In order to check for the healthy tissue material properties are used.

In addition, it is not possible to compute the average through the averaging function of Comsol but it is necessary to manually integrate the average as:

$$\bar{\sigma} = \frac{\int_{\Omega} f \sigma \, dv}{\int_{\Omega} f \, dv} \quad (5.4.1)$$

Where the same definition of the healthy tissues is used to define f as:

$$f := \begin{cases} 1, & \in \text{healty tissue} \\ 0, & \notin \text{healty tissue} \end{cases} \quad (5.4.2)$$

Due to Comsol design it requires extra nested if condition to define f inside the main aforementioned solving cycle.

Furthermore, the staggered approach is driven by two scaling factors to govern load and growth intensity.

5.5 Relaxed formulation

It is also important to mention that in order to stabilize the formulation the growth computation expressed in fig. 3.6 was converted into a relaxed formulation.

It is possible to update the new growth variables by taking into account also previous information. We consider the actual growth deformation tensor as:

$$\mathbf{G} = \mathbf{I} + \beta \left(\alpha^{(k-1)} \mathbf{\Lambda}^{(k-1)} \right) + (1 - \beta) \left(\alpha^{(k-2)} \mathbf{\Lambda}^{(k-2)} \right) \quad (5.5.1)$$

Where k follows the load increment over the boundary pressure and the actual deformation gradient is computed taking into account the previous stress field (rought $\alpha^{(k-1)}$) and also the previous growth deformation gradient computed at the previous load step (rought $\alpha^{(k-2)}$).

As explained in the method section the growth parameter α is related to the difference between local (element) stress and average stress and the projection tensor $\mathbf{\Lambda}$ allows directing tissue remodelling into the first principal stress direction.

The relaxation coefficient is taken as $\beta = 0.9$.

5.6 Variable stiffness spring

In order to unload the configuration it is not simply possible to remove the boundary conditions of blood pressure. The growth algorithm induces also internal stress and it is necessary to completely remove constrains in order to leave the configuration stress-free.

In order to relieve all the stresses we follow two different approaches. The first one is to simply leave one side completely free to avoid the compressive reaction due to the fixed constraints. The second approach is based on the remotion of the fixed constraints. To this avoiding instability during the Finite Element analysis we used **spring foundation** constrain. It is possible to use high-stiffness springs that act as a fixed constraint and then gradually reduce the stiffness with extra load steps in order to relieve mechanical stress.

List of Figures

1.1	Schematic representation of the carotid arteries: common carotid artery (CCA), internal carotid artery (ICA) and external carotic artery (ECA). Schematic representation of the plaque at the carotid bifurcation.	6
1.2	Evolution of carotid atherosclerosis: normal vessel (a); initial initmal thickening (b) low-density lipoprotein deposition and starting of oxaditve reaction (c); atheroma (d); clinical condition with large necrotic core, thin fibrotic cap and thombosis (e).	7
1.3	Representation of biological organisms involves multiple disciplines to describe the real systems and be able to extract useful results from the model (a); Biological hierarchy involve multiple scales (b)	13
2.1	One of the way to represent the opening angle α . Whole ring geometry with internal and external radii(a); Cutted ring geometry (b); Opening of a common carotid artery ring showing the relasing of residual stresses (c) [84]	19
3.1	Motion χ of the body from the reference configuration Ω_0 to the current configuration Ω (a); Representation of the stress state, with a hypothetical cut through the body perpendicular to \mathbf{n} , and of the corresponding traction vector treading from the Cauchy's stress theorem $\mathbf{t}(\mathbf{x}) = \boldsymbol{\sigma}(\mathbf{x})\mathbf{n}(\mathbf{x})$ (b); Normal stress components σ_{ii} and shear stress components σ_{ij} determine the traction vector \mathbf{t} and the load acting at the material particle (c).	24
3.2	Pressurized cylinder vessel (a) with internal pressure p with circumferential (or tangential) stress σ_θ , axial stress σ_l and radial stress σ_r . Circumferential and radial stresses are highlighted in (b) and (c).	25
3.3	3D volumetric reconstruction with coronal, para-sagittal and horizontal plane of CTA image (a) and tissue segmentation (b) for carotid bifurcation with atherosclerotic vessel. Example of meshed atherosclerotic carotid vessel (c).	33
3.4	Representation of the tissue growth and remodeling through a kinematic description. The stress-free intermediate (eventually incompatible) configuration Ω_0 separates the growth-related and the non-growth-related motions. The deformation gradient is multiplicatively decomposed and the final deformation is due to both the deformation gradient and the growth tensor.	35
3.5	Stress vs. stretch curves for different tissue types at uniaxial extension.	37

3.6	Growth algorithm that allows us to calculate the growth deformation gradient to homogenize the stress field. It is used up to mean pressure (given the oscillatory behavior of blood pressure the growth is assumed to reflect what happens at mean pressure). The k steps follow the load history to increment internal pressure from zero to the boundary condition (average blood pressure) while the j steps follow the growth scaling factor. For each step, the algorithm solves the mechanical problem and computes the stress field. Through the stresses, it is possible to compute the desired volumetric growth tensor (as described by eq. (3.6.4)) with the aim of minimizing the stress gradient. At each step, the applied growth is related to the computing at the previous step.	38
3.7	Normalized scaling factors used to modulate external load or activate growth. Different approaches are presented: in (a) growth and load are increased together until the maximum is reached, in (b) firstly the load is increased and then the growth is computed, and a hybrid approach is shown in (c). tt represent a fictitious time, while loadFactor and growthFactor represent respectively the k and j indexes shown in the general algorithm in fig. 3.6	38
3.8	Generic workflow for the model. It starts with a conversion from medical images into a mesh, segmenting the images such to distinguish between the properties of the different tissues. The STL mesh models are imported into Comsol material properties assigned through a Matlab procedure. Finite element simulation routines in Comsol are employed to compute the finite element solution and investigate the stress state and residual strains. (*) Solving times are referred to a Windows11 workstation with i7-10850H and 32 GB RAM at 2933 MHz.	41
4.1	First principal stress for the inflated cylinder on standard (a) and growth (b) formulation on a half-height plane. It is possible to observe the stress homogenization in the analysis with the tissue growth. In the standard analysis, the stress varies from more than 50 kPa to less than 20 kPa. Instead, in the growth formulation stresses appear to be in a more restricted range.	43
4.2	Ideal cylinder with the inclusion. The red domain ■ presents MATX material properties and the blue one □ presents CALC material properties.	44
4.3	First principal stress for the inflated cylinder with inclusion (as calcification) on standard (a) and growth (b) formulation on a half-height plane. The stress pattern appears similar however in the growth formulation peak stresses are lower. The stress gradient across the wall appears to be reduced.	44
4.4	First principal stress over a cut line across the wall lumen (c), the coordinate s varies from zero, outside the wall, and 1 at the internal side. It is possible to observe how the stress difference is reduced by more than 50%.	45
4.5	Residual strain for inflated normal cylinder without (a) and with (b) inclusion. Volumetric strain is shown on a half-height plane. The residual strain appears positive inside and slightly negative outside. In the simple cylinder (a), the positive strain is up to 10% instead the negative one is slightly lower than expected. For the case with inclusion (b) the residual strain appear higher where the peak stress was identified, right at the interface between the inclusion and the vascular tissue. Clearly, in the inclusion it is zero considering that the growth algorithm does not work on tissues other than the vascular one (MATX).	45
4.6	3D reconstruction of the vessel for patient ID 643(a); Slice of interest (b) with different materials highlighted with different colors. In the table also the percentages of the constituents are shown for the whole vessel.	47
4.7	Mesh sensitivity analysis showing how NRMSE decrease with increasing in number of elements. Also the normalized computational time respect to the maximal one is shown. 48	48

4.8	Stresses distributions obtained from meshes with a different number of elements.	48
4.9	Comparison of the stress distributions between formulation with and without growth for the first (a), second (b) and third (c) proposed approaches of load-growth relation.	49
4.10	Relative normalized deviation (see eq. (3.6.7)) of the local stress from the averaged homogenized stress for each growing step j after reaching the trigger load for the patient-specific case for the hybrid approach.	49
4.11	First principal stress distribution in the whole vessel at average pressure where the reduction of the peak stresses is strongly evident.	50
4.12	First principal stress field on the slice of interest with a boundary condition of average blood pressure and comparison between the standard (a) and the growth (b) analysis. The standard analysis shows a well-evident gradient of the stress across the wall thickness. Instead, by considering the growth algorithm (b), a more homogenous stress field is obtained. Furthermore, the peak stresses appear to be reduced. The lipid region, due to the more compliant behavior, appears to be less active in loading stress by considering the tissue redistribution.	51
4.13	Residual growth intensity as volumetric strain represented through the color map and main growth direction computed at average pressure plotted over half vessel (left) and slice of interest (right).	52
4.14	First principal stress distribution in the whole vessel at physiological systolic pressure.	53
4.15	First principal stress field on the slice of interest with a boundary condition of systolic blood pressure and comparison between the standard (a) and the growth (b) analysis. The standard analysis shows a well-evident gradient of the stress across the wall thickness. Instead, by considering the growth algorithm (b), a more homogenous stress field is obtained. The stress pattern is similar to the average pressure (fig. 4.12) however notice that the color scale is doubled. In the solution with the growth formulation, the peak stress appears to be strongly reduced. Furthermore, it is interesting to observe how the area with higher stress is localized near the fibrous cap (arrow).	54
4.16	First principal stress distribution in the whole vessel at hypertension pressure.	55
4.17	Second slice of the first patient-specific analysis: the slice of interest (a) and the tissues distribution (b).	56
4.18	First principal stress field on the second slice of interest with a boundary condition of 180 mmHg and comparison between the standard (a) and the growth (b) analysis. The growth one shows a reduction of peak stresses and a more homogenous stress field.	56
4.19	Third slice of the first patient-specific analysis: the slice of interest (a) and the tissues distribution (b).	57
4.20	First principal stress field on the third slice of interest with a boundary condition of 180 mmHg and comparison between the standard (a) and the growth (b) analysis. The growth one shows a reduction of peak stresses and a more homogenous stress field.	57
4.21	Residual strain on the slice of interest. Volumetric strains are shown for vascular tissue (MATX) and appear positive on the internal side and negative outside.	59
4.22	3D reconstruction of the vessel for patient ID 779 (a); Slice of interest (b) with different materials highlighted with different colors. In the table also the percentages of the constituents are shown for the whole vessel.	60
4.23	First principal stress field on the slice of interest with a boundary condition of average blood pressure and comparison between the standard (a) and the growth (b) analysis.	60
4.24	3D reconstruction of the vessel for patient ID 753 (a); Slice of interest (b) with different materials highlighted with different colors. In the table also the percentages of the constituents are shown for the whole vessel.	61
4.25	First principal stress field on the slice of interest with a boundary condition of average blood pressure and comparison between the standard (a) and the growth (b) analysis.	61

4.26	3D reconstruction of the vessel fro patient ID 710 (a); Slice of interest (b) with different materials highlighted with different colors. In the table also the percentages of the constituents are shown for the whole vessel.	62
4.27	First principal stress field on the slice of interest with a boundary condition of average blood pressure and comparison between the standard (a) and the growth (b) analysis.	62
5.1	The geometry of the inflated cylinder: simple (a) and with the inclusion (b). The curve surface is splitted into four regions (both for the external and the internal ones) from Comsol as you can see from the vertical lines.	76
5.2	Average mesh density of the inflated cylinder: simple (a) and with the inclusion (b). We need at least four layers across the lumen to efficiently apply the growth algorithm.	76
5.3	First principal stress field on the slice of interest with a boundary condition of systolic blood pressure and comparison between the standard (a) and the growth (b) analysis.	77
5.4	Residual volumetric strain on the slice of interest shown only for vascular tissue (MATX).	77
5.5	First principal stress field on the slice of interest with a boundary condition of systolic blood pressure and comparison between the standard (a) and the growth (b) analysis.	78
5.6	Residual volumetric strain on the slice of interest shown only for vascular tissue (MATX).	78
5.7	First principal stress field on the slice of interest with a boundary condition of systolic blood pressure and comparison between the standard (a) and the growth (b) analysis.	79
5.8	Residual volumetric strain on the slice of interest shown only for vascular tissue (MATX).	79